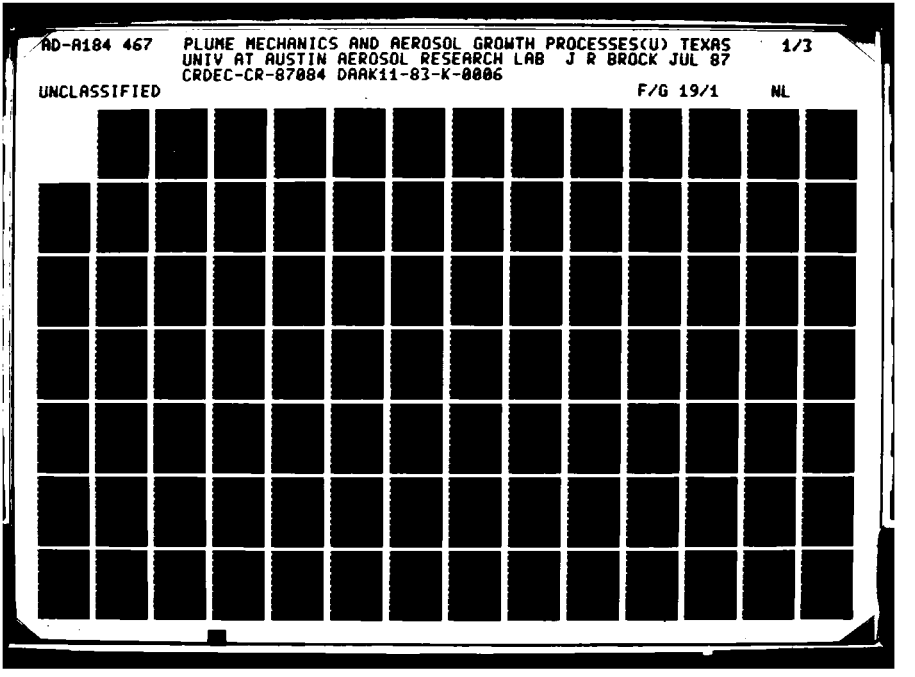
AD-A184 467 PLUME MECHANICS AND AEROSOL GROWTH PROCESSES(U) TEXAS 1/3
UNIV AT AUSTIN AEROSOL RESEARCH LAB J R BROCK JUL 87
CRDEC-CR-87084 DAAK11-83-K-0006
UNCLASSIFIED F/G 19/1 NL

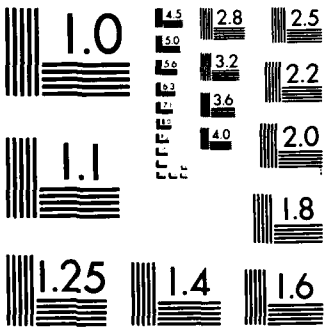

MICROCOPY RESOLUTION TEST CHART
NATIONAL BUREAU OF STANDARDS-1963-A

(12)

CHEMICAL RESEARCH, DEVELOPMENT & ENGINEERING CENTER

CRDEC-CR-87084

PLUME MECHANICS AND AEROSOL GROWTH PROCESSES

by J.R. Brock
UNIVERSITY OF TEXAS
Austin, TX 78712

July 1987

U.S. ARMY
ARMAMENT
MUNITIONS
CHEMICAL COMMAND

Aberdeen Proving Ground, Maryland 21010-5423

Disclaimer

The findings in this report are not to be construed as an official Department of the Army position unless so designated by other authorizing documents.

Distribution Statement

Approved for public release; distribution is unlimited.

UNCLASSIFIED
SECURITY CLASSIFICATION OF THIS PAGE

REPORT DOCUMENTATION PAGE

1a REPORT SECURITY CLASSIFICATION UNCLASSIFIED	1b RESTRICTIVE MARKINGS
2a SECURITY CLASSIFICATION AUTHORITY	3 DISTRIBUTION/AVAILABILITY OF REPORT Approved for public release; distribution is unlimited.
2b DECLASSIFICATION/DOWNGRADING SCHEDULE	
4 PERFORMING ORGANIZATION REPORT NUMBER(S) CRDEC-CR-87084	5. MONITORING ORGANIZATION REPORT NUMBER(S)
6a NAME OF PERFORMING ORGANIZATION University of Texas Aerosol Research Laboratory 6b OFFICE SYMBOL (If applicable)	7a. NAME OF MONITORING ORGANIZATION
6c. ADDRESS (City, State, and ZIP Code) Austin, TX 78712	7b. ADDRESS (City, State, and ZIP Code)
8a. NAME OF FUNDING/SPONSORING ORGANIZATION CRDEC 8b. OFFICE SYMBOL (If applicable) SMCCR-RSP-B	9. PROCUREMENT INSTRUMENT IDENTIFICATION NUMBER DAAK11-83-K-0006
8c. ADDRESS (City, State, and ZIP Code) Aberdeen Proving Ground, MD 21010-5423	10 SOURCE OF FUNDING NUMBERS PROGRAM ELEMENT NO. / PROJECT NO / TASK NO. / WORK UNIT ACCESSION NO
11 TITLE (Include Security Classification) Plume Mechanics and Aerosol Growth Processes	
12 PERSONAL AUTHOR(S) Brock, J.R.	
13a TYPE OF REPORT Contractor 13b. TIME COVERED FROM 83 Aug TO 86 Jul 14. DATE OF REPORT (Year, Month, Day) 1987 July 15 PAGE COUNT 219	
16 SUPPLEMENTARY NOTATION COR: Dr. G. Rubel, SMCCR-RSP-B, (301) 671-2326	

17 COSATI CODES			18. SUBJECT TERMS (Continue on reverse if necessary and identify by block number)	
FIELD	GROUP	SUB-GROUP		
07	04		Aerosol Growth	Laminar Coaxial Jet
			Dispersion	Ostwald Ripening
			Ferromagnetic Particles	Laser-Particle Interactions

19 ABSTRACT (Continue on reverse if necessary and identify by block number)

Results of research on major topics in aerosol science and technology are summarized. These include: (1) Formation of liquid and solid particles by nucleation and growth; (2) Influence of smoke plume/puff dispersion on aerosol growth; (3) Nonlinear interations of laser beams with aerosols; (4) Aerosol filtration.

20 DISTRIBUTION/AVAILABILITY OF ABSTRACT ☒ UNCLASSIFIED/UNLIMITED ☐ SAME AS RPT ☐ DTIC USERS	21 ABSTRACT SECURITY CLASSIFICATION UNCLASSIFIED
22a NAME OF RESPONSIBLE INDIVIDUAL TIMOTHY E. HAMPTON	22b TELEPHONE (Include Area Code) (301) 671-2914 22c OFFICE SYMBOL SMCCR-SPS-T

DD FORM 1473, 84 MAR

83 APR edition may be used until exhausted
All other editions are obsolete

SECURITY CLASSIFICATION OF THIS PAGE
UNCLASSIFIED

PREFACE

The work described in this report was authorized under Contract No. DAAK11-83-K-0006. This work was started in August 1983 and completed in July 1986.

The use of trade names or manufacturers' names in this report does not constitute an official endorsement of any commercial products. This report may not be cited for purposes of advertisement.

This document has been approved for release to the public.

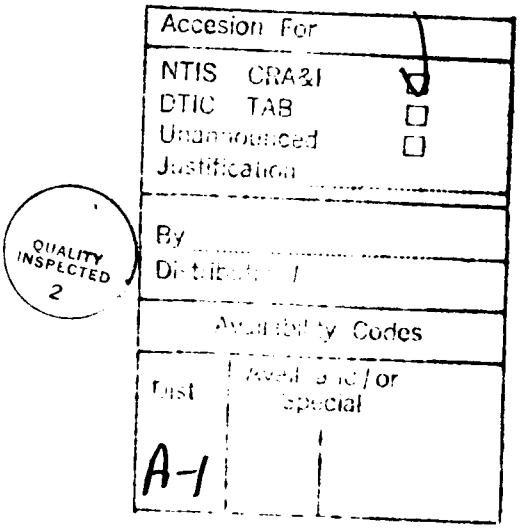

Blank

TABLE OF CONTENTS

TABLE OF CONTENTS (Continued)

LIST OF FIGURES

LIST OF FIGURES (Continued)

LIST OF FIGURES (Continued)

LIST OF FIGURES (Continued)

LIST OF FIGURES (Continued)

LIST OF FIGURES (Continued)

LIST OF FIGURES (Continued)

LIST OF TABLES

PLUME MECHANICS AND AEROSOL GROWTH PROCESSES

I. OBJECTIVES OF RESEARCH

Work under this contract was intended to add to the technological base of the U. S. Army's programs in aerosol technology, smoke and protection, as well as to contribute to fundamental knowledge of aerosol physics and chemistry. In this study, the following areas have been investigated:

(1) Formation of liquid and solid particles by nucleation and growth.

(2) Influence of smoke plume/puff dispersion on aerosol growth.

(3) Nonlinear interactions of laser beams with aerosols.

(4) Aerosol filtration.

Areas (1) and (2) above deal with key problems in smoke obscuration. The efficiency of an aerosol obscurant for electromagnetic radiation depends on many factors including particle size, shape, composition and concentration. For an obscurant propagating in the atmosphere, particle size, shape, composition, and concentration are determined by the processes of particle generation and growth as well as by advection, dispersion and other processes of atmospheric motion. While some qualitative features of these various processes are recognized, our knowledge is incomplete. Improvements in aerosol obscurant technology must depend in part on development of the basic knowledge of the various processes cited above.

Most aerosol obscurants are generated by the condensation of atomic or molecular species initiated by a nucleation process. The description of this process remains today as one of the unsolved classical problems of physics. Subsequent to their formation by nucleation, the stable particles grow by coagulation and condensation/evaporation processes. For liquid particles of a single chemical species which coalesce on collision, these processes for restricted homogeneous systems can be described quantitatively. However, even in this limited case, this has only recently been done. For particles that do not coalesce on collision, no general theory is available. Such particles will form larger particles with complex morphology - chains, branched structures, random aggregates, etc. - whose description in the context of a dynamic model has not yet been achieved. When the aerosol is formed from a mixture of chemical species, the problems cited above for single component aerosols are compounded. The study of the evolution of aerosol mixtures is only in its initial stages.

When aerosol obscurants are formed in the atmosphere, the formation and growth processes discussed above will occur in a turbulent environment. First these processes take place in turbulence produced by the obscurant generation device. Then, atmospheric turbulence takes over, and the subsequent evolution occurs in this environment. The description of turbulence also remains as one of the unsolved classical problems of physics. While qualitative descriptions of aerosol evolution in a turbulent environment are available in special cases, no general

quantitative description is currently available. Only empirical descriptions of limited validity can be found in the literature. The evolution of an aerosol in an atmospheric plume is a complex process whose average characteristics have only recently been studied quantitatively.

Practical application of work under area (3) is found in the problems of transmission of intense laser beams through the atmosphere and in possible use of aerosols as protective screens. If one wishes to propagate an intense laser beam in the atmosphere, the presence of water aerosols, fog and cloud droplets poses a difficulty. In this case an understanding of rapid aerosol evaporation by laser beams is essential. Laser beams are totally absorbed by plasmas and scattered by particle explosion. These phenomena present possibilities for the use of aerosol as protective screens against intense laser beams.

Area (4) is concerned with the problems of protecting personnel by use of mask air filters against chemical and biological aerosol threat agents. In order to ensure such protection, it is essential to understand filtration mechanisms for fibrous and membrane filters and factors which could contribute to enhanced penetration of filters by aerosol particles.

Work under this contract has addressed important aspects of these areas of application. In the following report, the research performed is outlined. Full details are available for the most part in the various publications resulting from this research.

II. SUMMARY OF RESULTS

Highlights of major accomplishments from the research are presented here along with a listing of publications arising from this work. This section is followed by a more detailed exposition. The major accomplishments are listed in approximate chronological order.

A. Major Accomplishments.

Under contract from the Chemical Research Development and Engineering Center (CRDEC) some major accomplishments of our work, in approximate chronological order, are as follows:

* A theoretical basis and numerical schemes have been developed for simulating the atmospheric dispersion of plumes of volatile aerosol such as diesel smoke plumes. Computer code for this simulation has been transferred to CRDEC for their use in planning and evaluation as a replacement for inaccurate Gaussian plume models. See publications CRDEC 1, 2 and 3.

* A theoretical basis and computer code have been developed for dispersing atmospheric plumes emitting infrared or other radiation as a result of chemical or thermochemical reactions. See publication CRDEC 4.

* The first simulations of the Ostwald ripening process have been carried out showing the approach to asymptotic limit distributions in the continuum and free molecule regimes. See publication CRDEC 5.

* The first simulations of the dynamics of the Ostwald ripening process with simultaneous coalescence have been carried out showing that scaling arguments are insufficient to establish the dominant asymptotic growth mechanism in the continuum regime. See publication CRDEC 6.

* Limitations in the use of Fokker-Planck equations for describing growth of clusters, as used in development of classical Becker-Doring-Zeldovich homogeneous nucleation theory, have been demonstrated. See publication CRDEC 7.

* Moment methods have been extended to include aerosol evaporation for the first time. This permits easy and rapid numerical simulations of evaporation processes. See publication CRDEC 8.

* The production of ultrafine metallic particles by evaporation of metallic samples in the gas phase has been employed in research and commercial applications for at least 50 years. In spite of this long history, the processes determining particle size concentration and morphology have not been understood. Through an experimental and theoretical program, we have developed a model which explains all the important features of particle formation and growth in these applications. See publication CRDEC 9.

* The first thorough experimental and theoretical investigations of ferromagnetic particle formation by borohydride reduction in aqueous phase have been carried out. New regimes of particle growth have been discovered. Characteristics of primary particles have been explained through a model based on a chemical mechanism for reduction of cations by borohydride ions. See publication CRDEC 10.

* The first quantitative experimental data have been obtained for binary aerosols formed by homogeneous nucleation of vapor mixtures. The experimental results are explained by a theoretical model for binary homogeneous nucleation and growth. See publications CRDEC 11 and 12.

* We have carried out the first quantitative simulation of the explosion of water droplets caused by absorption of intense laser radiation. Substantial departure from classical blast wave theory is shown to arise from homogeneous vapor nucleation early in the shock expansion. See publication CRDEC 13.

* We have carried out the first quantitative simulation of rapid evaporation of small droplets exposed to intense laser beams. Computer code IRDE (radial isobaric radial droplet evaporation) has been developed for this simulation. See publication CRDEC 14.

* The first simulation of the evolution of the aerosol size distribution in the presence of a laser beam has been carried out. See publication CRDEC 15.

* The first complete theoretical investigation of fibrous and membrane filter filtration mechanisms has been carried out numerically. See publication CRDEC 14.

B. Publications from CRDEC Contract Work.

CRDEC-1. T. H. Tsang and J. R. Brock, "Dispersion of a plume of volatile aerosol," Aerosol Science and Technology, 2 429-436 (1983).

CRDEC-2. T. H. Tsang and J. R. Brock, "Simulation of condensation aerosol growth by condensation and evaporation," Aerosol Science and Technology, 2 311-320 (1983).

CRDEC-3. J. R. Brock, "New aspects of aerosol growth processes," Aerosol Science and Technology, 2 109-120 (1983).

CRDEC-4. J. R. Brock, "Dispersion of thermal and Chemiluminescent plumes," in R. Kohl, Ed. Proceedings of the 1985 Scientific Conference on Obscuration and Aerosol Research, CRDEC-SP-86019, 1986.

CRDEC-5. T. H. Tsang and J. R. Brock, "On Ostwald ripening," Aerosol Science and Technology, 3 283-292 (1984).

CRDEC-6. T. H. Tsang and J. R. Brock, "Dynamics of Ostwald ripening with coalescence," Aerosol Science and Technology, 5 (1986).

CRDEC-7. J. R. Brock, "Remarks on particle size distributions of ultrafine binary particles with one involatile component," Journal of Aerosol Science, 4 273-278 (1985).

CRDEC-8. J. R. Brock and J. Oates, "Moment method for aerosol evaporation," Journal of Aerosol Science, 5 (1986).

CRDEC-9. S. G. Kim and J. R. Brock, "Formation of primary metal particles in evaporation chambers," Journal of Applied Physics, 60(2) 509-513 (1986).

CRDEC-10. S. G. Kim and J. R. Brock, "Growth of ferromagnetic particles from cation reduction by borohydride ions," Journal of Colloid and Interface Science, 100 (1986).

CRDEC-11. J. R. Brock, P. J. Kuhn and D. Zehavi, "Condensation aerosol formation and growth in a laminar coaxial jet: Experimental," Journal of Aerosol Science, 17 11-22 (1986).

CRDEC-12. J. R. Brock and P. J. Kuhn, "Binary nucleation and growth of aerosols in a laminar coaxial jet," Journal of Aerosol Science, In Press, 1987.

CRDEC-13. S. G. Davies and J. R. Brock, "Evaporation of droplets in intense laser beams," Submitted for publication.

CRDEC-14. S. G. Kim and J. R. Brock, "Chain aggregate aerosols produced by liquid phase reactions," in B. Liu et al. Eds. Aerosols: Science, Technology and Industrial Applications, Elsevier, NY, 1984.

CRDEC-15. C. Seigneur, A. Hudischbwsky, J. Seinfeld, K. Whitby, E. Whitby, J. R. Brock, and H. M. Barnes, "Simulation of aerosol dynamics: A comparative review of mathematical models," Aerosol Science and Technology, 5 205-223 (1986).

CRDEC-16. J. R. Brock, "Simulation of aerosol dynamics," in R. E. Meyer, Ed., Theory of Dispersed Multiphase Flow, Academic Press, NY, 1983.

CRDEC-17. S. G. Kim, "Formation and Growth of Ultrafine Ferromagnetic Particles," Ph.D. Dissertation, University of Texas, Austin, 1985.

CRDEC-18. J. R. Brock, "Aerosol generation: Studies of nucleation and growth processes," in R. Kohl, Ed., Proceedings of the 1983 Scientific Conference on Obscuration and Aerosol Research, U.S.A.A.M.C.C., Aberdeen Proving Ground, Maryland, 1984.

CRDEC-19. J. R. Brock, T. H. Tsang and S. G. Kim, "Aerosol plume mechanics and particle growth processses," in R. Kohl, Ed., Proceedings of The Chemical Research and Development Center's 1984 Scientific Conference on Obscuration and Aerosol Research, U.S.A.A.M.C.C., Aberdeen Proving Ground, Maryland, 1985.

CRDEC-20. J. R. Brock, "Nucleation and particle growth," in R. Kohl, Ed. Proceedings of the 1985 Scientific Conference on Obscuration and Aerosol Research, CRDEC-SP-86019, 1986.

CRDEC-21. J. R. Brock, "Interaction of aerosol with laser beams," in R. Kohl, Ed., Proceedings of the 1985 Scientific Conference on Obscuration and Aerosol Research, CRDEC-SP-86019, 1986.

CRDEC-22. S. G. Kim and J. R. Brock, "Particle formation a d growth," in R. Kohl, Ed., Proceedings of the 1986 Scientific Conference on Obscuration and Aerosol Research , CRDEC-SP-86, To Appear.

CRDEC-23. J. Carls, S. G. Davies and J. R. Brock, "Nonlinear laser-particle interactions," in R. Kohl, Ed., Proceedings of the 1986 Scientific Conference on Obscuration and Aerosol Research , CRDEC-SP-86, To Appear.

CRDEC-24. S. C. Davies, Evaporation of Aerosols by Laser Radiation, M. S. Thesis, University of Texas, Austin, 1986.

Blank

III. DETAILED SUMMARY OF CRDEC CONTRACT WORK

Complete details of work performed under CRDEC Contract DAAK-83-K-0006 are given in the publications listed in Section II. In this section, a detailed summary is given of the general results from this research in the four areas listed in Section I. First, work done on particle formation by homogeneous nucleation and growth is discussed. Extension of this work to atmospheric dispersion of evolving plumes is presented next. Then, work done on nonlinear interactions of intense laser beams with aerosol particles is summarized. Finally, first results from investigations of aerosol filtration from the standpoint of protection is outlined.

A. Aerosol Growth Processes and Plume Mechanics

The most important and usual means for production of particles less than the order of 1 m involves homogeneous nucleation in a vapor or liquid and subsequent growth by condensation/evaporation and coagulation. This part of our research has been directed toward investigation of these processes and their incorporation in models for atmospheric dispersion of aerosols. In this section work on homogeneous nucleation and particle growth is discussed first. This begins with work on nucleation and growth of liquid aerosol followed by work on metallic aerosol's and hydrosols. Then simulation work on atmospheric dispersion is presented.

A-1. Aerosol formation and growth in a laminar coaxial jet.

In nature and many technical applications, aerosol is formed by homogeneous nucleation of a vapor. A few examples include condensation in plumes from industrial sources, in rocket nozzles, in explosions and in various natural processes. Subsequent to formation by nucleation, the aerosol may grow by condensation/evaporation and coagulation. In spite of the importance of these processes, there are few available experimental data suitable for tests of theories of particle formation and growth. A number of studies have been carried out in turbulent flows, e.g. Amelin[1], Higuchi and O'Konski[2], Hidy and Friedlander[3], Delattre and Friedlander[4], Ismagilov et al.[5], Anisomov et al.[6] and Sutugin et al.[7]; however, measurement and interpretation of particle formation and growth in turbulent flows pose difficulties which, until now, have not been overcome completely.

The principal purpose of our work has been to investigate the dependence of the disperse properties of binary aerosols formed by homogeneous nucleation on the physicochemical properties of the mixtures. We have carried out studies by following the condensation of oil vapors in a laminar coaxial jet. A laminar coaxial jet provides a fluid dynamical state which can be modelled numerically with considerable accuracy and also eliminates possible influences of wall effects in the initial stages of aerosol growth. The principal theoretical uncertainties in the analysis of such a flow system are found in the description of homogeneous nucleation of the vapor and, less importantly,

in expressions for the dynamical coefficients of coagulation and condensation.

a. Experimental procedure.

A schematic diagram of the experimental system is shown in Figure A-1-1. The principal elements are the liquid oil and carrier gas metering systems, the oil vaporizer, coaxial jet system, and the sampling and aerosol measurement systems.

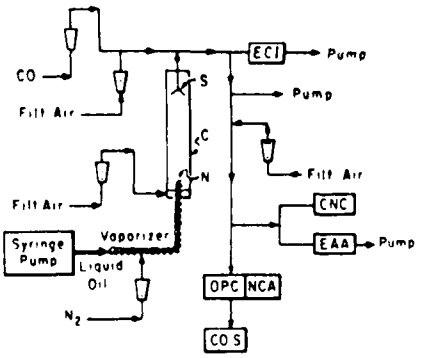

Figure A-1-1. Schematic diagram of experimental laminar coaxial jet system.

Liquid oil was delivered at accurate volumetric flow rates in the range 0.001-0.02 cm^3 min^{-1} by a calibrated syringe pump. Pure nitrogen carrier gas was metered through calibrated rotameters. The liquid oil was vaporized in the nitrogen carrier gas in a heated packed column. Proper design of this vaporizer was essential to obtain a steady, laminar coaxial jet from the nozzle. Also essential was accurate temperature control of the nozzle heater section; this was achieved

through use of a DC power supply controllable to $\pm$ 0.01 W at approximately 19 W total power level coupled to a small thermocouple sensor attached just below the outer exit rim of the nozzle. In the experimental aerosol growth chamber, superheated oil vapor, of a concentration known accurately from the liquid oil metering rate and nitrogen carrier gas flow rate, issued as a laminar coaxial jet from a 0.2 cm diameter circular nozzle (N in Figure A-1-1) along the axis of a 7.6 cm diameter glass tube (C in Figure A-1-1). A coaxial flow of filtered air at 25^{o}C was maintained at determined flow rates. With this arrangement, the laminar coaxial aerosol jet can be caused to travel along the axis of the larger tube for its entire length of 1.25 m. Experimental and theoretical analysis show that jet temperature and velocity are equilibrated with the coaxial air flow at distances greater than several hundred nozzle diameters.

Aerosol sampling was carried out with a cone sampler (S in Figure A-1-1) which collected the total coaxial flow and produced (depending on the coaxial air flow rate) from 10 to 25-fold dilutions of the aerosol in times of the order of a few milliseconds. A larger aerosol jet diameter would have permitted point sampling to investigate the radial variation of aerosol dispersity. However, it was found that sufficiently large nozzles posed the practical problem of unwanted thermal convective motion, and we were not able to overcome this difficulty. Hence, only the average aerosol dispersity over the jet cross-section was investigated. Within times of the order of 0.01 s the

diluted stream from the cone sampler was subsequently diluted by filtered air in a two-stage isokinetic dilution system by dilution factors in the range 1000-10,000. The reason for this large dilution is given below. The exact dilution was determined by metering in CO as a tracer gas, as shown in Figure A-1-1, and determining the CO dilution by means of a calibrated non-dispersive CO sensor. The dilutions used were too large to permit accurate measurement of dilution by methods described in the literature.

A major interest in this study was the disperse properties of aerosols after nucleation and condensation growth was substantially complete; the sampling technique used here was satisfactory for this purpose. Order of magnitude estimates for the volatility of oils used show no measurable evaporation of the aerosols during or after sampling, as substantiated by the experimental measurements.

The principal means employed for measurement of particle size distribution was a Climet 208 optical particle counter (OPC in Figure A-1-1) whose output signals were processed by a Nuclear Data pulse height analyzer and minicomputer system giving 512 channels over the useful range of the Climet (0.3-5 μm particle diameter). It was found to be essential that calibration curves were obtained for the particular oil aerosol to be measured. Determination of particle size distribution from Climet signals was found to depend strongly on particle refractive index. Calibration of the Climet signals was obtained by generating monodisperse aerosols of the oils by means of a parallel plate electrical mobility

analyzer whose performance was further checked by using monodisperse polystyrene latex spheres in the range 0.2-5 μm with diameters determined prior to use by electron microscopy. In using the Climet 208, it was also found to be essential that the aerosol sampled was diluted to particle number concentrations less than 100 cm^{-3}. At higher sampled number concentrations, spurious particle counts are obtained which give particle concentrations incorrect by factors of 10 to 100. A TSI 3030 electrical aerosol analyzer was also used in studies of early stages of aerosol growth in the jet, although these results are only of qualitative interest and are not presented here. An electronic cascade impactor (ECI in Figure A-1-1) was used in a limited series of studies to measure composition as a function of particle size in binary aerosol.

The description of the laminar jet is a classical problem in fluid dynamics and a vast literature exists on the subject (e.g. Pai[13], Birkhoff and Zarantonello[4]). The laminar coaxial jet employed here can be completely described by the following conservation equations of mass, momentum, and energy:

$$\nabla \cdot \rho \underline{v} = 0 \qquad \text{(A-1-1)}$$

$$\rho \underline{v} \cdot \nabla \underline{v} + \nabla p + \nabla \cdot \underline{\underline{\tau}} - \rho \underline{g} = 0 \qquad \text{(A-1-2)}$$

$$\rho c_v \underline{v} \cdot \nabla T = \nabla \cdot k \nabla T - \underline{\underline{\tau}} : \nabla \underline{v} \qquad \text{(A-1-3)}$$

where ρ is the fluid mass density, $\underline{v}$ the mass average velocity, p the pressure, $\underline{\underline{\tau}}$ the shear stress tensor, $\underline{g}$ the gravitational acceleration, c_v the heat capacity, T the fluid temperature, and k the thermal

conductivity. The vapor and aerosol mass concentrations in the jet are approximately three orders of magnitude less than the mass concentration of the carrier gas; consequently, the vapor and aerosol may be regarded as passive contaminants and do not influence the dynamics of the coaxial jet described by equations (A-1-1)-(A-1-3).

A computer program has been developed which permits solution of equations (A-1-1)-(A-1-3) by modeling an axisymmetric, two-dimensional, steady laminar flow. The numerical calculations are carried out using a finite difference method and a variable mesh size to accommodate the rapid changes taking place in the entrance region. Figures A-1-2, A-1-3 and A-1-4 show, respectively, the calculated radial velocity, axial velocity and temperature distributions for the laminar coaxial jet for an initial average nozzle velocity of 94.4 cms^{-1} and temperature of 270°C with an average velocity in the annular regionof 2.34 cms^{-1}. These initial values are those used for the aerosol measurements reported here.

Such calculations permit detailed simulation of aerosol formation and growth with spatial resolutions in the velocity and temperature fields not possible by present experimental techniques. As a check that the theoretical model approximated the experimental system, average temperatures in the aerosol jet were measured by means of small thermocouples. Figure A-1-5 shows the approximate agreement between the calculated and observed average jet temperatures as a function of downstream distance. These measurements therefore also confirm the computed velocity fields in the jet.

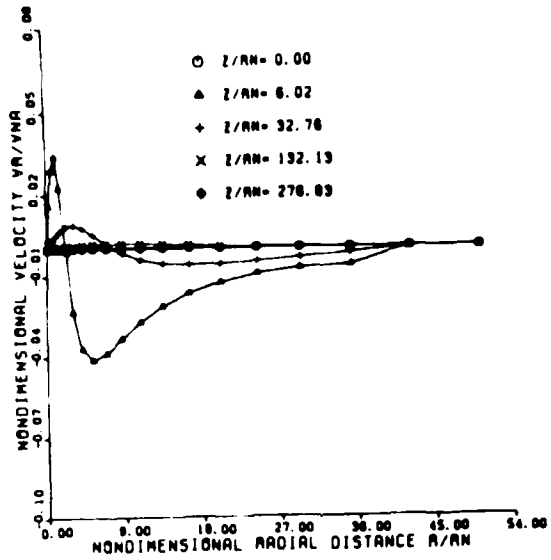

Figure A-1-2. Calculated radial velocity in experimental laminar coaxial jet system. VR is radial velocity, VNA average velocity at nozzle exit, Z is downstream distance, R is radial distance, and RN is nozzle radius (0.1 cm).

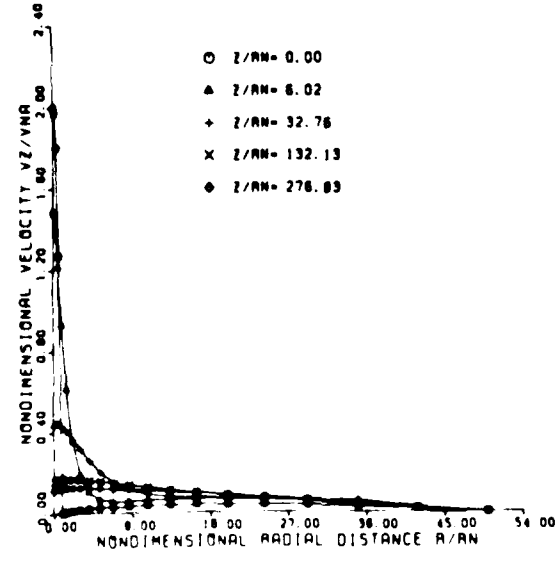

Figure A-1-3. Calculated axial velocity in experimental laminar coaxial jet system. For nomenclature see legend Figure A-1-2.

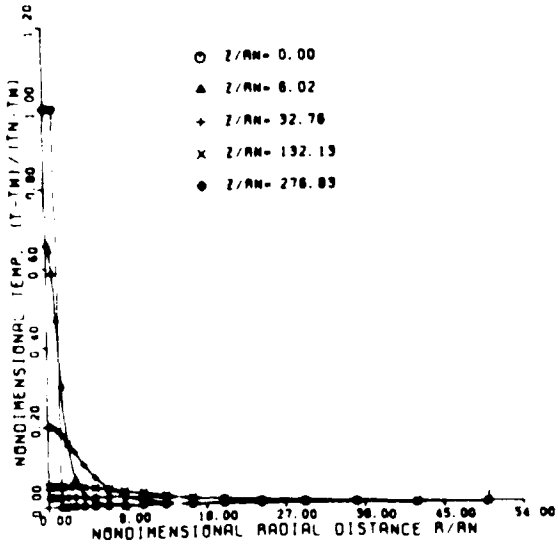

Figure A-1-4. Calculated temperature distribution in experimental laminar coaxial jet system. T is temperature, TW is wall temperature, and TN nozzle temperature. For other nomenclature see Figure A-1-2 legend.

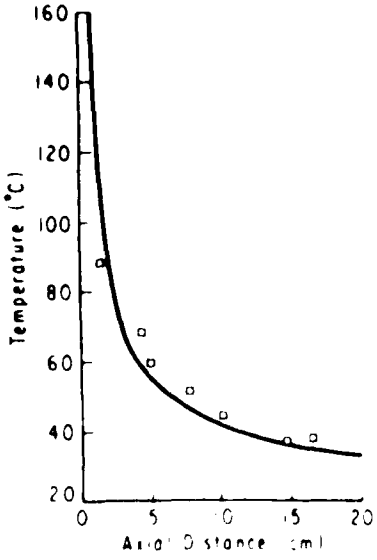

Figure A-1-5. Calculated and observed average jet temperature as a function of axial downstream distance in laminar coaxial jet.

b. Results.

A primary interest in the results presented here is measurement of the particle

binary aerosol after nucleation and condensation growth of the aerosol was completed. At the particle number concentrations produced in our experiments, coagulation was relatively unimportant over the relevant time scales; our measurements were concerned with growth times less than 1 s whereas characteristic coagulation times for the aerosol produced were > 10 s, even during homogeneous nucleation, according to our model calculations. As pointed out above, the sampling and dilution system used was adequate for accurate sampling of these aerosols.

The use of CO tracer permitted accurate determination of total dilution of the aerosol measured by the OPC. Particle number distributions were then calculated using the measured dilution factor. A confirmation of these measurements was provided by calculating the mass distributions from which the total mass concentration was in turn calculated. For those oils undergoing total condensation to aerosol, these mass concentrations agreed to within less than 5% with the total mass concentrations found from the accurate liquid oil and nitrogen feed rates.

A series of phthalate esters was used - dibutyl (DBP), dihexyl (DHP), and dioctylphthalate (DOP) - along with squalene (SQ) (spinacene) and oleic acid (OA), and their mixtures. For all but dibutyl phthalate, the vapor pressures were sufficiently low in the temperature field of the jet that all condensation growth was completed at axial distances greater than approximately 2 nozzle diameters. Measurements at downstream positions showed no change in particle size distributions, except for dibutyl phthalate.

Dibutyl phthalate has a sufficiently high vapor pressure that condensation growth was not complete at the usual sampling point at an axial distance of 20 cm from the nozzle. Figure A-1-6 shows the evolution of the particle number and mass distributions at axial downstream distances of 47.5, 70 and 100 nozzle diameters for a liquid oil feed rate of DBP of 0.00136 $cm^3 min^{-1}$ and 178 $cm^3 min^{-1}$ (298K, 1 atm., nitrogen carrier gas). The "mixing" ratio defined here is the liquid oil feed rate divided by the nitrogen carrier gas feed rate. The mixing ratio in this example is 7.64×10^{-6}. Figure A-1-7 shows the percentage of total mass concentration of DBP vapor condensed as aerosol as a function of downstream distance. Total number concentration is constant for the three positions at $4.6 \times 10^6 cm^{-3}$, as is consistent with growth of an aerosol solely by condensation.

Dihexyl (DHP) and dioctyl (DOP) phthalate have sufficiently low vapor pressures in the temperature field of the jet that condensation is complete at axial distances greater than approximately 20 nozzle diameters. An important aspect of particle formation and growth is the dependence of particle size distribution and its moments on the initial vapor concentration. Figures A-1-8 and A-1-9 show particle number and mass distributions for DOP and DHP respectively at 100 nozzle diameters (20 cm) downstream. In these measurements, nozzle temperature was 270°C, nitrogen feed rate was 178 $cm^3 min^{-1}$ at 298K, 1 atm., and liquid oil feed rate 0.00206, 0.0034 and 0.0051 $cm^3 min^{-1}$ (mixing ratios of 1.16×10^{-5}, 1.91×10^{-5} and 2.87×10^{-5}). In all cases, total mass concentration calculated from the measured particle size distributions agreed to within 7 % with mass balance based on feed rates.

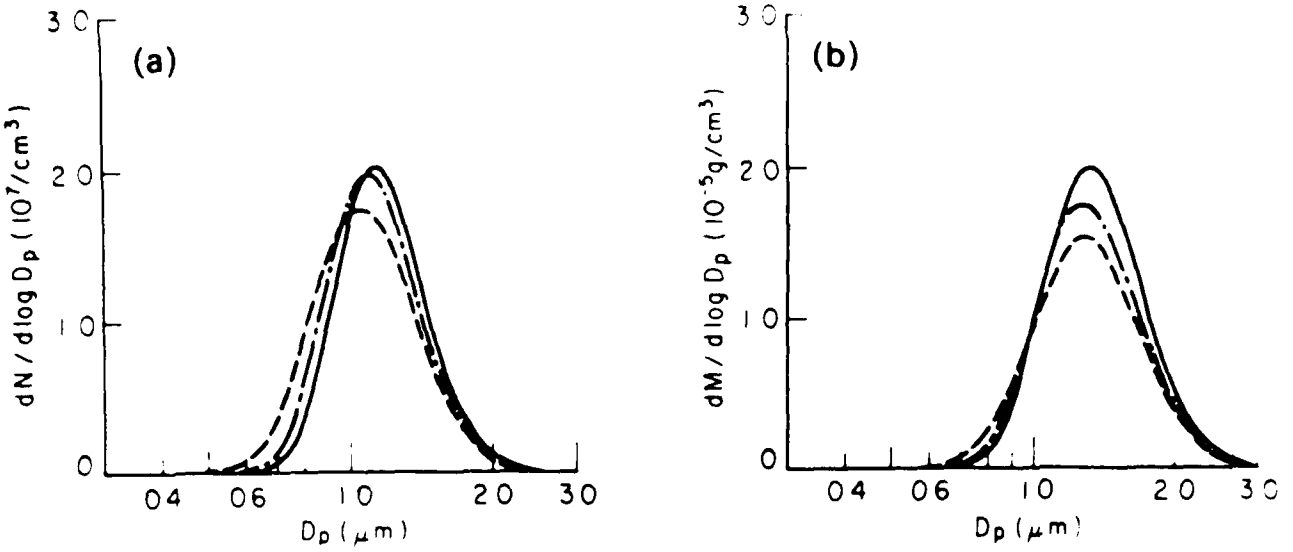

Figure A-1-6. Experimental results for dibutyl phthalate for evolution of particle number and mass distributions at axial downstream distances of 47.5 (---), 70.0 (-.-.) and 100.0 (____) nozzle diameters for mixing ratio of 7.64E-6.

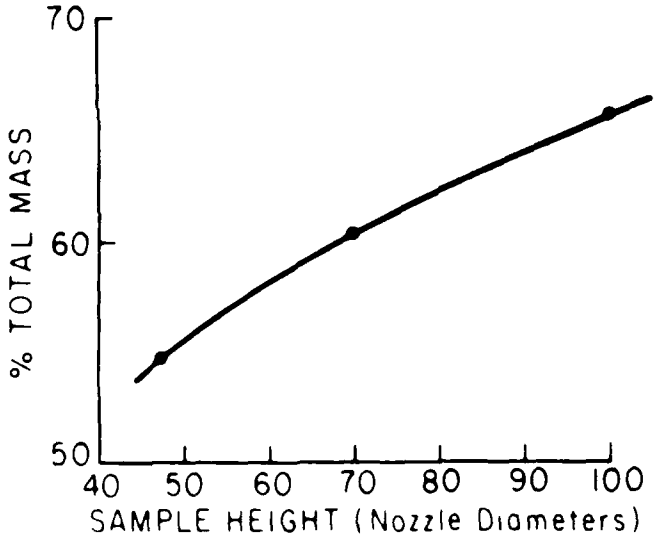

Figure A-1-7. Percentage of total mass concentration of dibutyl phthalate vapor condensed as aerosol as a function of axial downstream distances of 47.5, 70.0, and 100.0 nozzle diameters for mixing ratio of 7.64E-6.

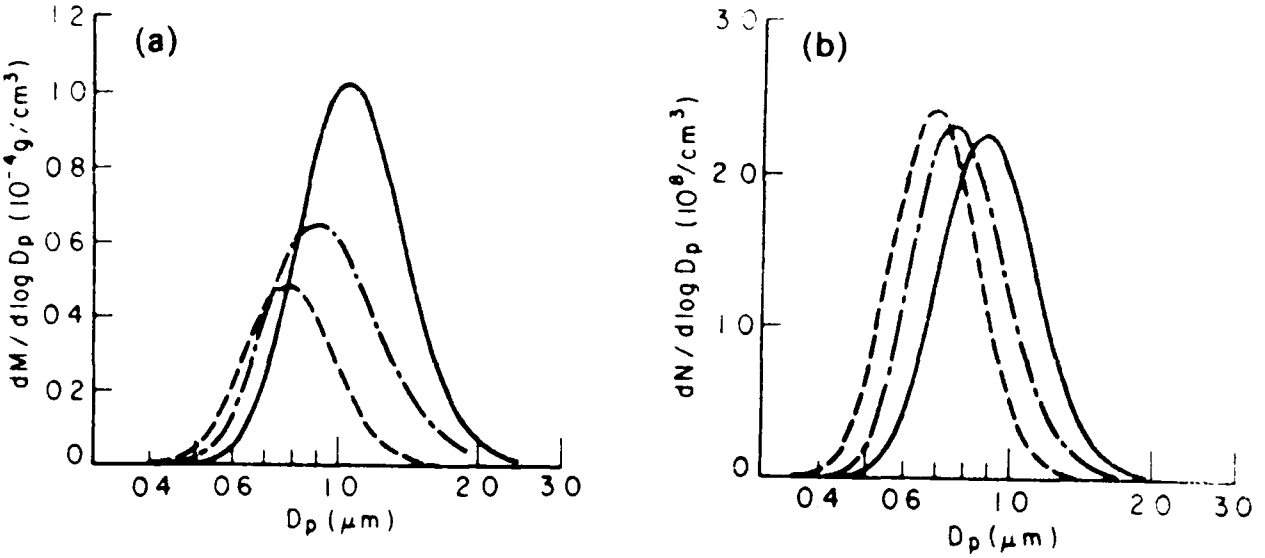

Figure A-1-8. Number and mass distributions for dioctyl phthalate with complete condensation of vapor to aerosol at downstream axial distance of 100.0. Nozzle diameters at mixing ratios of 1.16E-5 (---), 1.91 E-5 (-.-.-) and 2.87 E-5 (_____).

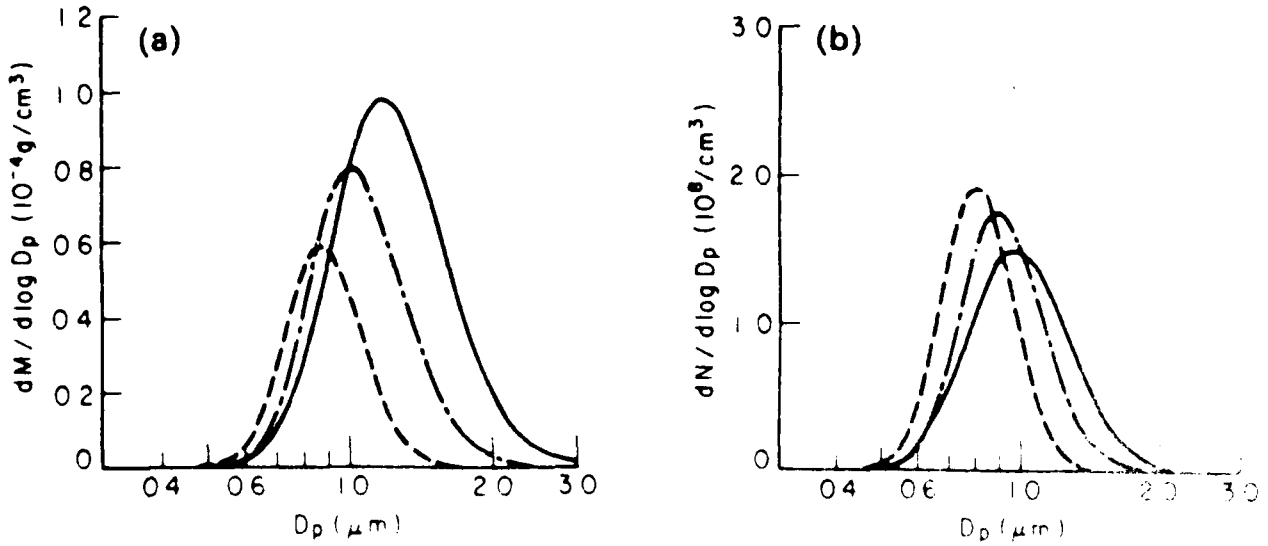

Figure A-1-9. Number and mass distributions for dinexyl phthalate [illegible] complete condensation of vapor to aerosol at downstream axial distance of 100.0 nozzle diameters at mixing ratios of 1.16E-5 (---), 1.91E-5 (-.-.-) and [illegible] (_____).

The data presented here are intended to illustrate the character of the results obtained from our experimental system. A complete presentation of binary aerosol data with a more complete analysis will be given in additional papers. In the next section partial analysis of some of the results presented will be given.

c. Analysis of results.

A complete analysis of experimental data obtained from the laminar coaxial aerosol jet would involve numerical solution of the spatially inhomogeneous dynamical equations for aerosol growth (e.g., Brock[5]) coupled with the solution of equations (A-1-1)-(A-1-3). An analysis of this stystem considering only coagulation of an aerosol was published earlier (Kajuichi and Brock). Here an approximate analysis will be given by considering an average over the aerosol jet at a given downstream distance. With justifiable neglect of axial and radial diffusion of particles, the average properties of the aerosol jet at a downstream position will be modeled by obtaining, from the numerical solution of equations (A-1-1)-(A-1-3), the average axial transport time and temperature.

A dynamical model for evolution of the particle size distribution can be developed along these lines, but such a program will be carried out elsewhere. Here we present results based on an approximate moment formulation of the spatially averaged (at a downstream cross-section) single component particle size distribution $n(x,t)$. The number of particles having masses in the range x, dx at time t is $n(x,t)$

being the axial downstream distance) is $n(x,t)dx$. We study the evolution in this time through the moments of $n(x,t)$:

$$M_0 = \int_0^\infty n(x,t)dx \qquad \text{(A-1-4)}$$

$$M_1 = \int_0^\infty xn(x,t)dx \qquad \text{(A-1-5)}$$

$$M_2 = \int_0^\infty x^2 n(x,t)dx \qquad \text{(A-1-6)}$$

$$C + M_1 = \text{constant}. \qquad \text{(A-1-7)}$$

where C is the vapor mass concentration. For a single component aerosol, the evolution equations are obtained from the equation for $n(x,t)$ appropriate for the experimental conditions studied:

$$\partial n/\partial t = -(\partial/\partial x)(\psi n) + 1/2\ (\partial^2/\partial x^2)(\alpha n) + \dot{R} \qquad \text{(A-1-8)}$$

where ψ is the particle growth rate, α is the diffusion coefficient of particle growth, and $\dot{R}$ the nucleation rate. Neglecting the diffusion term and evaporation, one obtains from (4)-(6) and (8):

$$dM_0/dt = R \qquad \text{(A-1-9)}$$

$$dM_1/dt = \int_0^\infty \psi n dx + x_c R \qquad \text{(A-1-10)}$$

$$dM_2/dt = 2\int_0^\infty x\psi n dx + x_c R \qquad \text{(A-1-11)}$$

Also:

$$d(M_1+C)/dt = 0 \qquad \text{(A-1-12)}$$

where the nucleation process is assumed to produce a single time dependent nucleus size, $x_c(t)$:

$$\dot{R} = \delta(x-x_c(t))R$$

where δ is the delta function and R is the nucleation rate. R is calculated according to the classical theory of Becker-Doring-Zeldovich (e.g. Abraham[1]).

The particle growth rate has the form (Davis et al.[7]):

$$\psi = (\pi D_p^2/4)\upsilon_1 C_v (S-e^{Ke})\pi^{1/2} Kn \left[1 + \frac{Kn\,\frac{4}{3}\,Kn + 1.016}{4\,Kn/3+1}\right]^{-1}$$

where D_p is particle diameter, υ_1 mean thermal speed of vapor molecules, C_v the concentration corresponding to the bulk vapor pressure, S the supersaturation ratio, Ke the Kelvin and Kn the Knudsen numbers. Coagulation is unimportant for the conditions of this study.

Equations (A-1-9)-(A-1-12) are not a closed set for the moments. Closure is only possible in the free molecule regime if ψ does not contain the Kelvin evaporation term; this situation does not exist for our experimental system.

Various lumped parameter and mean growth models of nucleation and growth have been proposed (e.g. Takahashi[15]). However, we have found that such models cannot explain our experimental observations. Closure of equations (A-1-4)-(A-1-12) is effected here by introducing an assumed particle size distribution. This procedure is similar to methods proposed previously for coagulation and condensation (e.g. Clark[6]). We have used the lognormal distribution in these simulations, although other distributions may be superior for this purpose. For simple condensation

and evaporation processes, comparison between the lognormal solutions and analytical solutions shows that the lognormal gives a reasonable prediction of the progression of the mean and modal values in time, but the second moment is in error with a magnitude dependent on the growth law.

The lognormal distribution has the form:

$$n(x,t) = (M_0 / \sqrt{2\pi} \ln\sigma_g \bar{x}) e^{-(\ln x - \ln \bar{x})^2 / 2\ln^2 \sigma_g} \qquad \text{(illegible)}$$

The parameters, $\bar{x}(t)$, $\sigma_g(t)$ are time dependent and can be expressed in terms of M_1 and M_2:

$$M_1 = M_0 \, m e^{1/2 \ln^2 \sigma_g} \qquad \text{(A-1-14)}$$

$$M_2 = M_0 \, m^2 e^{2\ln^2 \sigma_g} \qquad \text{(A-1-15)}$$

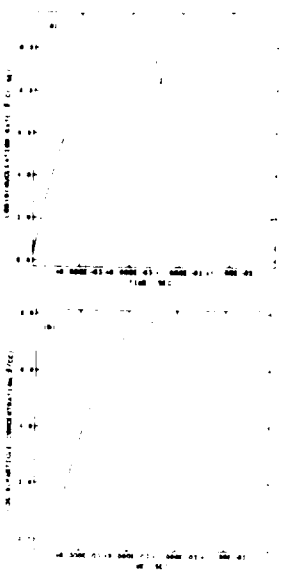

Figure A-1-10. Calculated (a) nucleation rates and (b) particle number concentrations for dioctyl phthalate [illegible] phthalate (DHP) condensing in experimental [illegible] axial jet for conditions described in Figures [illegible] through A-1-5. Mixing ratio = 2.1 [illegible] , DHP [illegible].

With these these definitions, equations (A-1-9)-(A-1-12) are closed and may be solved in integral form. Such solutions provide at least a qualitative explanation of our experimental results. This model has also been extended to multicomponent aerosols.

Figure A-1-10 shows the calculated nucleation rates and particle number concentration as a function of t(z) for single component aerosols of DOP and DHP at a mixing ratio of 2.1×10^{-5} in the laminar coaxial jet from equations (A-1-9)-(A-1-15). Figure A-1-11 displays the corresponding geometric mass mean particle diameters and standard deviations. It can be seen that the nucleation process is completed in times of the order of a few milliseconds.

The characteristics of the two aerosols produced in the comparison of Figures A-1-10 and A-1-11 are the result of competitive rate processes: nucleation and condensation. Upon initiation of nucleation, all of the available vapor goes to the creation of particles. As the particle concentration increases, the vapor begins to condense on existing particles as well as to contribute to creation of new particles. The condensation rate increases and eventually condensation depletes the vapor bringing about a rapid decrease in new particle formation by nucleation.

The cooling rate of vapor in the jet plays a key role in determining the maximum nucleation rate and hence the number of particles produced. Maximum cooling rates in our experiments were of the order of 10^4 Ks^{-1}. Large cooling rates permit very rapid increases in nucleation

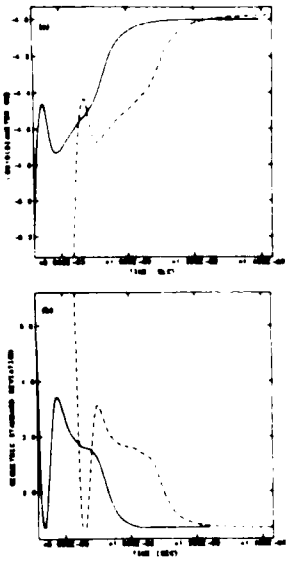

Figure A-1-11. Calculated (a) mass average particle diameters and (b) standard deviations for dioctyl phthalate (DOP) and dihexyl phthalate (DHP) condensing in experimental laminar coaxial jet for conditions described in Figures A-1-3 through A-1-5. Mixing ratio = 21 E-5. Key: DOP (_____), DHP (----).

rates while at the same time the total condensation rates increase much less rapidly. In general, larger cooling rates produce higher particle number concentrations and, for a fixed initial vapor concentration, smaller ultimate mean particle sizes. Turbulent jets create much larger cooling rates than those found in laminar jets; consequently, for the same initial vapor concentrations and other conditions, turbulent jets produce much higher particle number concentrations and smaller mean particle sizes than are found here for a laminar jet.

In the laminar coaxial jet, particle growth continues long after cessation of nucleation. The plots of mean particle diameter and standard deviation shown in Figure A-1-11 indicate the apparent

complexity of the growth process, although the theory used here is admittedly approximate. The shoulders in the curves for particle diameter may be due to the existing large nucleation rates and consequent rapid introduction of smaller particles, which, however, rapidly increase in size at the high supersaturation prevailing at that time. At the times of these shoulders, the standard deviations are seen to exhibit similar changes. The standard deviations are seen to decrease during late stages of particle growth. This agrees with the well-known fact that condensation growth of an aerosol produces a narrowing of its distribution.

In this study, as well as in previous studies of nucleation and particle growth, it is found that, other conditions being the same, less volatile species yield aerosols with higher number concentrations and smaller mean particle sizes. Figure A-1-12 shows a comparison of calculated and observed total particle number concentrations for DOP and DHP as a function of mixing ratio. As is evident, the qualitative trend is reproduced by the model, although there is a quantitative difference. This difference may arise from several sources. Classical nucleation theory is used in the calculation, although the classical theory is known to diverge widely from experiment at the high nucleation rates believed to exist in our experiments. A decrease of 10^4 in the nucleation rate calculated by the classical theory for DHP would bring about a much better quantitative comparison. Also, the theory applied here is approximate and conditions are assumed constant over a cross-section of the vapor-aerosol jet.

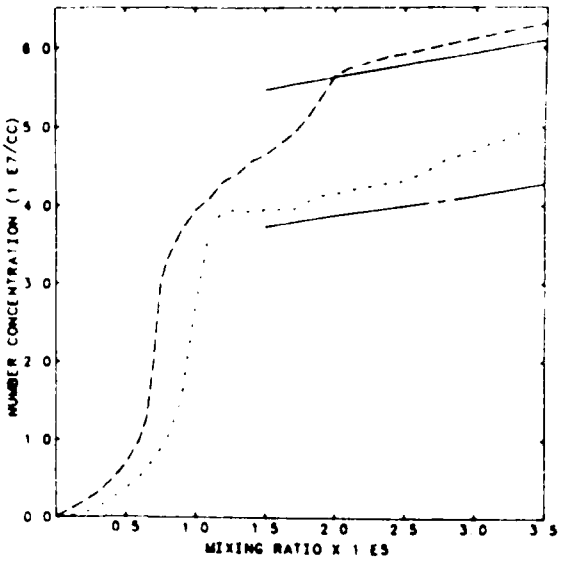

Figure A-1-12. Comparison of calculated and observed particle number concentrations, with all vapor condensed to aerosol, for dioctyl phthalate and dihexyl phthalate aerosols in experimental laminar coaxial jet as function of mixing ratio. Experimental conditions same as described for Figures A-1-3 through A-1-5. Key: DOP calculated (- - -), DOP observed (_____), DHP calculated (----), DHP observed (__ - __)

The extension to binary aerosols follows the procedure outlined above. The binary density function $n_{12}(x_1, x_2, t)$ is defined such that $n_{12}(x_1, x_2, t)\, dx_1\, dx_2$ is the number of particles having masses, x_1, of species 1 and x_2 of species 2 in the range dx_1, dx_2 about x_1 and x_2.

Moments may be defined:

$$M_{ij} = \int_0^\infty \int_0^\infty (x_1 + x_2)^i\, n_{12}(x_1, x_2, t)\, dx_1\, dx_2$$

The evolution of these moments in time is obtained from the evolution equation for $n_{12}(x_1, x_2, t)$ appropriate to the experimental conditions:

$$\frac{\partial n_{12}}{\partial t} = -\frac{\partial}{\partial x_1}(\xi_1 n_{12}) - \frac{\partial}{\partial x_2}(\xi_2 n_{12}) + R_{12}$$

The moment equations studied have the form:

$$\frac{dM_{00}}{dt} = R_{12}$$

$$\frac{dM_{10}}{dt} = \int_0^\infty \int_0^\infty \xi_1 n_{12}(x_1, x_2, t)\,dx_1 dx_2 + x_1 R_{12}$$

$$\frac{dM_{01}}{dt} = \int_0^\infty \int_0^\infty \xi_2 n_{12}(x_1, x_2, t)\,dx_1 dx_2 + x_2 R_{12}$$

$$\frac{dM_{20}}{dt} = 2\int_0^\infty \int_0^\infty x_1 \psi_1 n_{12}(x_1, x_2, t)\,dx_1 dx_2 + x_1 R_{12}$$

$$\frac{dM_{02}}{dt} = 2\int_0^\infty \int_0^\infty x_1 \psi_2 n_{12}(x_1, x_2, t)\,dx_1 dx_2 + x_2 R_{12}$$

ξ_1 and ξ_2 are the particle growth rates for species 1 and 2. Details may be found in the references cited in Section II. R_{12} is the classical binary nucleation rate, a straightforward, but, unfortunately, limited extension of the single component classical nucleation theory cited above.

Closure of the moment equation above is obtained by assuming a lognormal product for n_{12}:

$$n_{12}(x_1, x_2, t) = (M_0/2 \ln\sigma_1 \ln\sigma_2 x_1 x_2) \cdot$$
$$\exp(-(\ln x_1 - \ln\bar{x}_1)^2/2\ln^2\sigma_1) \cdot$$
$$\exp(-(\ln x_2 - \ln\bar{x}_2)^2/2\ln^2\sigma_2)$$

a consistent density function for binary internally mixed aerosols as in the present study.

Detailed presentation of results is too lengthy to repeat here. Some limited comparisons are given here of predicted and experimental values of the total number concentration, M_{00} as shown in Figures A-1-13 and A-1-14 for DHP in DOP and DHP in SQ (squalane). In view of the well-known inadequacies of current binary classical nucleation theory, the agreement exhibited in these figures is surprisingly good. It should be noted that these are independent comparisons with no adjustable parameters.

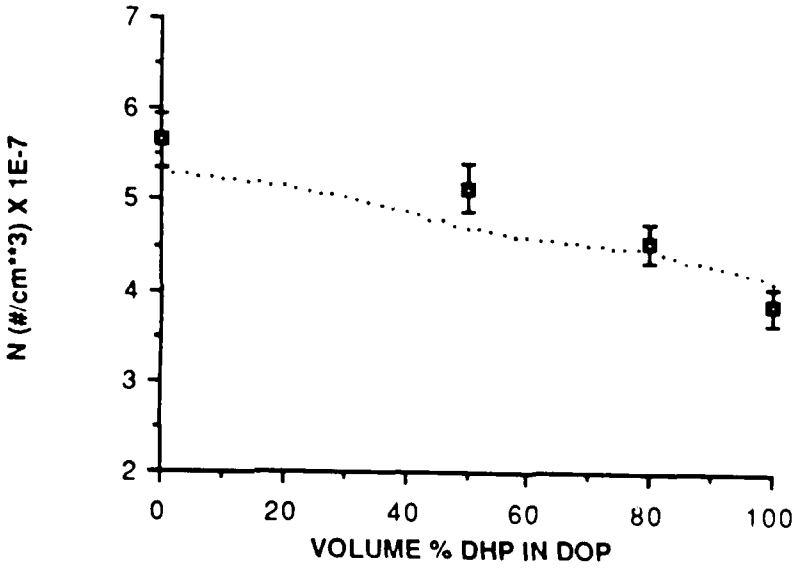

Figure A-1-13. Asymptotic number concentration as a function of volume % dihexyl phthalate (DHP) in dioctyl phthalate (DOP). ..... theory; points with error bars, experimental

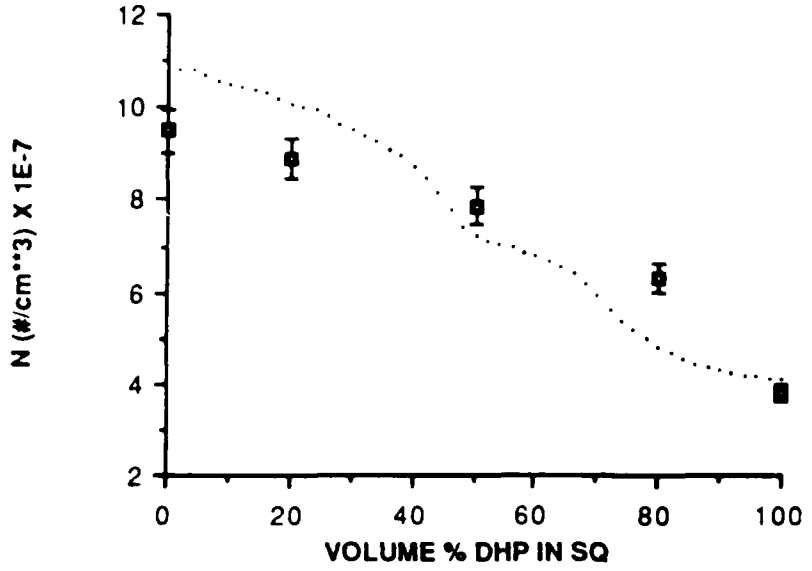

Figure A-1-14. Asymptotic number concentration as a function of volume % dihexyl phthalate (DHP) in squalane (SQ). ..... theory; points with error bars, experimental.

A-2. Aerosol growth: Ostwald ripening.

Subsequent to their appearance by homogeneous nucleation from a monomer, particles grow by coagulation and condensation/evaporation processes. Such growth has been titled Ostwald ripening (Ostwald[29], Liesegang[23]). Numerous studies (e.g., Lifshitz and Slyozov[24], Wagner[32], Kahlweit[20,21], Binder[16], Venzl[31], Marqusee and Ross[27]) have been concerned with the existence of asymptotic limit distributions arising from Ostwald ripening by the condensation/evaporation process. We have obtained results from numerical investigations of this aspect of Ostwald ripening. We have noted specifically limitations inherent in previous work, owing to assumptions used in the model of the physical system, and described the dynamics of approach to the asymptotic limit distributions for continuum and kinetic (free molecule) growth regimes.

3. Theory.

In [illegible]

equation for the part [illegible]

[illegible]

$$\frac{\partial n(x,t)}{\partial t} = \cdots \frac{\partial}{\partial x} \cdots$$

where

$$\cdots(x,t) = A \cdots x/s-\exp \cdots x^{1/3} \cdots$$

$n(x,t)$ is the [illegible] of particles [illegible]

$\cdots$ is the growth rate of a particle (mass per unit time). Equations 1' and (A-2-c) are appropriate for describing the [illegible] tion process for dilute monomer vapor in inert [illegible] the supersaturation ratio; $K/x^{1/3}$ is the Kelvin [illegible] [illegible] with the motion term, [illegible] the third [illegible], and [illegible]

The form of $A(x)$ depends on the [illegible] is, first of all, the question of [illegible] particle growth, a topic receiving considerable [illegible] Fellenhof and Fuchs[13], Mothes-Weber and Allen[14], [illegible] Kirpatinsky[15], Marquis and Pruppacher[16]. [illegible] the [illegible] [illegible]

$$A_c(x) = 2\pi D_p D C_v [1 + D_p \sqrt{1/2 \pi M_0 \langle D_p \rangle}],$$

where D_p is the particle diameter: $x = (1/6)\pi D_p^3 d$; D, the diffusion coefficient of monomer vapor in host gas; M_0, the particle number concentration; $\langle D_p \rangle$, the mean particle diameter; and C_v, the equilibrium mass concentration of monomer vapor for a plane interface. The term in brackets in this expression accounts for competitive effects. For particle sizes restricted to those appropriate for aerosols and for sufficiently small number concentrations, e $D_p \sqrt{1/2 \pi M_0 \langle D_p \rangle} \ll 1$ (and apparently competitive effects can be neglected). Alternatively, the equilibirium volume fraction (Marqusee and Ross[27]), $\sigma \sim (C_{initial} - C_v)d$ fulfills the condition $\sigma \ll 1$. For situations where e is not small for aerosols, competitive effects become important; however, this corresponds to larger values of M_0, for which Equation (A-2-1) is no longer the correct evolution equation, and the coagulation process must be included. The importance of competitive growth for aerosols when coagulation is present has not yet been examined completely, although this is discussed next in Section A-3.

In any event, our simulations are restricted to the regime where competitive effects may be regarded as negligible. For continuum growth, therefore:

$$A_c(x) = 2\pi D_p D C_v \quad {}_c x^{1/3}. \qquad \text{(A-2-3)}$$

For kinetic (free molecule) growth:

$$A_K(x) = 1/4 \pi D_p \left(\frac{8 \cdot T}{m_1}\right)^{1/2} \quad C_v \quad {}_k x^{2/3}. \qquad \text{(A-2-4)}$$

Here, m_1 is the monomer molecular mass and $\cdot T$ the thermal energy.

Equation (A-2-1) is coupled to the conservation equation for monomer:

$$C_v \frac{ds}{dt} = -\int_{x^*}^{\infty} \dot{x}(x,t)n(x,t)dx - x^* \dot{x}(x^*,t)n(x^*,t), \qquad (A-2-5)$$

x^* is the mass of the smallest particle that obeys the growth law, Equation (A-2-2).

Two important moments of $n(x,t)$ are the total particle number concentration, M_0, and mass concentration, M_1. From (1) and (5):

$$\frac{dM_0}{dt} = \dot{x}(x^*,t)n(x^*,t). \qquad (A-2-6)$$

$$\frac{d}{dt}(C_v s + M_1) = 0. \qquad (A-2-7)$$

Equation (A-2-7) reflects the conservation of total mass concentration.

Equations (A-2-1) and (A-2-5) constitute a nonlinear integro-differential equation for $n(x,t)$. The asymptotic properties of (A-2-1) and (A-2-5) with the linearization:

$$\exp(K/x^{1/3}) \sim 1 + K/x^{1/3} \qquad (A-2-8)$$

and $x^* = 0$, were apparently first investigated correctly by Lipschitz and Slyozov[24] (LS); subsequent investigations have not modified the LS results. Asymptotic solutions are obtained in terms of the similarity variables:

$$\eta = 3 \ln (D_p/D_{pc}(t)),$$

$$\xi = D_p/D_{pc},$$

η is implicitly related to t through the dependence, $D_{pc}(t)$. D_{pc} is the critical particle diameter separating the regions of evaporation and condensation. From (2):

$$D_{pc} = 4\sigma_1/\kappa T \ln s \qquad (A-2-9)$$

or, with the linear approximation, Equation (A-2-8):

$$D_{pc} \sim \sigma_1/\kappa T(s-1).$$

The distribution is transformed with the assumption that asymptotically ($t \to \infty$):

$$n(x,t) = (2/\pi d)M_0(t)P(\xi)/D_{pc}D_p^2. \qquad (A-2-10)$$

For the continuum growth law: $A(x) \sim x^{1/3}$, and the LS result is

$$P(\xi) = \frac{3^3 e}{2^{5/3}} \exp[-1/(1-2\xi/3)]/(\xi+3)^{7/3}(3/2-\xi)^{11/3} \qquad (A-2-11)$$

and $M_0 \sim 1/t$, valid for the linearization, Equation (A-2-8).

For kinetic (free molecule) growth: $A(x) \sim x^{2/3}$, and it is easy to show that

$$P(\xi) = 24\xi \exp[-3/(2-\xi)]/(2-\xi)^5 \qquad (A-2-12)$$

and $M_0(t) \sim t^{-1/2}$, valid for the linearization, Equation (A-2-8).

We report here results of numerical investigations of Equations (A-2-1)-(A-2-5) with and without the linearization, Equation (A-2-8), for both continuum and kinetic (free molecule) growth laws. In addition, the important effect on approach to the asymptotic limit, Equation (A-2-10), of the dispersion of the initial size distribution is noted. The numerical technique employed for solution of (A-2-1) and (A-2-5) is a combined finite-difference method that we have described elsewhere (Seaver and Peterson).

Seaver and Peterson reported a numerical solution of (A-2-1) and (A-2-5) with linearization, Equation (A-2-8), for the continuum

growth law with special restrictions on initial conditions. We will introduce none of these restrictions.

In our numerical simulations, the initial distribution is defined in terms of the distribution with respect to particle diameter and have the form:

$$f(D_p, t=0) = f_0(D_p; \bar{D}_p, \sigma_g),$$

where $\bar{D}_p$ and σ_g are, respectively, the mean and geometric standard deviation of a lognormal distribution. The lognormal distribution has been suggested (Granquist and Buhrman[19]) to describe experimental size distributions from various homogeneous nucleation processes.

Table A-2-1 summarizes the various cases studied in our simulations. Cases 1-6 cover the continuum growth law, $A_c(x) \propto x^{1/3}$, with the indicated variations in the Kelvin term and initial particle size distribution. The kinetic growth law, $A_k(x) \propto x^{2/3}$, is applied in cases 7-8, where principally the effect of linearization of the Kelvin term and the existence of the asymptotic limit, Equation (A-2-12), were studied. In all cases, the value of $C_v s + M_1$ is the same.

The questions we wish to examine in this study are: (1) What are the dynamics of the approach to the asymptotic limit? (2) What is the role of initial particle size dispersion on approach to the asymptotic limit distribution? (3) What is the effect of using the normal form for the Kelvin effect in particle growth, rather than the approximation, Equation (A-2-[illegible]), that is the usual form in Equation (A-2-[illegible]), for [illegible]

TABLE A-2-1: Cases Studied in Simulation of Ostwald Ripening

Case	S	M_1(gm/cm^3)[a]	M_0(#/cm^3)[a]	g	$\bar{D}_p$ (μm)	Kelvin effect	growth law[a]
1	1.1	1.0 x 10^{-7}	2.25594x10^7	1.4	0.2	linear Eq. (6)	continuum
2	1.1	1.0 x 10^{-7}	2.25594x10^7	1.4	0.2	nonlinear Eq. (2)	continuum
3	1.1	1.0 x 10^{-7}	1.30565x10^7	3.0	0.2	linear Eq. (6)	continuum
4	1.1	1.0 x 10^{-7}	1.30565x10^7	3.0	0.2	nonlinear Eq. (2)	continuum
5	1.10	1.0 x 10^{-7}	1.87755x10^7	2.0	0.2	nonlinear Eq. (2)	continuum
6	1.12	2.3137x10^{-7}	1.65999x10^7	5.0	0.09	nonlinear Eq. (2)	continuum
7	1.1	1.0 x 10^{-7}	2.2559x10^7	1.4	0.2	nonlinear Eq. (2)	kinetic
8	1.1	1.0 x 10^{-7}	2.2559x10^7	1.4	0.2	linear Eq. (6)	kinetic

[a] The numerical values used for parameters in the study:
C_v=3.84E-6g/cm^3; t=423K; =20 dyn/cm; d=1.0 g/cm^3; m_1=6.48E-22g.

b. Results.

Figures A-2-1 - A-2-3 show the approach to the asymptotic limit distribution, Equation (A-2-1) with continuum growth, $A(x) \sim x^{1/3}$, for cases 1-4 of Table A-2-1. Figures A-2-1 and A-2-2 differ only in that the linearization, Equation (A-2-8), is employed in obtaining the results of Figure A-2-1, while the full nonlinear term is used in Figure A-2-2. In both cases, the asymptotic limit distribution, Equation (A-2-11), is found for nondimensional times, $\tau \sim 15$ within the limits of accuracy of our numerical simulations. In Figure A-2-3, cases 3 and 4 are presented for relatively large initial particle size dispersion, $\varepsilon_g = 3$. As is evident, the asymptotic limit, Equation (A-2-12), is not achieved at $\tau \sim 15$, as was found for cases 1 and 2 where $\varepsilon_g = 1.4$. Our estimates indicate that much larger values of (~ 100) would be necessary to achieve the asymptotic limit distribution, Equation (A-2-12).

The positive moments M_0, M_1, M_2, M_3, M_4, M_5, and M_6 as a function of simulation time are shown in Figures A-2-4 through A-2-7, where

$$M_i = \int_{x^*}^{\infty} x^i n(x,t)dx.$$

The lower bound corresponds to a particle diameter of 0.001 μm.

In Figure A-2-4, M_0 and M_1 are shown for the continuum and kinetic growth laws for all cases in Table A-2-1. It is easily seen that there is an initial "adjustment phase" during which M_0 remains constant. This reflects the finite time for evaporating particles to reach x^* so that M_0 can begin to decrease according to Equation (A-2-[illegible]). For our assumed initial particle size distributions, $n(x^*,t=0)$ is exponentially

- - - - - - - t = 0 (τ =0)
—— - —— - t=0.01 sec (τ =1.828)
—— - —— t=0.05 sec (τ =3.768)
—— o-o-o-o t=0.4 sec (τ =4.913)
———— Asymptotic similarity solution, Equation (A-2-11)

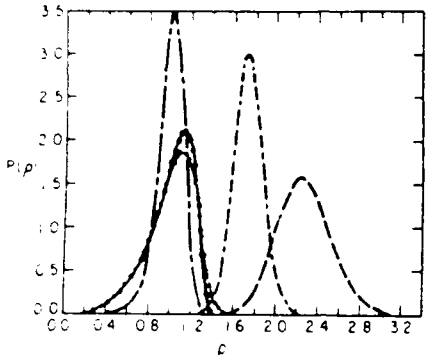

Figure A-2-1. Approach to asymptotic limit distribution for continuum growth law, case 1, Table A-2-1.

- - - - - - - t = 0 (τ =0)
—— - —— - t=0.2 sec (τ =2.35)
—— - —— t=0.05 sec (τ =3.65)
—— o-o-o-o t=0.40 sec (τ =4.72)
———— Asymptotic similarity solution, Equation (A-2-11)

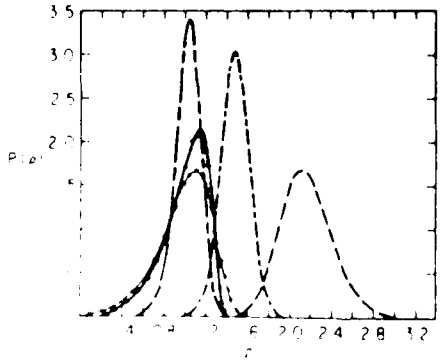

Figure A-2-2. Approach to asymptotic limit distribution for continuum growth law, case 2, Table A-2-1.

Case 3:

- - - - - - - t = 0 (ξ=0)
—— - —— - t=0.2 sec (ξ=4.81)

Case 4:

——..——... t=0.40 sec (ξ=5.74)
^ ^ ^ ^ ^ ^ t=15000 sec (ξ=15.35)
———————— Asymptotic similarity solution, Equation (A-2-11)

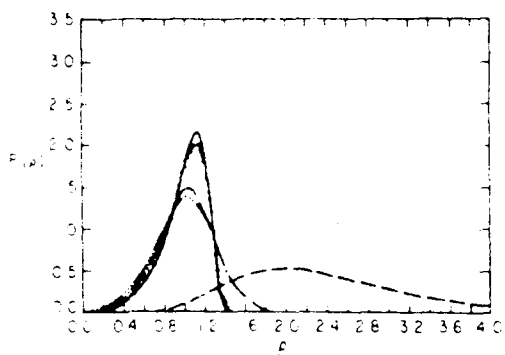

Figure A-2-3. Approach to asymptotic limit distribution for continuum growth law, cases 3 and 4, Table A-2-1.

ooooooooo case 1 (continuum growth)
————————— case 2 (continuum growth)
———— —— case 4 (continuum growth)
^^^^^^^^^^ case 5 (continuum growth)
|_| |_| |_| case 6 (continuum growth)
—— - - ——— cases 7, 8 (kinetic growth)

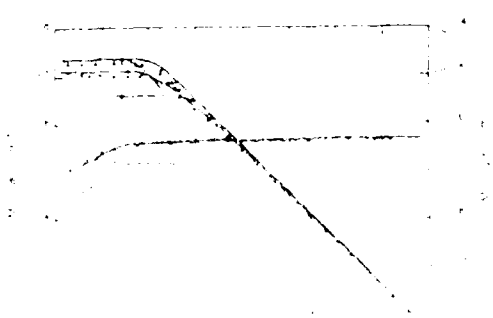

Figure A-2-4.

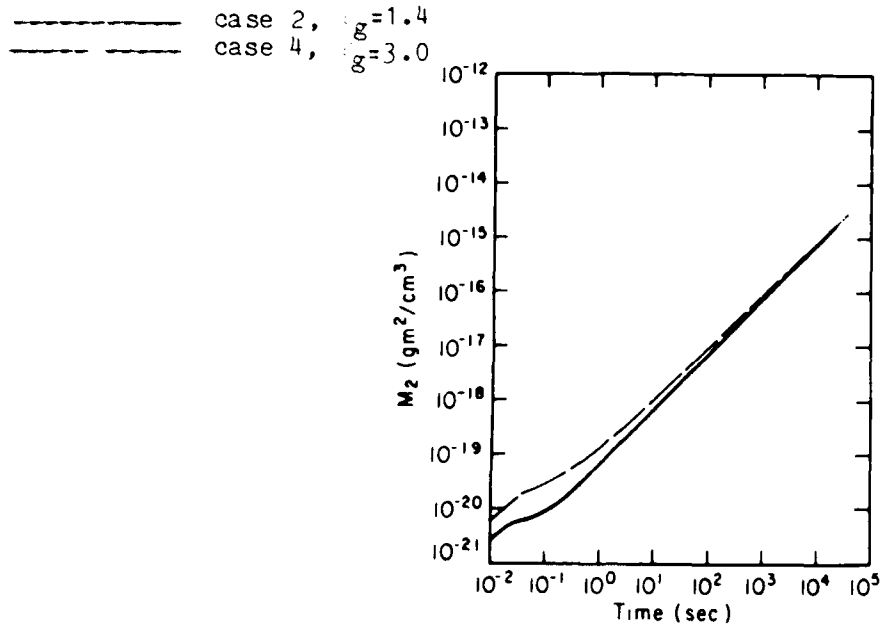

Figure A-2-5. Second moment, $M_2(t)$, as a function of time for continuum growth.

zero and remains so until the evaporation "wave front" reaches x^*. Cases 1-6 and 7-8 all have the same value of $(C_v s+M_1)$, Equation (A-2-3), so that the LS theory predicts a universal behavior as t --> ∞ and for continuum growth, $M_0 \sim 1/t$. For kinetic growth, $M_0 \sim t^{-3/2}$ asymptotically. This is confirmed in Figure A-2-4.

For ε_g=1.4, for continuum growth, $M_0 \sim 1/t$ for simulation times t>1 sec (->15). Much longer times are required for ε_g=3.0 and ε_g=5.0, as evident in Figure A-2-4. As is also evident from Figure A-2-4, M_1 achieves a universal quasistationary state for cases 1-6, and does this more rapidly than M_0 assumes its asymptotic state.

According to the LS theory for the linearized Kelvin term, Equation (A-2-3), the moments M_i, are easily shown to have the following time dependence:

$$M_i \sim t^{\alpha(i-1)}, \quad i = 0, \pm 1, \pm 2, \ldots, \qquad (A\text{-}2\text{-}14)$$

where

$\alpha = 1$ continuum grwoth;

$\alpha = 3/2$ kinetic (free molecule) growth.

Some of these positive moments are shown in Figures A-2-5 through A-2-7 for continuum growth, and are found numerically to follow the relation, Equation (A-2-14), for long times. It should be noted that M_1 obeys (A-2-14) strictly when but a single particle remains in the system, a state that can never be obtained in an infinite system. As expected, the larger the initial dispersion in particle size, the longer the time necessary for the moments to achieve the asymptotic state.

---------- case 2, σ_g=1.4
—— —— case 4, σ_g=3.0

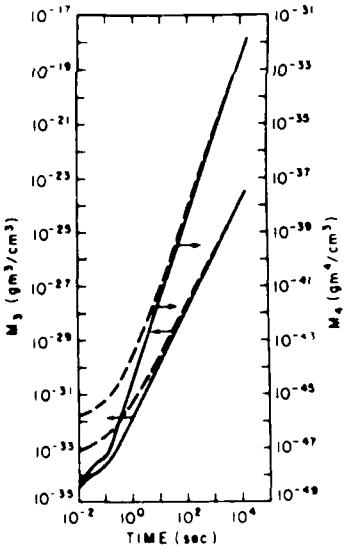

Figure A-2-6. Third and fourth moments, $M_3(t)$ and $M_4(t)$, as a function of time for continuum growth.

———————— case 2, ε_g=1.4
— — — — — case 4, ε_g=3.0

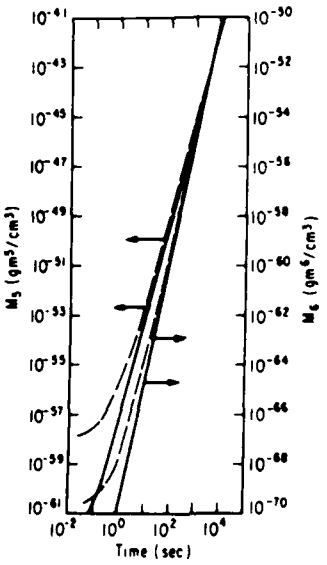

Figure A-2-7. Fifth and sixth moments, $M_5(t)$ and $M_6(t)$, as a function of time for continuum growth.

For continuum growth, the effect of the linearization, Equation (A-2-8), on the approach to the limit, Equation (A-2-11), is seen in Figures A-2-8 and A-2-9 where the distribution function $3xn(x,t)$ is plotted as a function of particle diameter. In these figures, for $t \sim 1$ sec, $D_{pc} \sim \langle D_p \rangle$, the mean particle diameter. Therefore the region to the left of the mode in each distribution represents evaporating particles. The nonlinear Kelvin term in Equation (A-2-2) at x^* is much greater than the linearized term, Equation (A-2-8): $e^{10} >> 11$. This causes the distribution for the nonlinear term for long times to be smaller than the corresponding distribution with the linear approximation, Equation (A-2-8). As can be seen from Figure A-2-8 for continuum growth, this is not true for relatively small times.

Clearly, for particle diameters less than the order of the Kelvin diameter, the linearization, Equation (A-2-8), is not at all an acceptable approximation. Therefore, the basis for the development of the LS theory, Equation (A-2-8), is physically unrealistic, particularly in view of the fact that particles disappear at some very small particle size, where Equation (A-2-6) is incorrect. However, we find the similarity solutions, based on the linearization, Equation (A-2-8), to yield good approximations to the correct nonlinear development according to Equation (A-2-2). The explanation for this is as follows.

We find for the nonlinear and linear cases for both kinetic and continuum growth laws for long times that

$$\frac{dM_0}{dt}\ \text{nonlinear} \gg \frac{dM_0}{dt}\ \text{linear}. \qquad \text{(A-2-15)}$$

———— case 1, linearized Kelvin term, Equation (A-2-8)
. . . . . case 2, nonlinear Kelvin term, Equation (A-2-2)

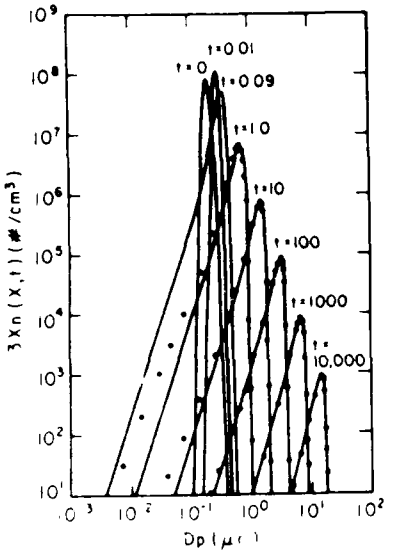

Figure A-2-8. Effect of linearization of Kelvin term on evolution of number distribution function 3xn(x,t) for continuum growth law for cases 1 and 2, Table A-2-1.

---------- case 3, linearized Kelvin term, Equation (A-2-8)
. . . . . case 4, nonlinear Kelvin term, Equation (A-2-2)

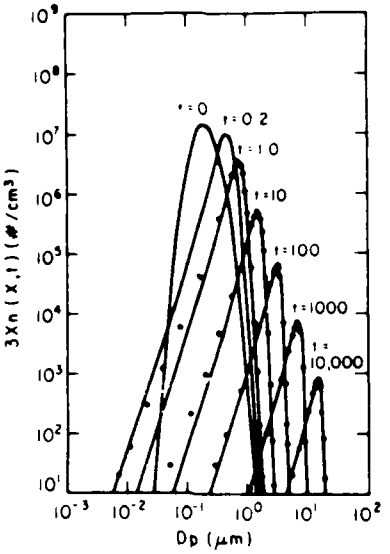

Figure A-2-9. Effect of linearization of Kelvin term on evolution of number distribution function 3xn(x,t) for continuum growth law for cases 3 and 4, Table A-2-1.

That is, the rate of disappearance of particles is approximately the same for *nonlinear and* linear Kelvin terms. From Equation (A-2-6) it follows that

$$[\psi(x^*,t)\, n(x^*,t)]_{\text{nonlinear}} \cong [\psi(x^*,t)\, n(x^*,t)]_{\text{linear}}. \quad \text{(A-2-16)}$$

Therefore, near to x^*, the LS distribution, Equation (A-2-11), and the asymptotic result, Equation (A-2-12), cannot be correct. However, for t --> ∞, the large differences between $n(x^*,t)_{\text{nonlinear}}$ and $n(x^*,t)_{\text{linear}}$ become confined to a "boundary layer" near x^*, and the asymptotic limits, Equations (A-2-11) and (A-2-12), hold to a good approximation outside of this "boundary layer." This is indicated implicitly by Figures A-2-8 and A-2-9 for the continuum growth law. Cases 5 and 6 represent two very dissimilar initial lognormal distributions studied with the continuum

growth law. As shown in Figure A-2-10, even in D_p,t space, the characteristics of the initial distributions are "forgotten" and a universal form is approached, Equation (A-2-11); although more slowly in case 6, as was discussed above.

The approach to the asymptotic limit distribution, Equation (A-2-12), for kinetic (free molecule) growth, $A(x) \sim x^{2/3}$, is shown for cases 7 and 8 of Table A-2-1 in Figure A-2-11. The differences between the distributions for the nonlinear, Equation (A-2-2), and linearized, Equation (A-2-8), Kelvin term are not evident in this figure. As already noted, those differences for long times appear in a "boundary layer" near x^*, with the value at x^* given approximately by Equation (A-2-16). Figure A-2-12 shows the distribution in D_p,t space for the nonlinear and

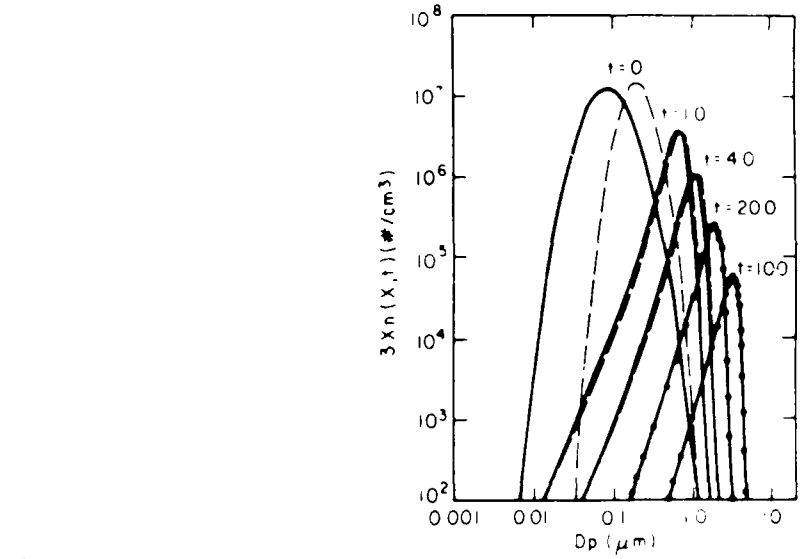

Figure A-2-10. Evolution of number distribution function, $3xn(x,t)$ for continuum growth law for two dissimilar initial particle size distributions, cases 5 and 6, Table A-2-1.

- - - - - - - t=0 (τ=0)
- ·- ·- · - t=0.0075 sec (τ=1.0)
—— - —— t=0.05 sec (τ=1.93)
. . . . . t=300 sec (τ=15.24)
---------- Asymptotic similarity solution, Equation (A-2-12)

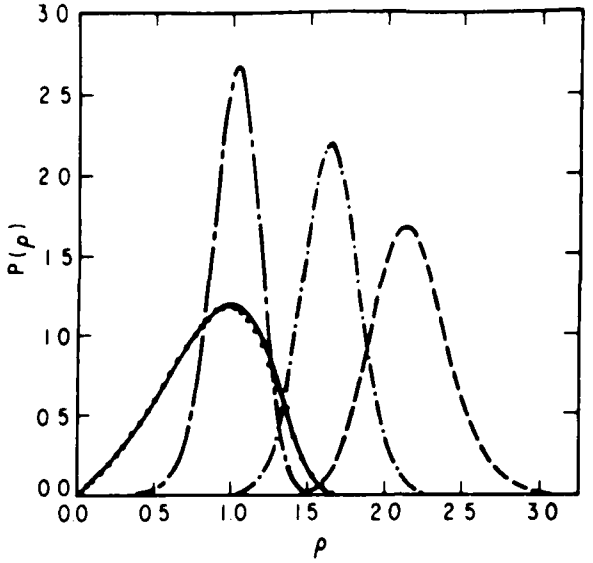

Figure A-2-11. Approach to asymptotic limit distribution for kinetic (free molecule) growth, case 7, Table A-2-1.

linear Kelvin terms for kinetic growth (cases 7 and 8). For small times, there are significant differences in the tails of the distributions for the linear and nonlinear cases.

It is possible to form estimates for the characteristic terms for the evolution of n(x,t) by Equations (A-2-1)-(A-2-5). From examination of the moments, Figures A-2-4 through A-2-8, it is clear that for the initial conditions studied, there are two regimes in the evolution of n(x,t).

In the first, the number concentration, $M_0(t)$, remains constant during the time period necessary for particles to evaporate down to x* and be lost from the distribution. The characteristic time, t_1, for this process can be estimated from the evaporation rate, , Equation (A-2-2). For continuum growth:

$$t_{c1} \sim \frac{(M_1(0)/M_0(0))}{4\pi(3/4\pi d)^{1/3} c_v K}.$$

For kinetic growth:

$$t_{k1} \sim \frac{(M_1(0)/M_0(0))^{2/3}}{3\pi(3/4\pi d)^{2/3}(8\pi T/\pi m_1)^{1/2} C_v K}.$$

From Figures A-2-4 through A-2-8 it can be shown that the time t_2 necessary to achieve the asymptotic state (e.g., Equation (A-2-14)) increases with increasing σ_g of the initial distribution. From dimensional considerations, estimates for t_2 are possible for continuum growth:

$$t_{c2} \sim \frac{(M_2(0)/M_0(0))}{C_v d \bar{D}_p^2 (2\sigma/kT)^2}.$$

..... case 8, linearized Kelvin term, Equation (A-2-8)

——— case 7, nonlinear Kelvin term, Equation (A-2-2)

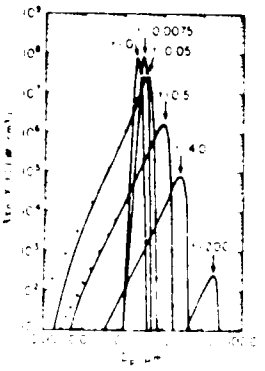

Figure A-2-12. Evolution of number distribution function $3xn(x,t)$ for kinetic growth law for cases 7 and 8, Table A-2-1.

For kinetic growth:

$$t_{k2} \sim \frac{(M_2(0)/M_0(0))}{C_v d(8kT/\pi m_1)^{1/2} D_p^3 (2\pi/kT)^2},$$

where $M_2(0)$ is the initial second moment.

In any event, it is clear that increasing the aerosol vapor pressure over that used in our simulations will lead to a decrease in the time necessary to approach closely the asymptotic regime. Also, a decrease in initial particle dispersion decreases the time necessary to achieve the asymptotic regime.

From our numerical studies of the condensation/evaporation problem with vapor conservation, we conclude the following:

1. Starting with some arbitrary initial distribution, for long times, an asymptotic limit distribution is approached which agrees, for the linearized Kelvin term, with the analytical similarity solutions for continuum and kinetic (free molecule) growth laws. At this asymptotic limit, details of the initial distributions are completely "forgotten."

2. The time evolution, starting with some arbitrary initial distribution, involves two epochs. In the first, the total number concentration remains sensibly constant. In the second, particles begin to be lost from the distribution and the rate of decrease of total particle concentration approaches that predicted by the asymptotic similarity theory.

3. The time necessary to achieve the asymptotic similarity solutions for continuum and kinetic (free molecule) growth laws increases with increasing dispersion in initial particle size distribution.

4. For long times, the differences in the distributions resulting from use of nonlinear and linear Kelvin terms (Equations (A-2-2) and (A-2-8)) in the growth law are confined to a boundary region near x^*, outside of which the distributions are very nearly identical.

5. As is implicit in the similarity theory development, no unique asymptotic limit distribution occurs in the transition region of Knudsen numbers. This is borne out by our numerical simulations using transition region growth laws.

6. For conditions where coagulation may be neglected, it does not appear to be necessary to include competitive effects in describing aerosol growth by condensation/evaporation.

A-3. Aerosol growth: Ostwald ripening and coalescence

Numerous studies[33-47] have been concerned with the asymptotic stages of growth by a homogeneous nucleation process. Comparatively less attention has been given the associated problem of growth when both condensation/evaporation and coalescence occur. For aerosols we have presented the first quantitative study of the Ostwald ripening problem with a realistic coalescence process.

a. Theory.

We have investigated the isothermal spatially homogeneous growth of particles suspended in supersaturated monomer vapora nd inert host gas. The process is described by the evolution equation for the singlet density function n(x,t):

$$\frac{\partial n(x,t)}{\partial t} + \frac{\partial}{\partial x}[\dot{x}(x,s)n(x,t)] = \int_{x^*}^{x/2} b(x-x',x')n(x-x',t)n(x',t)dx' - n(x,t)\int_{x^*} b(x',x)n(x',t)dx' \qquad (A-3-1)$$

where n(x,t)dx is the number of particles having masses in the range x,dx at time, t. $\dot{x}(x,s)$ is the growth law for a particle by the condensation/evaporation process and b(x',x) is the coalescence rate coefficient

for two particles of masses x' and x. x^* is the mass of the smallest particle in the population and s is the supersaturation ratio of monomer vapor. We do not consider here competitive growth effects,[47,48] as the theory for this is lacking when coalescence is significant.

Equation (A-3-1) is coupled to the mass conservation equation for monomer vapor:

$$C_v \frac{ds}{dt} = - \int_{x^*}^{\infty} \psi(x,s)n(x,t)dx - x^*\psi(x^*,s)n(x^*,t) \qquad (A-3-2)$$

where C_v is the equilibrium bulk vapor concentration.

Equations (A-3-1) and (A-3-2) obey the mass conservation law:

$$\frac{d}{dt}(C_v s + M_1) = 0$$

where $M_1 = \int_{x^*}^{\infty} xn(x,t)dx$ is the mass concentration of particles. An important additional moment of n(x,t) is the total number concentration, $N(t) = \int_{x^*}^{\infty} n(x,t)dx$. It follows from Equation (1) that:

$$\frac{dN}{dt} = \psi(x^*,s)n(x^*,t) - \int_{x^*}^{\infty}\int_{x^*}^{\infty} b(x',x)n(x',t)n(x,t)dxdx'$$

We have studied the evolution of n(x,t) by numerical simulation using techniques described in detail elsewhere. These simulations use the continuum diffusive growth laws:

$$\psi(x,s) = 4\pi RDC_v(s - \exp(K/R))$$

where $x = (4\pi/3)R^3d$, D is the binary diffusion coefficient of monomer in host gas and K is the Kelvin coefficient for the dependence of vapor pressure on droplet curvature. d is the mass density of a particle with radius R. The rate coefficient for coalescence is that appropriate to the continuum Brownian process:

$$b(x',x) = (2kT/3\mu)(x^{1/3} + x'^{1/3})\left(\frac{1}{x^{1/3}} + \frac{1}{x'^{1/3}}\right)$$

where kT is the thermal energy and μ is the viscosity coefficient of the host gas.

Equation (A-3-1) may be put into nondimensional form through the substitutions: $\rho = x/\bar{x}_o$, $\tau = 4\pi DC_v(3/4\pi d\bar{x}_o^2)^{1/3}t$, $\phi = \bar{x}_o n(x,t)/N_o$. $\bar{x}_o$ is the initial mean particle mass and N_o the initial number concentration of particles. In these variables, Equation (A-3-1) becomes:

$$\frac{\partial\phi(\rho,\tau)}{\partial\tau} + \frac{\partial}{\partial\rho}[\rho^{1/3}(s - \exp(K'/\rho^{1/3}))\phi(\rho,\tau)] = \tag{A-3-3}$$

$$\alpha\int_{\rho^*}^{\rho/2} b_1(\rho-\rho',\rho')\phi(\rho-\rho',\tau)\phi(\rho',\tau)d\rho' - \phi(\rho,\tau)\int_{\rho^*}^{\infty} b_1(\rho',\rho)\phi(\rho',\tau)d\rho'$$

where

$$\alpha = kTN_o x_o^{2/3}/3\pi\mu DC_v(3/4\pi d)^{1/3}$$

The coefficient α is a measure of the relative rates of coalescence to condensation/evaporation. In Equation (A-3-3), for $\alpha \to \infty$, the coalescence process becomes dominant and for $\alpha \to 0$, only the condensation/evaporation process remains with results previous described.[35,44]

A question addressed by others[40,48] using scaling arguments is which mechanism - condensation/evaporation or coalescence - will be dominant for intermediate values of α. The conclusion from these analyses is that asymptotically coalescence will dominate at higher particle mass concentrations - that is for larger values of α. We show here that this is not the case and that apparently coalescence can only be dominant asymptotically for the growth laws studied for vanishingly small rates of the condensation/evaporation process. This is illustrated by presenting a result from numerical solution of Equations (A-3-1) and (A-3-2) for the stated growth laws. Parameters used yield: α = 0.31, β = $5.3 \times 10^{3}t$, $s(t=0) = 10$, $K/\bar{R}_0 = 1.0$.

Figure A-3-1 shows the evolution in time of the moments N, M_1 of the distribution together with variation with time of the interfacial diameter, D_p^*: $D_p^* = 2K/\ln S$. After an initial induction period[43,44] it

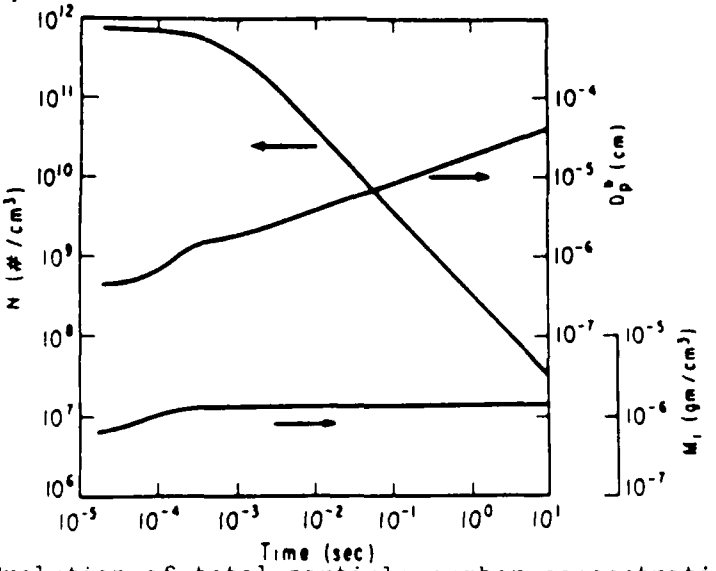

Figure A-3-1. Evolution of total particle number concentration, N, and total particle mass concentration for continuum diffusive growth with simultaneous processes of condensation/evaporation and coalescence. D_p^* is particle diameter at condensation/evaporation interface of particle size distribution.

can be noted that $N(t) \sim t^{-1}$. This dependence is the same predicted for asymptotic continuum diffusive growth by the condensation/evaporation process according to the Lifshitz-Slyozov (LS) theory.[35] It is also the same dependence found both numerically and by similarity theory[49] for the continuum Brownian coalescence process. The increase of D_p^* with time follows the law: $D_p^* \sim t^{1/3}$, also the same predicted by the LS theory for only the condensation/evaporation process. Interestingly, even substantial coalescence rates do not alter significantly this result from condensation/evaporation similarity theory. Since, separately, condensation/evaporation and coalescence both give the result, $N(t) \sim t^{-1}$, for the continuum diffusive cases, scaling arguments are insufficient to establish which of the two mechanisms is dominant asymptotically.

Figure A-3-2 shows the contribution to the total rate of change of N, dN/dt, by each of the two processes - condensation/evaporation and coalescence. The continuous curve is that for the ratio of coalescence rate of change of N to the total rate and the dashed curve that for the condensation/evaporation process according to Equation (A-3-1). Clearly, the contribution of coalescence to the change of N decreases with time while that for condensation/evaporation increases. Therefore previous conjectures on the dominance of either of the two processes appear to be incorrect for these continuum diffusive growth processes.

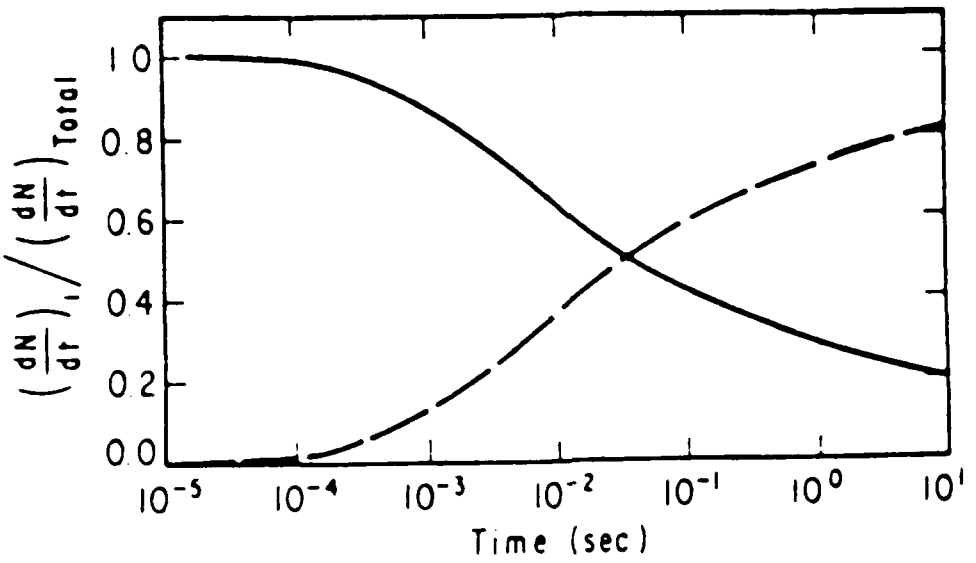

Figure A-3-2. Relative contributions of coalescence (solid curve) and condensation/evaporation (dashed curve) to rate of total time change of particle number concentration, N.

A-4. Aerosol growth: Binary aerosol with one involatile component

The simplest example of a binary aerosol is one in which one of the components making up the particles is involatile. Such aerosols are common and are found in hygroscopic smokes, formation of aerosols by various nucleation processes from vapor mixtures, and in nature in cloud formation processes.

This note reports some results found during development of models of the initial stages of growth of such binary aerosols. The general theory of growth by condensation of ultrafine binary aerosols is discussed first. Next the characteristics of the equilibrium distributions found for these aerosols are presented along with approximate forms for these distributions. Finally unrestricted condensation growth of

these binary aerosols is considered briefly in terms of suitable approximations of the growth process.

a. Theory.

There have been a number of discussions of the growth of binary aerosols (e.g. Friedlander[52], Gelbard and Seinfeld[53]). It is sufficient to note here that the exact description of condensation growth of these aerosols is given by the differential-difference equation:

$$dn_{i,j}/dt = -(\alpha^{(1)}_{i,j} + \alpha^{(2)}_{i,j})\, n_{i,j} + \alpha^{(1)}_{i-1,j} n_{i-1,j} + \alpha^{(2)}_{i,j-1} n_{i,j-1} - (\beta^{(1)}_{i,j} + \beta^{(2)}_{i,j})\, n_{i,j} + \beta^{(1)}_{i+1,j} n_{i+1,j} + \beta^{(2)}_{i,j+1}\, n_{i,j+1}, \qquad (A\text{-}4\text{-}1)$$

where $n_{i,j}$ is the concentration of particles having i molecules of species 1 and j molecules of species 2. Here $\alpha^{(1)}_{i,j}$ and $\alpha^{(2)}_{i,j}$ are the rates of addition of a molecule of species 1 and 2, respectively to a cluster containing i,j molecules. $\beta^{(1)}_{i,j}$ and $\beta^{(2)}_{i,j}$ are the rates of loss by evaporation of a molecule of species 1 and 2, respectively, by a cluster containing i,j molecules.

If it is supposed that species 2 is involatile, then $\beta^{(2)}_{i,j}=0$ by definition. Therefore equation (A-4-1) becomes on dropping the remaining superscript:

$$dn_{i,j}/dt = -(\alpha_{i,j} + \beta_{i,j})n_{i,j} + \alpha_{i-1,j}n_{i-1,j} + \beta_{i+1,j}n_{i+1,j}.$$

In the context of this note equation (A-4-2) provides the description of the condensation growth of the binary aerosol.

ultrafine aerosol phase the coefficients $\beta_{i,j}$, $\alpha_{i,j}$ are evaluated for the free molecule regime of Knudsen number assuming the size of a particle is large compared to that of a condensing molecule:

$$\beta_{i,j} = (8\pi kT/m_1)^{1/2}(3v_1/4\pi)^{2/3}(i+jv_2/v_1)^{2/3}n_1, \qquad (A-4-3)$$

where kT is the thermal energy, and m_1 the molecular mass of species 1; v_1 and v_2 are, respectively, the volume per molecule of species 1 and 2, and for an ideal mixture would be independent of i and j, the numbers of molecules of species 1 and 2 making up a particle. n_1 is the number concentration of species 1 molecules in the vapor at large distances from a cluster.

Similarly, for the evaporation coefficient:

$$\alpha_{i,j} = (8\pi kT/m_1)^{1/2}(3v_1/4\pi)^{2/3}\,(i+jv_2/v_1)^{2/3}n_1^+, \qquad (A-4-4)$$

where n_1^+ is the concentration of species 1 molecules leaving the particle surface. From Defay et al.[51]:

$$\ln(n_1^+/n_1^{+0}) = 2\sigma v_1/kT(3v_1/4\pi)^{1/3}(i+jv_2/v_1)^{1/3} + \ln\gamma_1 - \ln(1+j/i),$$

where σ is the surface tension of a particle of the indicated composition and γ_1 is the activity coefficient of species 1 in the particle phase; n_1^{+0} is the surface concentration for a plane surface given in terms of the vapor pressure of pure species 1. On the assumption of ideality and large particles, it is easy to show that (5) reduces to the familiar form used in cloud physics to derive the so-called Kohler curves (Rogers[55]):

$$= (3\pi T/m_1)^{1/2}(3v_1/4\pi)^{2/3}n_1^{+0}t$$

$$s = n_1/n^{+0}$$

$$\hat{\alpha}_{i,j} = (i+A)^{2/3}s$$

$$\hat{\beta}_{i,j} = (i+A)^{2/3}\exp(\hat{K}/(i+A)^{1/3} + \ln n_1)/(1+j/i) \qquad \text{(A-4-5)}$$

$$\hat{K} = 2(3v_1/4\pi T)^{1/3}(3v_1/4\pi)^{1/3}$$

$$A = jv_2/v_1 .$$

Owing to the lack of a suitable theory of such differential-difference equations and in the interest of computational simplicity, it has for some time (Abraham[50]) been customary to study continuous approximations of equation (A-4-2). Introducing the displacement operator

$$\exp\left(\pm a \frac{\partial}{\partial i}\right) n(i) = n(i \pm a)$$

and regarding i as a continuous variable, (3) becomes:

$$\frac{\partial n(i,j)}{\partial} = -\frac{\partial}{\partial i}(\quad)n(i,j) + \frac{1}{2}\frac{\partial^2}{\partial i^2}(\quad)n(i,j) \qquad \text{(A-4-6)}$$

$$-\frac{1}{6}\frac{\partial^3}{\partial i^3}(\quad)n(i,j) + \frac{1}{24}\frac{\partial^4}{\partial i^4}(\quad)n(i,j) - \ldots$$

The convergence of equation (A-4-6) is usually assumed and it has been customary (Abraham[50]) to truncate the series at the second-order term as a suitable approximation to such differential-difference equations:

$$\frac{\partial n(i,j)}{\partial} = -\frac{\partial}{\partial i}(\quad)n(i,j) + \frac{1}{2}\frac{\partial^2}{\partial i^2}(\quad)n(i,j) . \qquad \text{(A-4-7)}$$

It will be shown below that this truncation is not generally [illegible].

b. Results

The presence of an involatile component makes possible the existence of equilibrium distributions in certain regions of vapor concentration. In addition to their fundamental interest these distributions provide a test of the validity of the expansion, equation (A-4-6).

The equilibrium distributions discussed here are found from the solution of equation (A-4-2) for $dn_{i,j}/dt = 0$. The first-order approximation of equation (A-4-2) is:

$$n(i,j)/\tau = -(i-i^*)n(i,j)/\tau i.$$

The equilibrium solution of this equation for a single value of j is the delta function:

$$n(i,j) = N\delta(i-i^*), \qquad (A-4-8)$$

where i^* is the real root of $i - i^* = 0$ and N is the total number concentration. For variable j and A one has a sum of such delta functions. Equation (A-4-8) of course does not agree with results from equation (A-4-2). There is in reality dispersion in the distribution owing to the discrete nature of the growth process.

In order to include these dispersive effects, one uses equation (A-4-1), which at equilibrium is a steady-state Fokker-Planck equation:

$$\tau^{-1} + \partial n/\partial i^2 - 2(i-i^*)\partial n/\partial i = 0. \qquad (A-4-9)$$

[illegible], the solution of this equation for the binary [illegible] is:

$$n(i,j) = \text{[illegible]}\,(\;\cdot+\cdot\;)^{-1} \exp\left(2 \int^{i} \frac{\cdot-\cdot}{\cdot+\cdot}\, di'\right), \qquad \text{[illegible]}$$

where [illegible] is the normalization factor:

$$\text{[illegible]} = \text{[illegible]}\,(\;\cdot+\cdot\;)^{-1} \exp\left(2 \int^{i} \frac{\cdot-\cdot}{\cdot+\cdot}\, di'\right) di.$$

In the case where the condensing vapor is conserved, the equation for the saturation ratio s and equation (A-4-9) are coupled. In this instance, equation (A-4-10) is only a formal solution as it is now a nonlinear integral equation for n(i,j). There are, however, no new features of the equilibrium distributions introduced by considering vapor conservation and the case of fixed vapor concentration is usually the most important one.

Figure A-4-1 shows a typical example of the reasonable agreement possible between equation (A-4-10) and the exact equilibrium solution of equation (A-4-2). However, this agreement is not universal. As s --> 1 or K --> 0, equation (A-4-10) no longer provides a useful approximation to the exact result from equation (A-4-2). As shown by Figures A-4-2 and A-4-3 where K = 0.1, the distribution given by equation (A-4-9) is no longer acceptable. Even the next level of approximation in the series expansion:

$$\text{[illegible]}$$

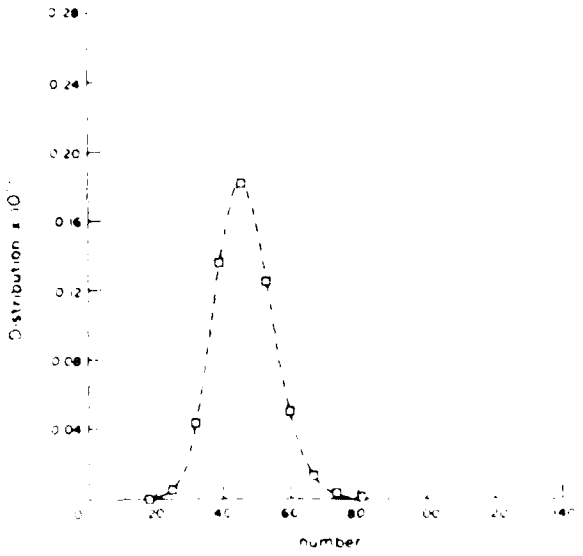

Figure A-4-1. Comparison of equilibrium distributions calculated from: exact difference equation (equation (A-4-2), squares, τ = 0) and from Fokker-Planck approximation (equation (A-4-9), circles, τ =3.0). Parameters: s=0.7; K=5.0; A=200; j=100.

does not improve agreement, as evident from these two examples, Figures A-4-2 and A-4-3. Figure A-4-4, however, shows that for larger K (K=1 in this case) convergence of the series expansion is more rapid and the error in the equilibrium distribution to this level of approximation is reduced. It should be noted that the approximating series cannot be truncated at odd-order terms as these give unstable solutions. In summary, when [illegible] and K small, the series expansion is apparently only slowly convergent and one must use the equilibrium solution of equation (A-4-[illegible]) for an accurate representation of these equilibrium distributions.

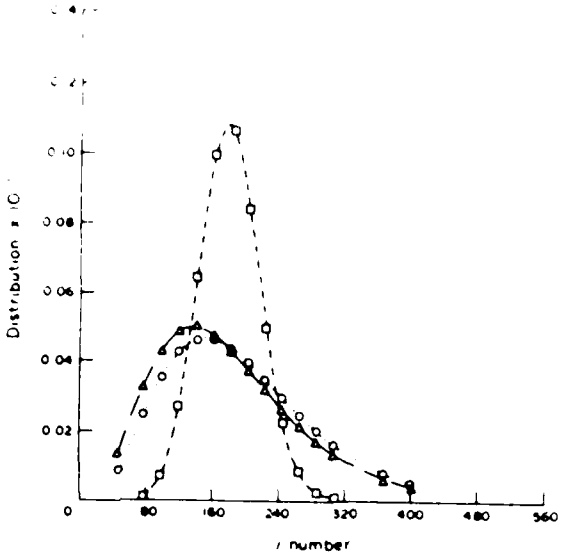

Figure A-4-2. Comparison of equilibrium distributions calculated from: exact difference equation (equation (A-4-2), squares); Fokker-Planck approximation (equation (A-4-9), circles); fourth-order approximation (equation (A-4-12), triangles). Parameters: s=0.99; K=0.1; A=10; j=5.

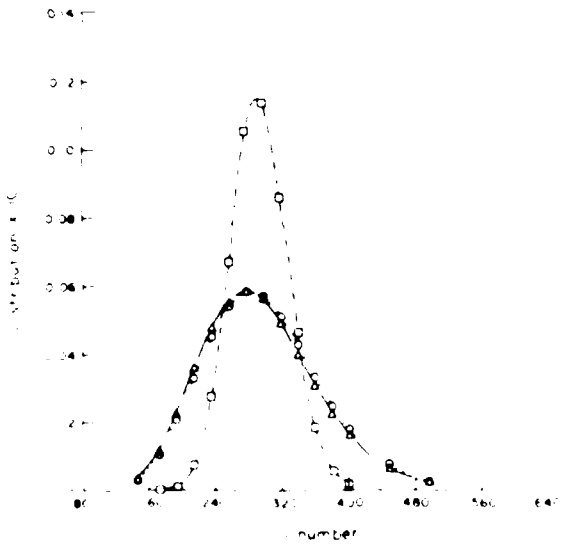

Figure A-4-3. Comparison of equilibrium distributions calculated from: exact difference equation (equation (A-4-2), squares); Fokker-Planck approximation (equation (A-4-9), circles); fourth-order approximation (equation (A-4-12), triangles). Parameters: s=0.99; K=0.1; A=10; j=5.

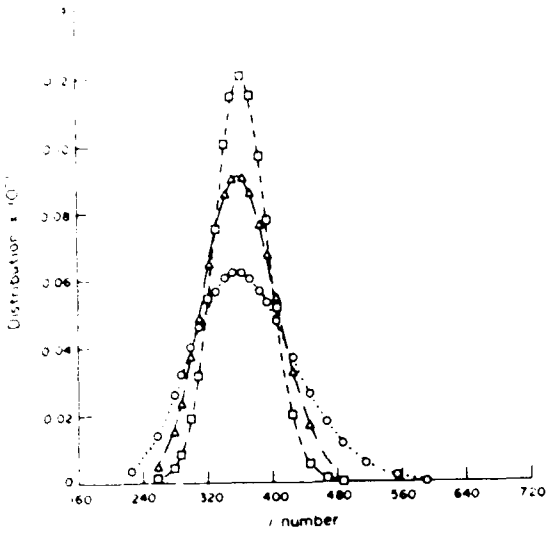

Figure A-4-4. Comparison of equilibrium distributions calculated from: exact difference equation (equation (A-4-2), squares); Fokker-Planck approximation (equation (A-4-9), circles); fourth-order approximation (equation (A-4-12), triangles). Parameters: s=0.9999; K=1.0; A=100; j=50.

For particular values of the parameters in α and β, as s increases above 1, equilibrium distributions are not possible and unrestricted growth of an initial distribution occurs. It is conventional to describe unrestricted growth of an aerosol by condensation with the first-order hyperbolic equation:

$$\partial n/\partial t = -\partial(\ldots)n/\partial i \qquad \text{(A-4-13)}$$

which is, of course, the first term in the expansion of equation (A-4-2) in the present case. Most investigators have neglected the second-order diffusion term and a criterion for this neglect has been discussed by [illegible].

Here the question of neglect of the diffusive term of equation (A-4-7) for modelling unrestricted condensation growth is examined using a lognormal model for the distribution: $n(i) = (N/\sqrt{2\pi}i\ln\sigma)\exp(-\ln^2(i/\bar{i})/2\ln^2\sigma)$ where $\bar{i}$ and σ are, respectively, the geometric mean number and standard deviation. A convenient criterion for this neglect based on the ratio of the derivatives $d^2(\tilde{i}n)/di^2$, $d(\tilde{i}^2n)/di$, evaluated at i would be: $1/\bar{i}(\ln\sigma)^2 \ll 1$, which will be satisfied for i and σ sufficiently large. A more detailed study would need to compare terms in equation (A-4-7) for a particular growth law.

In simulations of particle growth for other aerosol growth models (to be presented elsehwere) it is found that equation (A-4-7) gives an excellent representation of the exact equation (A-4-1) from the nucleation step to growth to large particles. The necessity for discrete-continuous simulations is not therefore always clear. One can argue in favour of including the diffusive term in simulations of aerosol growth under all conditions in which growth may occur at sharp fronts or boundaries of distributions. This would be in the spirit of inclusion of viscosity terms in the hyperbolic conservation equations for numerical treatment of shock propagation (von Neumann and Richtmeyer[56]).

An interesting, if intuitively obvious aspect of unrestricted growth of binary aerosols is the appearance of multimodal distributions from an initially unimodal distribution when the aerosol is an external mixture of a single volatile compojnent and two or more involatile species. An external mixtures means that the particles making

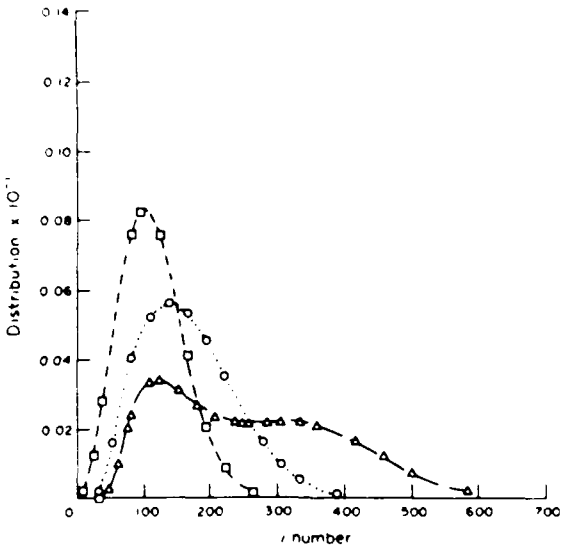

Figure A-4-5. Development of bimodal distribution during condensation growth from initial unimodal distribution of mixture of two aerosols, I and II. Parameters: Aerosol I: s=2; $\bar{K}$=0.1; A=25; j=20. Aerosol II: s=2; $\bar{K}$=0.4; A=25; j=20. In both cases γ_1 taken from data for Hg-Bi mixtures at 320°C.

aerosol contain different masses of the involatile species. Figure A-4-5 shows the development of a bimodal distribution for an initial aerosol consisting of two different involatile species, although all the parameters in α and β are the same except for K: A = 25, j = 20 and γ_1 is taken from experimental data for Hg-Bi mixtures at 320°C. In the simulation, K =0.1 and 0.4. In general for differences in A, K and γ_1 even for the same values of j multimodal functions can arise for long periods of unrestricted growth.

From the results of this study it is concluded that for binary ultrafine particles with one involatile component:

(1) Equilibrium distributions are approximated satisfactorily by the steady-state Fokker-Planck equation, equation (A-4-9), for sufficiently large K and s sufficiently less than 1. In practice, $K > 1$ and $s < 0.9$.

(2) As s approaches 1 and K approaches 0 the series expansion of the difference equation does not provide a useful approximation to the equilibrium distributions.

(3) Neglect of the second-order diffusive term in describing unrestricted growth of binary ultrafine particles is justified only for sufficiently large clusters with relatively broad distributions in the absence of sharp fronts or boundaries in the growth process.

(4) Under restricted condensation growth, initial differences in properties of ultrafine nuclei may lead for some time to the appearance of multimodal distributions from initial unimodal distributions.

A-5. Growth of ferromagnetic particles in gas phase

The production of finely divided particles by evaporation into a background gas dates back to the early 1930's when Pfund[57] made the famous and well-known metallic blacks of a series of metals by evaporating into air at a pressure of 1 Torr. Since that time many studies have been carried out in this process.[58-65] In spite of the large amount of previous work and the frequent use of the evaporation method in experimental procedures, the detailed processes leading to the formation of small primary particles in the gas surrounding a heated sample have not been well understood. Primary particles are defined as the spherical particles observed, either as single isolated particles or as their chain agglomerates.

In work reported here, experimental studies were undertaken to confirm observations of previous investigators on the formation of primary particles and their chain agglomerates when metal samples are heated in inert gas at reduced pressures. These experimental studies are reported first, together with a summary of the observations and discussion of the results. Next, previous theoretical analyses on the formation of primary particles are summarized followed by the development of a new theoretical analysis which explains the present observations as well as those of earlier investigators on the formation of primary particles in evaporation chambers.

a. Experiment.

The formation of primary particles and their chain aggregates was studied experimentally using an evaporation chamber for particle generation and electron microscopy for determination of particle morphology and size distribution. The experimental systems and procedures used in the study are outlined here.

The evaporation chamber is shown schematicallyin Figure A-5-1. The chamber was similar to that used in conventional vacuum evaporation. Here, the chamber was a Pyrex "T" with a diameter of 75 mm and a length of 255 mm for the horizontal portion. Feedthroughs were provided in the base plate for host gas and electrical power and a vacuum line was attached to one of the side plates. The heater for the evaporation source was tungsten wire 25 mm in length and 0.5 mm in diameter. The

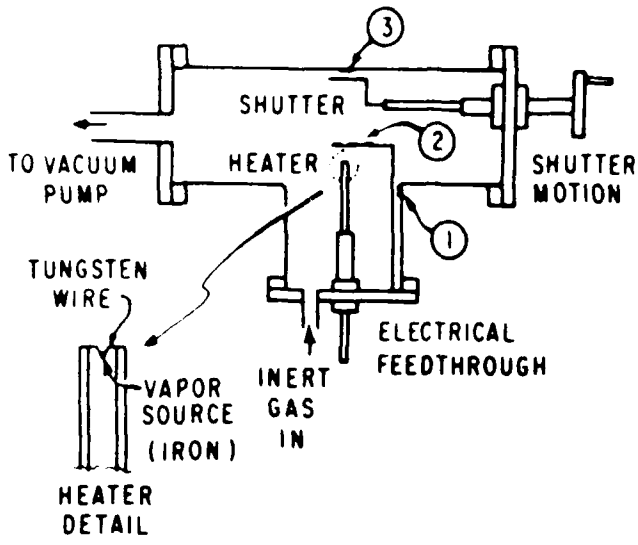

Figure A-5-1. Schematic diagram of experimental metal evaporation chamber. Points 1, 2, and 3 are particle sampling positions.

wire was bent to form a "V" in its center where the metal sample was placed. This sample typically had a mass of 2-3 mg. Usually, the chamber was evacuated down to 1E - 5 Torr initially, then filled with host gas to 300 Torr, reevacuated, and then refilled with host gas to the desired pressure. The heating current was applied for about ten seconds to evaporate the metal sample. The pressure inside the chamber was measured with ionization and thermocouple gauges. The temperature of the evaporation source was determined with an optical pyrometer. Particles resulting from evaporation of the metal sample were collected on carbon-coated transmission electron microscope grids at various positions in the chamber relative to the source. A shutter was used to control the amount of deposit on a grid. The entire region could be subjected to magnetic fields up to 1200 G. Grids with deposited particles were stored in nonoxidizing conditions and observed using a transmission electron microscope (JEOL JEM-200 CX) as well as a scanning electron microscope

(JEOL JSM-35C). For determination of primary particle size distributions, a semiautomated procedure developed by Hazlett et al.[66] was used. In this determination, images on negatives from electron micrographs of particle samples were digitized with a video camera. Analysis proceeded with edge enhancement and edge detection algorithms which ask for visual user confirmation of particle contour and acceptance of particle size.

b. Results.

The following qualitative observations correspond to those of previous workers. Upon heating of the source, a well-defined spherical smoke shell was observed to form concentrically with the source. Particulate samples were readily obtained when the specimen grids were placed on or near this smoke shell. When a grid was placed inside the smoke shell, the deposits resembled those seen in thin-film micrographs. This strongly implies that particles are not formed in the gas phase inside the smoke shell and that nucleation and particle growth occur directly on the grids in this region. As the host-gas pressure was lowered below 1 Torr, the visual smoke shell disappeared. At host-gas pressure below 0.01 Torr, it was inferred that no particles were formed in the gas phase as the deposits on the grids had the characteristic appearance of thin-film deposits. At higher pressures in the vicinity of the smoke shell, the particles formed were more or less linear chains even in the absence of an external magnetic field; inside the smoke

shell, particle chains were rarely observed. In and exterior to the smoke shell, application of an external magnetic field produced linear chains. However, it was found that small scale linearity of the chains was not greatly improved even at 1200 G.

The size of the primary particles making up the linear particle chains depended upon the host-gas pressure, the nature of the host gas, and the source temperature. The mean size of the primary particles increased with host-gas molecular weight. Mean primary particle size increased as the host gas was changed from helium to argon to xenon. Primary particle size also increased as the temperature was increased above 1800°C. Below approximately 1800°C very few particles could be observed on the grids. The primary particles have quite narrow size distributions. Figure A-5-2 shows primary particle size distributions for some representative chains. The three distributions represent particles produced in the chamber at pressures of 2, 6, and 20 Torr and a temperature of 1950°C (in order of increasing mean particle diameter).

c. Theory.

There have been a number of previous studies on the formation of particles in evaporation chambers. The previous theoretical analyses have not been successful in explaining all of the qualitative observations cited above. For example, Kawamura[67] posed a simple model in which the vapor supersaturation in the evaporation chamber determined the size of the metallic fine particles. This model explained the dependence of

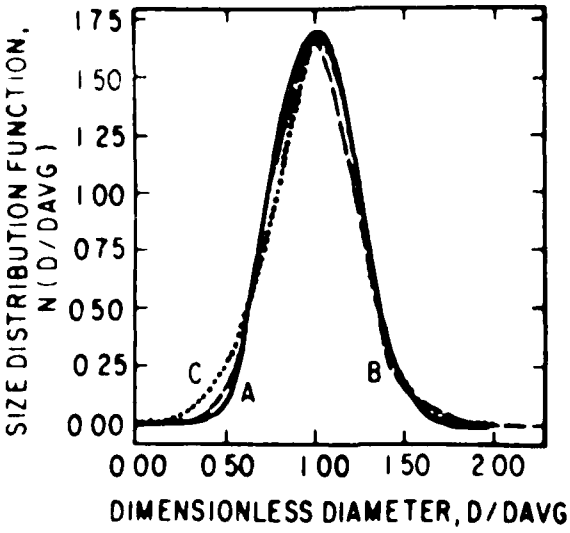

Figure A-5-2. Experimental size distributions of primary particles formed in evaporation chamber. D is particle diameter, DAVG is the number mean diameter. Curve A (line): DAVG=124 Å, standard deviation=0.22, host-gas pressure=20 Torr; Curve B (dash); DAVG=94 Å, standard deviation=0.25, host-gas pressure=6 Torr Curve C (dot): DAVG=6 Å, standard deviation=0.265, host-gas pressure=2 Torr.

primary particle size on the chamber pressure, but failed to explain its dependence on source temperature. The model also did not contain a description of particle formation and growth. Ozawa[68] obtained particle size distributions by solving the growth equations for the primary particles using steady-state solutions for the spatial distributions of temperature and vapor concentration. This model predicted that primary particle formation occurred in a narrow region close to the cooled wall of the chamber, a finding contradicted by experimental observations. In addition, the particle growth equations were not coupled to the energy and vapor conservation equations and did not include any particle transport mechanisms. Yatsuya et al.[62] observed a convective flow around their source, a heated tungsten boat, and concluded that the smoke shell

observed occurred in a region where the upward convective flow [illegible] tively cool host gas met a radial flow [illegible] metallic vapor [illegible] out from the source. However, when the tungsten boat was replaced tungsten wire as heater, no convective flow was observed although the smoke shell was still present. Nolan[64] claimed from similar [illegible] that primary particles grow mostly by coalescence in the smoke [illegible] conclusion based not on simulation of particle dynamics, but on a comparison of residence time in the smoke shell with characteristic coalescence times. Similar conclusions were reached by Granqvist et al.,[69] again in the absence of simulation of particle dynamics.

In this section, a model is developed for the formation of primary particles in evaporation chambers which contains all of the relevant dynamical processes of particle formation, growth, and transport. The physical system to be modeled consists of a spherical chamber of radius r_0 filled with inert host gas at some pressure P. A spherical source is located at the center of the chamber with radius r_s and is maintained at temperature T_s while the chamber walls are kept at temperature T_0. At the surface of the spherical source, the partial pressure of the metal vapor is assumed to be the equilibrium vapor pressure of the metal at temperature T_s. The contribution of the metal vapor to the chamber pressure is assumed to be negligible. From the source, both heat and metal vapor diffuse radially outward. The gradients of temperature and vapor result in spatial gradients of the saturation which give rise to homogeneous nucleation and growth of primary particles whose rates vary with distance from the source.

gradients of particles and temperature give rise to radial particle fluxes due to Brownian diffusion and thermophoresis. Based on observations and simulation results to be presented, the formation of particle chains only occurs at larger radial distances after the growth of the primary particles is completed.

The particle formation, growth, and transport processes outlined are described by the following evolution equation for the primary particle size distribution function $n(x,r,t)$, where $n(x,r,t)dx$ is the number of particles having masses in the range x,dx at radial position r at time t:

$$\frac{\partial n(x,r,t)}{\partial t} = \left(\frac{1}{r^2}\right)\frac{\partial (r^2 N)}{\partial r} + 0.5\int_{x^*}^{x} b(x,x')n(x-x',r,t)n(x',r,t)dx' - n(x,r,t)\int_{x^*}^{\infty} b(x',x)n(x',r,t)dx' - \frac{\partial [v(x,c_v,t)n(x,r,t)]}{\partial x} + R. \qquad \text{(A-5-1)}$$

Here N is the total diffusional flux of particles. The second and third terms on the right-hand side account for particle coalescence and the fourth term for growth by condensation of vapor. R is the rate of production of particles by homogeneous nucleation. For all experimental runs, the particle Knudsen number Kn is such that Kn>>10. Consequently, all particle growth and transport processes are described by free molecular theory.[70] The diffusional flux of particles is given by the expression

$$N = -D_p \frac{\partial n}{\partial r} - C_t n, \qquad \text{(A-5-2)}$$

where β_p is the free molecular Brownian diffusion coefficient and β_t is the free molecular thermophoretic velocity.[71] Similarly in Equation (A-5-1), the coalescence coefficient $\beta(x,x')$ and the condensation/evaporation coefficient γ are given by the free molecular expressions.[70] The homogeneous nucleation rate R is assumed to be given by the expression

$$R = R^* [x - x^*(r,t)], \qquad (A-5-2)$$

where δ is the delta function, x^* is the critical nucleus size, and R^* is the rate of appearance of critical nuclei given by the classical theory of Volmer-Becker-Doring-Zeldovich.[70] Equation (A-5-1) is coupled to the conservation equation for metallic vapor, which has the form

$$\frac{\partial c_v(r,t)}{\partial t} = -\left(\frac{1}{r^2}\right)\frac{\partial (r^2 N_v)}{\partial r} - \int_{x^*}^{\infty} \beta(x,c_v,t)\, n(x,r,t)\, dx - \int_{x^*}^{\infty} \gamma(x,c_v,t)\, n(x,r,t)\, dx. \qquad (A-5-4)$$

The vapor diffusion flux is

$$N_v = -D_v \frac{\partial c_v}{\partial r} - \frac{c_g M_g M_v k_T}{\rho_g T}\frac{\partial T}{\partial r}, \qquad (A-5-5)$$

where D_v is the diffusion coefficient for vapor, c_g the molar concentration of the host gas, ρ_g and M_g the density and molecular weight of the host gas, M_v the molecular weight of vapor, and k_T the thermal diffusion ratio of vapor in the host gas. In all calculations the temperature dependence of the transport coefficients is accounted for.[71]

Finally, the energy equation is coupled to Equations (A-5-1) and (A-5-4). It has the form

$$\frac{\partial n_{r,t}}{\partial t} = -\frac{1}{r^2}\frac{\partial [r^2(q+\dot{H}N_v)]}{\partial r} + \alpha_{pg}\dot{A}_g(T - T_p)A_p, \quad (A\text{-}5\text{-}5)$$

where c_{pg} is the heat capacity of the host gas at constant pressure, q the thermal heat flux, H the specific enthalpy of the vapor, α the thermal accommodation coefficient of the host gas with the particle surface, A_p the surface area of particles, T_p the mean temperature of particles, and $\dot{A}_g$ the mass rate of the host gas with unit area of particle surface. Radiative heating of the host gas was ignored since absorptivity of the gas and vapor is negligible. In a thermal radiation field the local mean temperature of the particles may be different from that of the host gas. A radiation energy balance is used to obtain T_p:

$$A_s \sigma_p T_s^4 A_{pp}/4\pi r_{12}^2 = \sigma_p T_p^4 A_p + \alpha_{pg}\dot{A}_g(T_p - T)A_p, \quad (A\text{-}5\text{-}7)$$

where σ is the Stefan-Boltzmann constant, e_p the emissivity of the particles, A_s the surface area of the vapor source, and A_p the mean projected area of particle surface exposed to radiation from the source at distance r_{12}.

A complete description of the evolution of the primary particles in the evaporation chamber would require simultaneous solution of equations (A-5-1) - (A-5-6). However, the experimental data do not warrant such a complete analysis, where only qualitative verification of experimental results is necessary. In this case, only the first three moments of $n(x,r,t)$ are sufficient. Consequently, a moment method is used to

obtain a partial solution of Equations A-5-1 - A-5-3. The kth moment of n(x,r,t) is given by

$$M_k(r,t) = \int_{x^*} x^k n(x,r,t)\,dx, \qquad (A\text{-}5\text{-}4)$$

where k is an arbitrary real number, M_0 is the total number concentration of particles, M_1 the mass concentration of particles, and M_2 the second moment related to the variance. It is clear from Equation A-5-3 that a straightforward application of the moment method to Equation A-5-1 will not result in a closed set of equations for these three moments since fractional moments arise from the various particle dynamical coefficients which involve fractional powers of the particle mass. More rigorous solutions of this problem are possible; however, here it is sufficient to employ a very approximate theory since only the qualitative features of the present and previous experimental results are sought. In addition, the simulations presented here are for times less than the order of 10 ms so that particles do not grow larger than approximately 2-nm diameter. In this case, the particle dynamical coefficients are taken to be constants and the average particle diameter can be expressed in terms of the three moments with the assumption of a lognormal particle size distribution for n(x,t):

$$n(x,t) = M_0 \left(\frac{1}{2\pi}\right)^{1/2} (1/x\ln\sigma) \exp\left[-(\ln x - \ln x_{av})^2/2\ln^2\sigma\right], \qquad (A\text{-}5\text{-}5)$$

where x_{av} is the geometric mean particle mass and σ is the standard deviation. From Equations (A-5-3) and (A-5-4) it can be shown the moments M_1 and M_2 are given in terms of x_{av} and σ by

$$M_1 = M_0 x_{av} \exp(9 \ln^2 \sigma/2), \qquad \text{(A-5-10)}$$

$$M_2 = M_0 x_{av}^2 \exp(18 \ln^2 \sigma). \qquad \text{(A-5-11)}$$

x_{av} and σ can be eliminated from Equations (A-5-10) and (A-5-11) to obtain the geometric mean particle diameter d_p:

$$d_p = (6M_0^{-3/2} M_1 M_2^{-1/2}/\pi\rho)^{1/3}. \qquad \text{(A-5-12)}$$

Particle diameters are calculated only in the region of the smoke shell since the numerical error in the calculation will be small there. At other positions the particle concentrations are found to be very low and the numerical error due to the very stiff nature of this problem is large.

d. Discussion.

The moment equations for M_0, M_1, and M_2, the mass conservation equation, and the coupling equation between local mean particle temperature and host-gas temperature are solved numerically. Spatial distributions of vapor concentration, temperature, supersaturation, and particle moments are reported as a function of the logarithm of the dimensionless distance from the source, $\ln(r/r_s)/\ln(r_0/r_s)$.

As shown in Figure A-5-3, the distribution of [illegible] has a maximum between the source and chamber walls. [illegible] the supersaturation value at the maximum point [illegible] temperature, but is relatively insensitive [illegible]

AD-A184 467 PLUME MECHANICS AND AEROSOL GROWTH PROCESSES(U) TEXAS UNIV AT AUSTIN AEROSOL RESEARCH LAB J R BROCK JUL 87 CRDEC-CR-87084 DAAK11-83-K-0006 2/3

UNCLASSIFIED F/G 19/1 NL

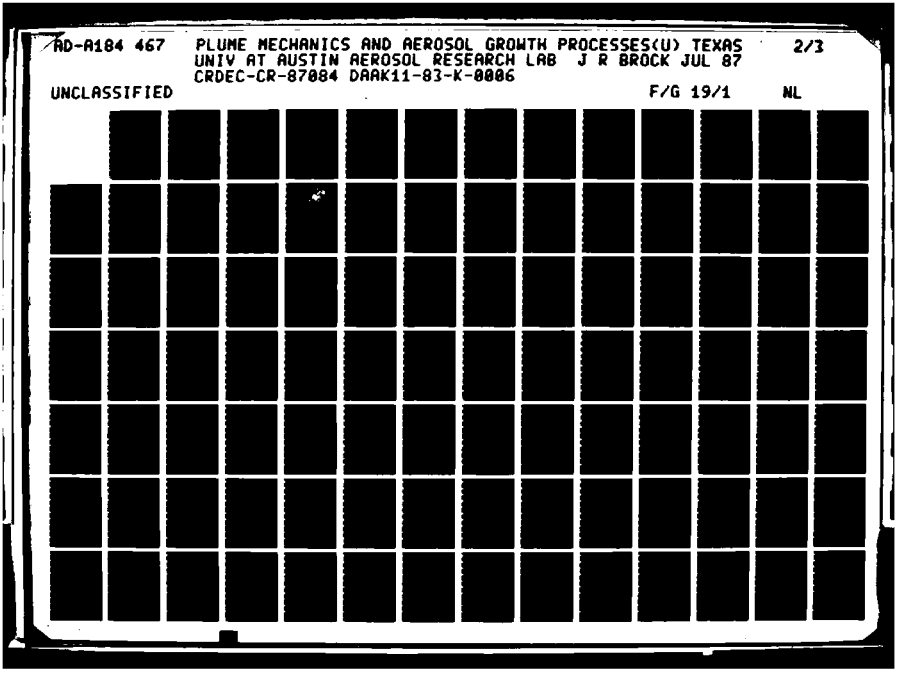

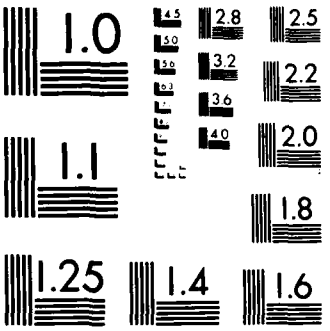

MICROCOPY RESOLUTION TEST CHART
NATIONAL BUREAU OF STANDARDS-1963-A

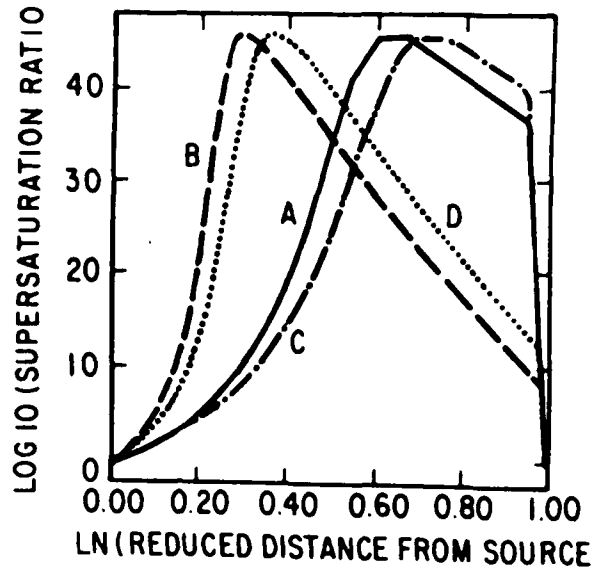

Figure A-5-3. Distribution of supersaturation ratio in model evaporation chamber with time and host-gas pressure as parameter. T_s=2000 K, nitrogen host gas. Curve A: P=500 dyn/cm^2, t=0.05 ms; Curve B: P=10000 dyn/cm^2, t=0.05 ms; Curve C: P=500 dyn/cm^2, t=0.1 ms; Curve D: P=10000 dyn/cm^2, t=0.1 ms.

properties. It is in this supersaturation maximum that particle formation and growth is dominant. As a consequence of this maximum point, the particle concentration is vanishingly small everywhere but in a narrow spatial region, termed above the so-called "smoke shell." Figure A-5-4 shows that the vapor concentration curves exhibit a cross-over as the host-gas pressure is changed. As host-gas pressure is increased, with reference to Figure A-5-3 the supersaturation maximum moves toward the source and, as shown in Figure A-5-5, the smoke shell becomes thinner. The other particle moments display similar trends to that indicated for the particle number concentration in Figure A-5-5.

The supersaturation ratio and particle moments are very sensitive to the source temperature, as would be expected from the exponential dependence of metal vapor pressure on temperature and the

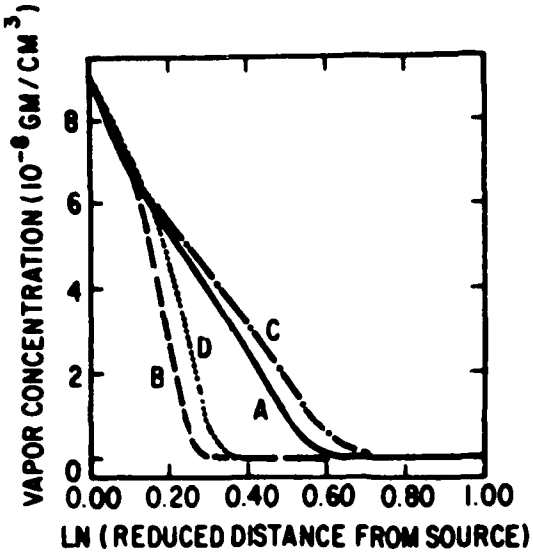

Figure A-5-4. Distribution of supersaturation metal vapor concentration in model evaporation chamber. Crossover effect with variation of host gas pressure is shown. T_s=2000 K, nitrogen host gas. Curve A: P=500 dyn/cm^2, t=0.05 ms; Curve B: P=10000 dyn/cm^2, t=0.05 ms; Curve C: P=500 dyn/cm^2, t=0.1 ms; Curve D: P=10000 dyn/cm^2, t=0.1 ms.

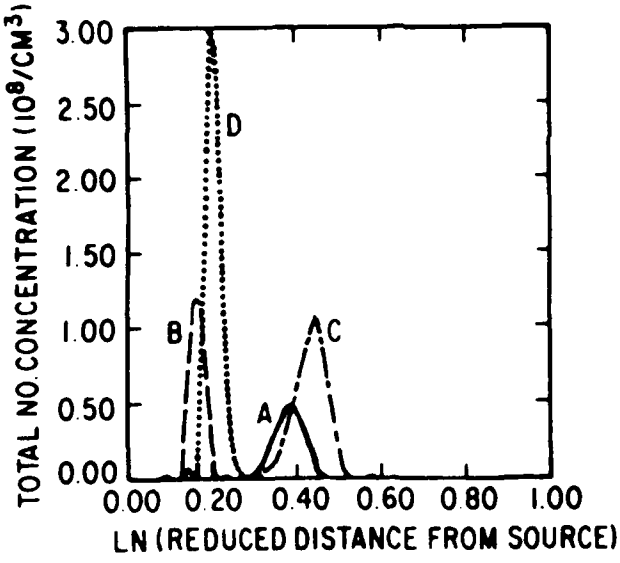

Figure A-5-5. Distribution of total number concentration of primary particles in model evaporation chamber with pressure and time as parameters. Narrow concentration distributions correspond to experimentally observed "smoke shell" surrounding the vapor source. T_s=2000 K, nitrogen host gas. Curve A: P=500 dyn/cm^2, t=0.05 ms; Curve B: P=10000 dyn/cm^2, t=0.05 ms; Curve C: P=500 dyn/cm^2, t=0.1 ms; Curve D: P=10000 dyn/cm^2, t=0.1 ms.

large variation of particle nucleation rate with supersaturation ratio. At lower source temperatures supersaturation ratios are not large enough to produce high concentrations of particles and a smoke shell about the source will not be observed. However, as shown by Figure A-5-6, if sufficiently high particle concentrations exist so that the smoke shell could be observed at all, the width of the smoke shell will not vary with source temperature; this phenomenon has been observed experimentally by Yatsuya et al.,[62], but not explained before now.

Mean particle diameters have been calculated from the particle moments only in the region of high particle concentration, the smoke shell. The calculations show that increases of host-gas pressure, source temperature, or molecular weight of the host gas results in increases of the mean particle diameter. This is illustrated for increasing host gas pressure in Figure A-5-7. These trends have been observed experimentally here as well as by previous investigators, but up to now have not been satisfactorily explained.

The published literature on gas evaporation systems[58-64] has emphasized the role of merging convective flow of host gas and diffusional flow of the evaporating vapor in explaining the formation of the so-called "smoke shell." The present numerical model shows clearly that these previous explanations are not correct and that thermophoresis of the particles is responsible for formation of the smoke shell; this is illustrated by Figure A-5-9 where the spatial distribution of par[illegible]

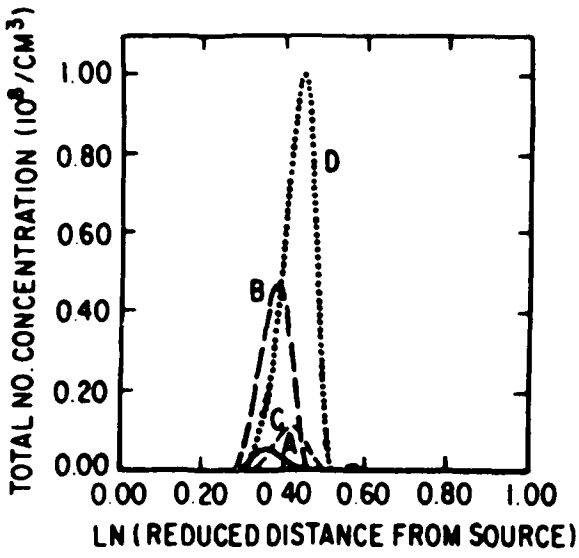

Figure A-5-6. Distribution of total number concentration of primary particles in model evaporation chamber with source temperature and time as parameters. Width of "smoke shell" does not vary with source temperature. P = 500 dyn/cm^2, nitrogen host gas. Curve A: T_s=2000 K, t=0.05 ms; Curve B: T_s=1900 K, t=0.05 ms; Curve C: T_s=2000 K, t=0.1 ms; Curve D: T_s=1900 K, t=0.1 ms.

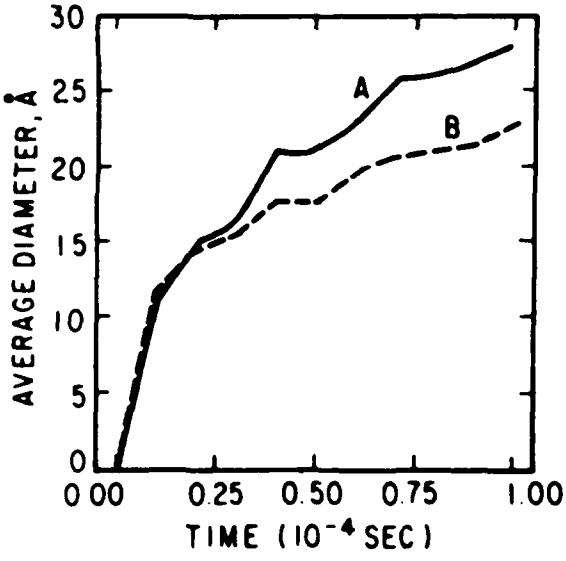

Figure A-5-7. The effect of host-gas pressure on average diameter of primary particles. Curve A: P=10000 dyn/cm^2; Curve B: P=500 dyn/cm^2.

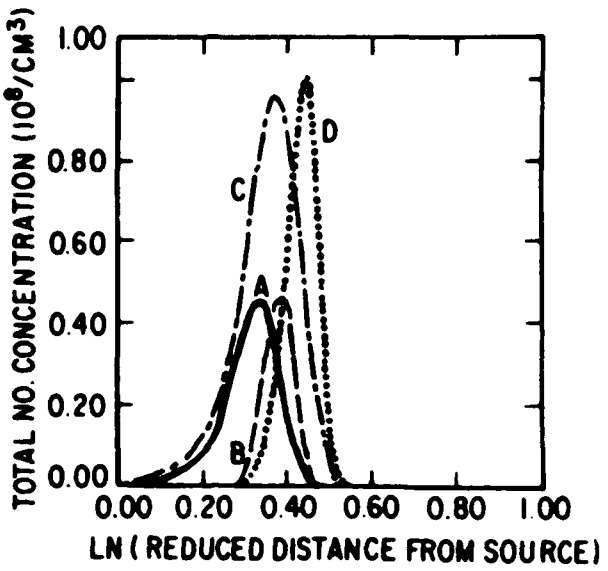

Figure A-5-8. Distribution of total number concentration of primary particles in model evaporation chamber with and without particle thermophoresis. Illustration of the principal role of particle thermophoresis in forming the "smoke shell." P = 500 dyn/cm^2, T = 200 K; Nitrogen host gas. Curve A: Without thermophoresis, t=0.05 ms; Curve B: With thermophoresis, t=0.05 ms; Curve C: Without thermophoresis, t=0.1 ms; Curve D: With thermophoresis, t=0.1 ms.

concentration is shown with and without particle thermophoresis. In the absence of thermophoresis, particles have a broad spatial distribution and the particle free zone around the source observed experimentally is not found.

Over the time scale represented by the position of the smoke shell (up to approximately 0.1 ms) coalescence of clusters to produce primary particles is not important, as verified by calculations with and without the coalescence process. Primary particle growth clearly occurs by condensation of metal vapor atoms; condensation growth is well known to produce narrow particle size distributions. Experimentally, it is always observed that the size distributions of primary particles in

evaporation chambers are narrow and that the primary particles are spherical. For longer times, as particles move further away from the source, coagulation (not coalescence) becomes important as evidenced by the formation of particle chains.

The present model explains present and previous experimental observations on primary particle formation in metal evaporation systems. The dependence of primary particle size on host-gas pressure, host-gas molecular weight and source temperature has been explained. Particle thermophoresis has been shown to cause the formation of the so-called "smoke shell" observed surrounding the source. Particle coalescence nas been shown not to be an important growth process for the primary particles. Particle coagulation, of course, for longer times is an important growth process in the formation of the chains of primary particles observed experimentally. Particle chain formation and its dependence on the system parameters will be the subject of an additional study.

A-6. Growth of ferromagnetic particles in liquid phase

The addition of a reducing agent to a solution containing metal cations produces metal atoms which condense to form particles. The reaction between metallic salts and sodium borohydride in the liquid phase to produce ultrafine metallic particles has been known since the work of Schlesinger et al.[1] These investigators demonstrated that sodium borohydride reacted rapidly with certain first-row transition

metal salts in aqueous phase to yield finely divided black precipitates thought to be metal borides. It is now known that through variation of ionic concentrations, temperature, and reducing agent ultrafine particles of a given mean primary particle size can be produced. The simplicity and rapidity of the borohydride reduction reaction have led to its widespread use in many applications, such as electroless plating, preparation of catalysts, and production of magnetic recording media.

Most studies on application of borohydride reduction in catalyst preparation have been directed toward procedures for preparation of very highly dispersed material.[73-76] Research on use of metallic cation reduction for preparation of magnetic recording coatings has been focused mainly on the magnetic properties and oxidation resistance of the particles produced.[77-80] However, in previous research the dependence of particle properties on the various experimental parameters, such as cation and anion nature and concentration, solvent, stabilizers, additives, and temperature have not been investigated systematically.

Work described here was designed to develop fundamental information on particle formation and growth in the reduction of metallic cations by borohydride. Of particular interest were the growth mechanisms of the primary particles, the effect of the experimental parameters noted above on the properties of the primary particles, and the role of primary particle properties on subsequent growth of the aggregates. First, the experimental procedures used in this investigation are described. This is followed by a summary and analysis of

experimental results. Finally, a theoretical model is developed and used to interpret qualitatively these results.

a. Experiment.

The reaction between the borohydride ion and metallic anions is initially rapid. Therefore, in order to obtain reproducible results independent of the fluid dynamical state, a mixing junction was designed similar to that used for stopped-flow reactors for the study of fact reactions.[81] This junction was in the form of a "tee" formed from brass tubing with an inside diameter of 1 mm. Mixing of the two reactant streams could be effected on time scales down to a few microseconds. The flow from the mixing junction was directed to an agitated ultrasonic bath where the slower final phase of particle growth took place. External magnetic fields could be applied bot to the "tee" reactor and to the ultrasonic bath. The particle suspension in the bath was washed with deionized water to remove the soluble reaction by-products and the solid particles were then finally dispersed in acetone; all these steps were carried out in the absence of oxygen. This method of particle formation was the principal one used in these studies. However, an alternative method for bringing about reaction with rapid mixing was also employed. In this method, reactants were aerosolized in two separate nebulizers. The aerosol jets from these nebulizers were directed towards each other. As a result, droplet collision and coalescence occurred so that the reduction reaction was confined to the individual droplets. This

droplets were of the order of 1 μm in diameter so that the diffusional time scale was less than the order of 1 msec.

Particles produced in the "tee" reactor system were studied by a number of techniques including transmission electron microscopy (TEM). The first step here was to sample the particles collected from the reactor as a dispersion in acetone. The most obvious method was to place a drop of the acetone dispersion onto a grid; however, as the acetone evaporates the particles in the droplet tend to agglomerate on the grid and this makes it difficult to obtain satisfactory micrographs for analysis. Another method involved placing a drop of the acetone dispersion onto a glass microscope slide, spreading the drop over the slide by shearing and then sampling the sheared deposit; however, it was found that the shearing action tended to break the original chains formed in the reaction system. The most successful method, and the one used, involved nebulizing the acetone dispersion as approximately 10 m droplets which were then collected on the TEM grids by direct impaction; this method was found to minimize alteration of particle characteristics noted with the other methods and could be applied successfully to any concentration of the acetone dispersion. Grids with deposited particles were stored in nonoxidizing conditions and observed using a JEOL JEM-200CX transmission electron microscope.

In addition to the study by TEM, the saturation magnetiziation (SM) of the particles was also measured. In preparation for the SM determination, the acetone dispersion was dried under a nitrogen atmosphere at room temperature, although in some experiments drying was

carried out at elevated temperatures to investigate the effects of thermal annealing on SM. In this manner, particle samples of approximately 0.02 and 0.05 grams were placed in a sample holder and used in measurement of SM in a vibrating sample mangetometer (Model FM-1 Princeton Applied Research). This instrument was initially calibrated with a standard nickel sample. Reproducibility of SM data with these techniques was very good. A portion of the sample used for the SM determination was at the same time used to get information on chemical composition of the particles. The bulk and surface chemical compositions were determined by Inductively Coupled Plasma Atomic Emission Spectroscopy (ICP-AES) and X-ray Photoelectron Spectroscopy (XPS).

The reactants were all reagent grade chemicals and were used in the experiments without additional purification. Solutions of ferrous chloride, ferrous sulfate, cobaltous chloride, and nickelous chloride were used as the sources of the metallic cations. The reducing agent was sodium borohydride; the standard reducing solution used in the experiments was 0.1 M to which was added 0.1 wt% sodium hydroxide to maintain a basic solution and prevent hydrolysis of the sodium borohydride. In the experiments, cation and anion concentrations were varied. In order to study the effects of additives, chromium chloride was used as an anti-oxidant and gelatin and sodium citrate were used as stabilizers. Neodymium chloride was also used in separate studies of supermagnetic materials. In most experiments, deionized water was the solvent; however, some runs were carried out in which mixtures of deionized water and reagent grade ethyl alcohol were the solvents.

As noted above, two methods were used for carrying out the borohydride reduction reaction to produce particles. One of these involved nebulization of the reactants in opposed jets so as to bring about subsequent collision and coalescence of the reactant droplets. This mode of reaction produced very small primary particles (approximately 50 A in diameter) which were confined on the TEM grids to the areas of the evaporated acetone droplets which were around 0.2 to 0.5 μm in diameter. The second method used the "tee" reactor system. With this system, the primary particle sizes varied from approximately 100 to 1500 A in diameter, depending on the experimental conditions. In most of the experimental runs using the "tee" reactor system, the primary particles formed essentially linear chains with some branches. External magnetic fields were necessary to produce straight chains without branching. The primary particles in a given chain were found to have narrow size distributions.

Table A-6-1 shows the bulk weight percent of the elements in particles produced by the "tee" reactor system as determined gy ICP-AES analysis; for this analysis all the samples were obtained from the "standard" reducing solution and 0.1 M metallic cation solutions. The alloy samples were prepared from equimolar mixtures of the cations and used the "standard" borohydride solution with 0.1 M metallic cation solutions. Nitric acid was used as solvent for the particle sample for ICP-AES analysis; the ratio of the mass from the analysis to the total mass of the original sample shows that some minor components of the

Table A-6-1: Bulk Composition of Particles

Sample Number	Sample I.D.	Na	Fe	Co	Ni	B	Total	Metal/B
				wt.%			%	(Atomic)
I	$(Fe,Co)_2B$	<0.02	34.71	53.59	0.11	9.37	97.78	1.82
II	Co_2B	<0.03	0.02	83.16	0.18	8.84	92.20	1.72
III	Ni_2B	<0.02	0.04	<0.01	73.65	8.14	81.83	1.66
IV	$(Fe,Ni)_2B$	<0.02	32.35	<0.01	53.04	9.03	94.42	1.83
V	Fe_2B	<0.02	89.09	<0.01	0.02*	7.96	97.07	2.16

* Close to the detection limit

particles were insoluble. Atomic ratios of metal to boron are approximately 2 for all samples. It can also be seen that in the alloy samples, the cobalt or nickel content is always higher than that of iron even though the reactant cation concentrations were equimolar. Analysis of the samples by XPS for surface composition showed that the ratio of metal to boron on the surface was one or smaller. This indicates that the boron was deposited mainly on the surface of the metal particles and that the particles are probably not metal borides but are an admixture of boron and metal. In the absence of thermal treatment, all the particles except those prepared at very low metallic cation concentration did not show any crystalline diffraction pattern with TEM. All the dried particles were pyrophoric in air. Also all the particles were ferromagnetic except particles formed from nickel cations; these particles became

ferromagnetic when heated for 20 min. in nitrogen at around 100°C.

In all of the studies of the production of particles by borohydride reduction, it was found that variation of the anions (sulfate and chloride) associated with the metallic cations did not affect the particle characteristics. However, variation of the cations (ferrous, cobaltous and nickelous) led to large changes in primary particle size, chain forming ability of the primary particles, and saturation magnetization of the particles. In the study of the effect of variation of the metallic cation, various amounts of cobaltous chloride or nickelous chloride were added to ferrous chloride while maintaining the same molar concentration of total metallic cation (0.1 M). As shown in Figure A-6-1, significant changes occur in the mean primary particle diameter as the compositions are varied. Chain length was found to diminish gradually with increasing content of cobaltous or nickelous ion. Particles formed from mixtures of cobaltous and nickelous ions in the absence of iron did not form chains even with magnetic fields up to 1200 Gauss. For particles formed from single component metallic ion solutions, the saturation magnetization (SM) values decreased in the sequence Fe (130 emu/g) > Co (30 emu/g) > Ni (0.4 emu/g). The variation in SM values of the Fe + Co alloy particles ranged from 130 to 30 emu/g, decreasing as the fraction of Fe decreased.

Figures A-6-2 and A-6-3 show the effect of variation of ferrous cation concentration on the mean primary particle size and saturation magnetization (SM) respectively. Without any of the two additives,

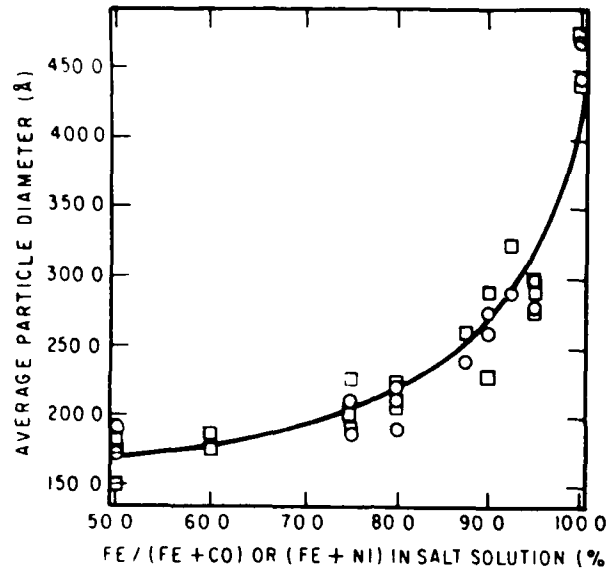

Figure A-6-1. Effect of metallic cation on mean primary particle size. Equimolar metallic cation reactant solution at 0.1 M in standard reducing solution with $CrCl_3$.
□ Fe + Co
○ Fe + Ni

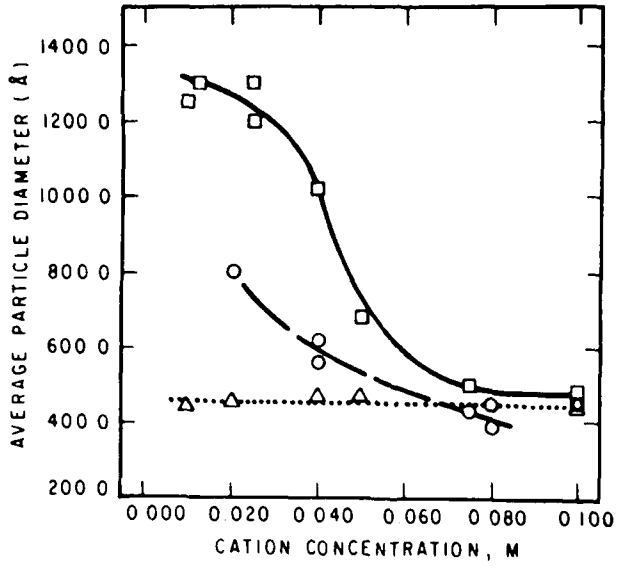

Figure A-6-2. Effect of ferrous ion concentration on mean primary particle size.
□ with $CrCl_3$ and NaOH
○ without $CrCl_3$ and with NaOH
△ without $CrCl_3$ and NaOH

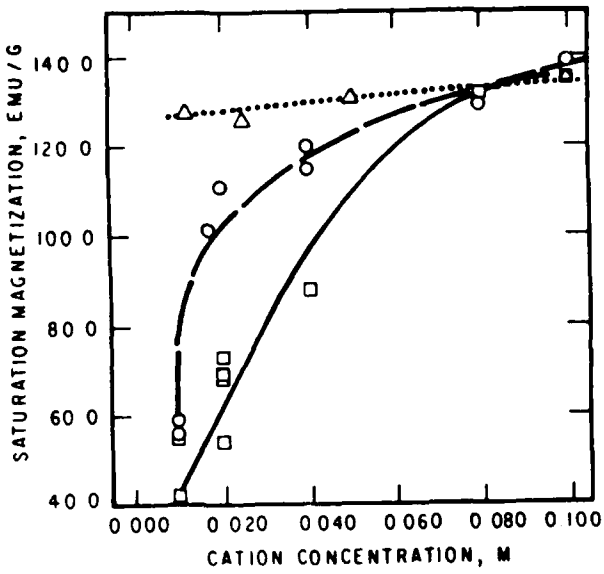

Figure A-6-3. Effect of ferrous ion concentration on saturation magnetization of particles.
|_| with $CrCl_3$ and NaOH
0 without $CrCl_3$ and with NaOH
Δ without $CrCl_3$ and NaOH

sodium hydroxide and chromium (III) chloride, the mean primary particle size is not affected by the variation of ferrous cation concentration. With the "standard" reducing solution, the mean primary particle size shows great variation with ferrous ion concentraiton. In this case, as shown in Figure A-6-2, above a critical cation concentration, the mean primary particle size remains nearly constant, while below that concentration, the particle size increases rapidly. These large particles tend not to form chains in the absence of an external magnetic field, indicating that these particles are of multidomain size. The transition noted takes place at higher ferrous ion concentrations and is steeper

when chromium (III) chloride (0.002M) is added to the ferrous chloride reactant solution. In the absence of the two additives, the saturation magnetization (SM) did not vary with ferrous ion concentration. Upon addition of NaOH, the SM drops rapidly at approximately the same critical ferrous cation concentration observed for variation of mean primary particle size. Below the critical ferrous ion concentration, where larger particles are produced, it was found that the mean size and SM values were highly dependent on residence time in the reactor system. Below the critical ferrous cation concentration, a gel-like green non-magnetic material first appeared and then slowly changed into black or dark brown ferromagnetic particles. The lifetime for the green gel increased as the ferrous cation concentration was lowered. In this same regime, at a constant ferrous ion concentration in the reactant solution, a higher initial NaOH concentration led to longer lifetimes of the green gel. The existence of this phenomenon was also corroborated by electron micrographs and SM measurements. Precipitate obtained for small residence times in the reactor system (approximately 1 min.) appeared in electron micrographs as sheet-like nets with very small spherical particles in some of the nets; this is shown in Figure A-6-4. Subsequently, for larger residence times, these small particles appeared to grow at the expense of the net material while the SM values increased and finally reached the values (about 130 emu/g) characteristic of particles formed above the critical value of ferrous ion concentration. All the data shown in Figures A-6-2 and A-6-3 were obtained from samples whose residence time in the reactor system was 5 minutes.

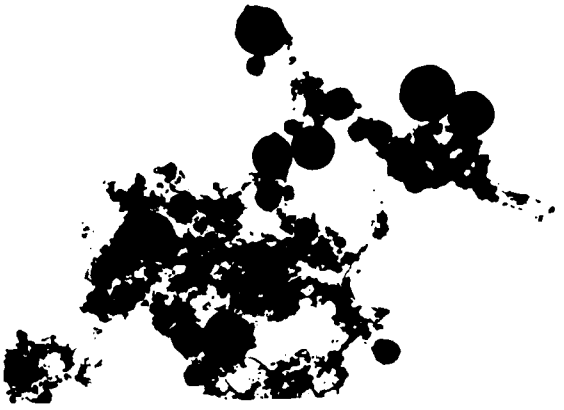

Figure A-6-4. Primary particle formation below critical ferrous ion concentration. Standard reducing solution and 0.01 MFe^{++}. Ferromagnetic particles are shown in growth sites in hydroxide get sheet-like nets. Residence time in reactor system was 5 min.

Since particles are produced as a result of chemical reaction, it might be expected that the reaction temperature would be an important parameter in the formation of primary particles. In the study of the effect of temperature, the entire reactor system was maintained at a fixed temperature, which could be varied from 5 to 50°C. Figure A-6-5 shows the variation of mean primary particle size with temperature for 0.1 M ferrous ion initial reactant concentration and the standard borohydride solution (0.1 M with 0.1 wt. % NaOH). As the reaction temperature increased the mean primary particle size decreased, being at 50°C less than half that at 5°C. At the same time the chaining tendency and SM values were not affected by the temperature of the reactor system. Since the reaction was exothermic and the reactor system did not permit maintenance of the system free of temperature gradients, the actual reaction temperatures were slightly greater than the nominal values shown for Figure A-6-5.

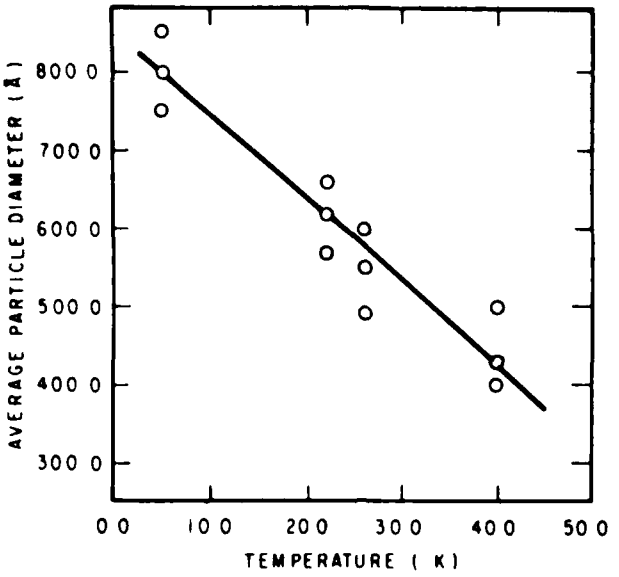

Figure A-6-5. Effect of reactor temperature on mean primary particle size. Ferrous ion (0.1 M) reactant solution in standard reducing solution.

Additives in the borohydride reduction reaction have been used by others to modify particle characteristics. A limited investigation was carried out on the effects of various additives on particle characteristics. When a small amount of gelatin (0.5 wt. %) is added to 0.1 M ferrous ion reactant with the standard reducing solution, random clusters are formed instead of chains. Similar behavior was found with addition of sodium citrate to the ferrous ion reactant. The addition of Cr^{+3} at 0.002 M in 0.1 M ferrous ion reactant solution led to increases in the SM values of the resultant particles. However, when the chromium ion concentration was increased to 0.005 M in the 0.1 M ferrous ion reactant solution, the chaining tendency of the resultant particles was significantly reduced as was the SM value. Addition of chromium was also found to prevent oxidation of the particles. Without chromium, from electron micrographs of the particles a noticeable film was observed to form on particle samples after an exposure time to air of one day. This

film had an amorphous structure from the electron diffraction pattern, and based on Olsen's findings[82], was believed to be iron oxide. When chromium was added to the ferrous ion reactant solution, no film was observed to form on the particles produced even after exposures of samples to air for as long as six weeks.

If borohydride reduction of ferromagnetic cations was carried out in solvent mixtures of water and ethyl alcohol, it was found that mean diameters of the primary particles decreased as the fraction of ethyl alcohol in the solvent increased. There is currently no explanation for this solvent effect. However, the SM values of particles produced with from 0 to 50 volume % ethyl alcohol as solvent remained constant.

External magnetic fields greater than approximately 500 Gauss applied to the reactor system produced highly linear chains with little or not branching. The external field was varied over the range 0 to 12500 Gauss, but no appreciable changes in primary particles or their chain formation were observed after the field exceeded 500 Gauss.

The saturation magnetization (SM) values for particles produced from 0.1 M ferrous and 0.1 M cobaltous reactant solutions were 130 and 30 emu/g respectively. These values are small compared to the values for pure bulk iron and cobalt. The lowered SM values are attributed here to the admixture of boron in the particles and to the small particle size. The small size of the cobalt and nickel particles imply a larger Brownian diffusivity than that for the larger iron particles. This higher

diffusivity, together with lower SM values, are believed to be responsible for the reduction in chain formation for the nickel and cobalt particles. Reduction in chain formation was also observed for the larger iron particles formed from reactant solutions with ferrous ion concentrations below the critical value shown in Figure A-6-2. These larger particles did not form chains even though their SM values were the same as the iron particles produced from higher concentration ferrous ion reactant solution (130 emu/g). This failure to form chains is attributed to the multidomain nature of these large particles.

The explanation for the effect of temperature on mean primary particle size is straightforward. Higher reaction temperatures are believed to result in higher reaction rates which in turn result in higher rates of production of metal atoms available for nucleation. Therefore, more nuclei are formed at higher temperatures and, as a result, fewer metal atoms are available for condensation on the nuclei. This picture is supported also by the variation of mean primary particle size with the cation and the chemical analysis of the associated particles. As Table A-6-1 shows, the atomic ratios of Co/Fe and Ni/Fe are always greater than one, even though the reactions occurred in reactant solutions that were equimolar in the two cations. The higher proportion of nickel and cobalt in the particles suggests that iron cations are reduced more slowly than the cobalt and nickel cations. In addition, it may be noted that pure nickel and cobalt cation reactant solutions yielded smaller mean primary particle sizes than those found for the

ferrous ion; this confirms the view that higher reaction rates result in smaller mean primary particle sizes.

From the experiments on variation of concentration of ferrous ion in reactant solution, summarized in Figure A-6-2, it appears that there are two quite separate mechanisms for formation of primary particles by borohydride reduction. Below the critical ferrous ion concentration indicated in Figure A-6-2, the first step in formation of primary particles is the formation of a green gel, probably an hydroxide, which is nonmagnetic and has the appearance of a sheet-like net in transmission electron micrographs (see Figure A-6-4). Baltz et al.[83] observed this sheet-like net in some of their samples and identified it as FeOOH by electron diffraction. However, Detourney et al[84] as well as Bernal et al[85] observed this green gel in an electrolytic bath for production of iron particles and found it to be a more complex material than FeOOH which slowly changes in FeOOH. On the basis of studies of this process at various reaction times, it is suggested here that below the critical cation concentration the hydroxide complex forms first, and that possibly active sites in the hydroxide gel become the centers for subsequent reduction to iron to form primary particles. Above the critical ferrous ion concentration, the sheet-like nets of green hydroxide gel are not observed; instead primary particles are formed directly in the reaction. Therefore, at the higher ferrous cation concentrations, it is inferred that the rate of the reduction reaction is higher than that of the hydroxide complex reaction.

As noted previously, in all the reaction systems the primary particles collided to form aggregates. The details of the various aggregation processes observed in these experiments are not well understood. Therefore, a measure of these aggregate structures may be of aid in studying the aggregation mechanisms. Such a measure is the Hausdorf or fractal dimension[86] of an aggregate which has been applied in investigation of a variety of aggregation processes, such as formation of branched polymers, the sol-gel transition formation of soot particles, etc. To date, most of the investigations of this concept[87,88] have involved computer simulations of model growth processes which give scale invariant aggregate structures that can be described as fractals. In the regime of scale invariance, the mass of a cluster or aggregate is predicted to scale as L^D, where L is a measure of the cluster size and D is the Hausdorf or fractal dimension. From the present experimental electron micrographs, estimates of the Hausdorf dimension of many aggregates were obtained by correlating the number of particles in any aggregate to a characteristic length of the aggregate -- in this case the geometric mean of the longest linear dimension of the aggregate and the length perpendicular to that axis. The correlations were carried out for aggregates produced by the standard solution borohydride reduction in the reactor system of pure 0.1 M ferrous ion and pure 0.1 M cobaltous ion in the absence of any external magnetic field. These correlations are shown in Figures A-6-6 and A-6-7, and the data are well described by a power law as would be expected for fractal objects. The fractal dimension for the

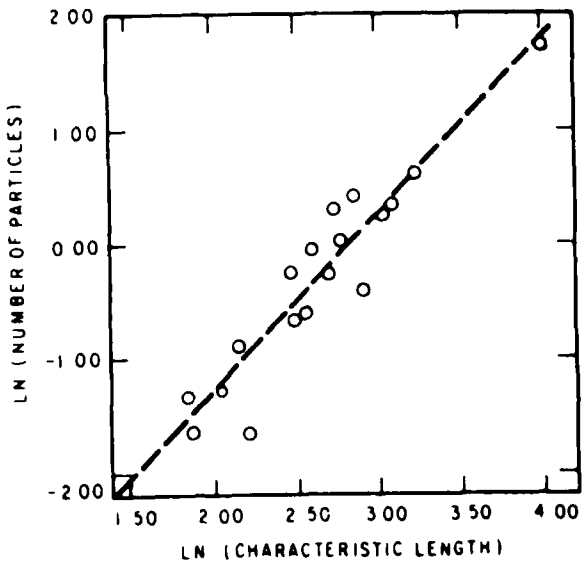

Figure A-6-6. Fractal geometry of iron particle aggregates prepared from 0.1 M Fe^{++} reactant solution in standard reducing solution. Fractal dimension is 1.54.

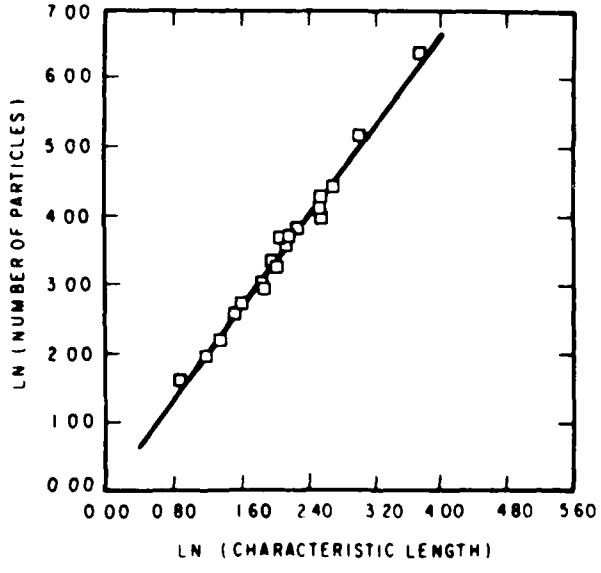

Figure A-6-7. Fractal geometry of cobalt particle aggregates prepared from 0.1 M Co^{++} reactant solution in standard reducing solution. Fractal dimension is 1.72.

aggregates of the iron particles was 1.54 while that for cobalt particles was 1.72. It should be noted that the Hausdorf dimension of linear chain particles would be 1.0, and this is, of course, observed for the iron particles under external magnetic fields greater than 500 Gauss. It is clear from Figures A-6-6 and A-6-7 that the iron particle aggregates, with their larger saturation magnetization values, exhibit a greater degree of "linearity" than do the cobalt particle aggregates. The Hausdorf dimension in this case may be a useful measure of the trend toward linearity of ferromagnetic particle aggregates and the magnetic properties of the primary particles.

b. Theory

In this paper, only the processes leading to the formation of the primary particles are considered in the context of a theoretical model; this model is intended to provide only a qualitative interpretation of the experimental results presented above for particle formation above the critical cation concentration. Additional work will be reported concerning models for chaining and aggregation of these primary particles.

In the borohydride reduction of metallic cations, the cations are reduced to metal atoms. In the liquid phase, these atoms have such low solubility that nucleation occurs with effectively zero activation energy and the dimer is the smallest stable cluster. As reaction proceeds, clusters may grow by accretion of atoms and other clusters. A

central question in consideration of the formation of primary particles is the relative contribution to the growth process of condensation of atoms and collision with other clusters (i.e. coagulation). In aqueous phase in the absence of external magnetic fields, collisions between clusters are subject to three principal interaction energies between a pair of clusters. These are van der Wallas, hydrodynamic and double layer energies. The van der Waals forces arise from the synchronized dipoles created by fluctuations in the electron clouds of the constituent atoms composing the clusters. Hydrodynamic forces arise from the interaction between a pair of particles with relativemotion in a viscous medium. Double layer forces are due to the interactions between the electrical double layers surrounding each particle. Of these three forces, only the van der Waals force is attractive. Analysis of these forces is the starting point for consideration of the stability of colloidal dispersions.[89,90] The general picture is that van der Waals attraction predominates at small and large interparticle distances; at intermediate distances, the electrical double layer forces may be dominant, depending on the relative magnitudes of these two forces. The hydrodynamic force is normally incorporated by a redefinition of the Brownian diffusion coefficients of a pair of particles. If the electrical double layer forces are dominant, the total energy as a function of interparticle distance displays a positive maximum and the disperse system is stable; the system exhibits what is termed slow coagulation.[91] If the double layer forces are not dominant at intermediate distances, the disperse system is unstable and exhibits what has been termed rapid

coagulation. These considerations are of obvious importance in the model development presented below. Intercluster magnetic forces are not considered since the clusters are below the critical domain size.

The physical system to be described consists initially of a spatially homogeneous mixture of borohydride ions and metallic cations in basic aqueous phase; the cation concentration is taken to be greater than the critical value so that the hydroxide mechanism is not included. The ensuing reduction reaction constitutes the source of metal atoms that undergo a zero activation energy nucleation process to form clusters. These clusters grow by accretion of additional atoms and possibly by accretion of other clusters. Conservation equations can now be applied which describe the formation and growth of the primary particles.

The conservation equation for metal and boron atoms has the form:

$$dc/dt = RXN - (1/m_1) \int_{x*}^{\infty} \psi(x,c,t)\, n(x,t)\, dx - 2R \qquad (A\text{-}6\text{-}1)$$

where c is the number concentration of metal and boron atoms. m_1 is the effective atomic mass. It is assumed that metal and boron are produced by the reaction and are both incorporated in the particle formation process. RXN is the rate of production and metal rate coefficients. The second term on the right hand side represents loss of atoms by attachment to existing particles, being the growth rate of a particle mass x and $n(x,t)$ the mass distribution function of particles. R represents loss of atoms by nucleation of clusters.

There have been no rate studies which have established quantitative values for RXN for the borohydride reduction of metallic cations. Ivanov et al.[92] have carried out a mechanistic study for the reduction of nickelous cations by borohydride in basic aqueous solution. Their mechanism is derived from mass spectroscopic studies of the reaction in deuterium oxide. They proposed the following mechanism which is used in the present analysis:

$$BH_4 + 4HOH + 2NI^{2+} = 2Ni + 2H_2 + 4H^+ + BO_2 + 2H_2O$$

$$BH_4 + H^+ = B + 2.5H_2$$

$$BH_4 + 4HOH = BO_2 + 4H_2 + 2H_2O \qquad (A\text{-}6\text{-}2)$$

from this mechanism the following rate expression is used for RXN:

$$RXN = 6k_1 [BH_4] [Ni^{2+}]^2 \qquad (A\text{-}6\text{-}3)$$

The rate coefficient k_1 is an unknown parameter which is varied in this analysis.

In liquid phase, particles grow in the continuum regime. The growth rate for this regime has the form:

$$. = 2kTm_1^{2/3}x^{1/3}c/3u = \psi_1 x^{1/3}c \qquad (A\text{-}6\text{-}4)$$

The nucleation term has the form:

$$R = R^* (x - x^*) \qquad (A\text{-}6\text{-}5)$$

where x^* is the mass of the smallest cluster, a dimer in this case and R^* is the coagulation rate. δ is the delta function. The quantities in equation (A-6-5) are defined:

$$x^* = 2m_1$$

$$R^* = b_{11}c^2, \quad b_{11} = 8kT/3\mu$$

where kT is the thermal energy and μ the viscosity coefficient.

The particle evolution equation is given by:

$$\frac{\partial n(x,t)}{\partial t} = \frac{1}{2}\int_{x^*}^{x} E\, b(x-x',n)\, n(x-x',t)\, n(x',t)\, dx'$$

$$- n(x,t) \int_{x^*}^{\infty} E\, b(x',x)\, n(x',t)\, dx'$$

$$- \frac{\partial}{\partial x}[\psi(x,c,t)\, n(x,t)] + R \qquad \text{(A-6-6)}$$

The first two terms on the right hand side account for coagulation of particles and the rate coefficient is given by the continuum regime expression.[93] E is the collision efficiency, $(0 < E < 1)$. b is the Smoluchowski collision rate. The third term represents particle growth by condensation.

For a qualitative picture of the formation process of primary particles it is sufficient to obtain an approximate solution of these equations through a moment technique for the particle phase. The k-th moment of the particle size distribution function is:

$$M_k(t) = \int_{x^*}^{\infty} x^k n(x,t)\, dx \qquad \text{(A-6-7)}$$

The set of moment equations is closed through the assumption that the particles evolve through time with a lognormal size distribution. The k-th moment of the size distribution is therefore given in terms of the lognormal parameters, x_g the geometric mass and σ the geometric standard deviation:

$$M_k(t) = M_0 x_g^k \exp(9k^2 \ln^2 \sigma/2) \qquad \text{(A-6-8)}$$

Any fractional moment of the distribution can be expressed in terms of the three moments M_0, M_1 and M_2, and the moment equations are therefore closed. The mean particle diameter, D_m, can be expressed in terms of these moments:

$$D_m^3 = 6M_0^{-3/2} M_1^2 M_2^{-1/2} / \rho\pi$$

The atom conservation equation and the moment equations analyzed here have the form:

$$dc/dt = RXN - M_{1/3}\psi_1 c m_1 - b_{11}c^2 \qquad \text{(A-6-9)}$$

$$dM_0/dt = b_1(M_0^2 + M_{1/3}M_{-1/3}) + b_{11}c^2/2 \qquad \text{(A-6-10)}$$

$$dM_1/dt = M_{1/3}\psi_1 c + m_1 b_{11} c^2 \qquad \text{(A-6-11)}$$

$$dM_2/dt = 2M_{4/3}\psi_1 c + 2b_1(M_1^2 + M_{4/3}M_{2/3}) + 2m_1^2 b_{11} c^2 \qquad \text{(A-6-12)}$$

The set of equations (A-6-9)-(A-6-12) can now be solved numerically to give a qualitative picture of the growth processes of primary particles. Solutions have been obtained for two cases which correspond to slow coagulation, E=0 (designated as Case 1) and rapid coagulation, E=1 (designated as Case 2). The initial conditions used were:

$$c(0) = M_3(0) = M_1(0) = M_2(0) = 0;\ Fe^{2+} = BH_4 = 0.1M.$$

Quantitative information on the rate coefficients for borohydride reduction of metallic cations was not available. Certain qualitative features of primary particle growth can, however, be examined. First, there is the observation that higher reduction rates, whether brought about by higher temperatures or change of cation from iron to cobalt or nickel, lead to smaller mean diameters of primary particles. Second, it is uniformly observed that primary particles produced under given reaction conditions have a narrow particle size distribution. An acceptable mechanism for primary particle formation and growth must account for these observations.

The moment equations, (A-6-9)-(A-6-12), were solved for Cases 1 and 2 for two orders of magnitude variation in the rate coefficient, k_1. Since quantitative rate data were not available, the values are only esitmates chosen to give a reasonable range of particle production rates. For Case 2, E=1, solution of equations (A-6-9)-(A-6-12) result in variations of primary geometric mean particle diameter with reaction rate that are exactly opposite to experimentally observed variation; in the simulations, mean diameters increase with increasing reaction rates. Also, for Case 2 the geometric standard deviations are much larger than those found for Case 1, E=0, and for the smallest reaction rate studied continuously increase with time. The solution of equations (A-6-9)-(A-6-12) for Case 1, E=0, give variations of geometric mean primary particle

diameters and standard deviations with time and reaction rate shown in Figures A-6-8 and A-6-9. These results agree qualitatively with the experimental observations that mean particle diameters decrease with increasing reaction rates and the particles are narrowly distributed in size.

These numerical and experimental results are consistent with the hypothesis that primary particle growth takes place primarily by the process of condensation of atoms onto nuclei and that collisions between clusters is suppressed. This suppression is attributed to the electrical double layer forces between clusters.

c. Discussion.

This study has shown that primary ferromagnetic particles with diameters from 5 nm to 1 μm and with saturation magnetizations from 0 to 130 emu/g can be prepared by control of various experimental parameters including the metallic cation(s), the metallic cation concentration, the reaction temperature, and the use of additives. The tendency of the primary particles to form chains is strongly affected by the saturation magnetization, the size of the primary particles, and the presence of external magnetic fields. The chaining mechanism was studied indirectly through determination of the fractal dimensions of iron and cobalt aggregates of known saturation magnetization formed in the absence of an external magnetic field; iron aggregates with higher saturation magnetization (130 emu/g) had a lower fractal dimension (1.8) than cobalt aggregates (fractal dimension of 1.9) with lower saturation

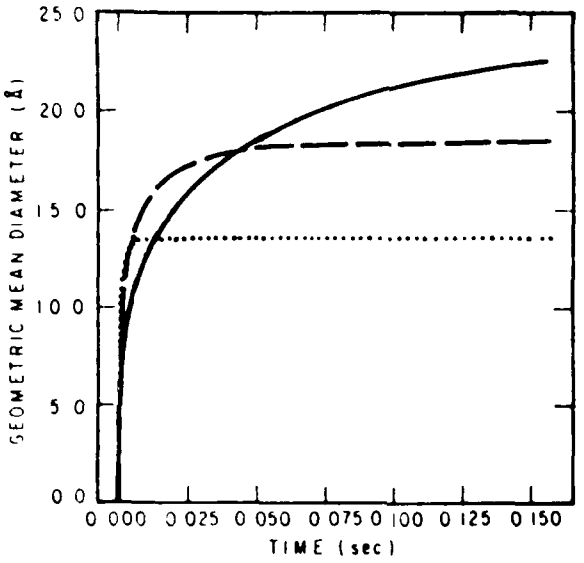

Figure A-6-8. Variation of geometric mean primary particle diameter with time for three values of chemical rate coefficient for Case 2, collision efficiency between clusters, E=0.

_____ k_1 = 2.5E-41 (cm^{-6}-sec.)
_ _ _ _ k_1 = 2.5E-40 (cm^{-6}-sec.)
..... k_1 = 2.5E-39 (cm^{-6}-sec.)

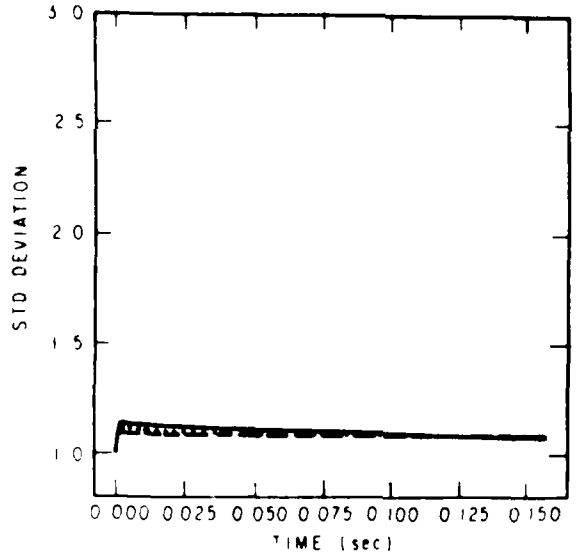

Figure A-6-9. Variation of geometric standard deviation with time for three values of chemical rate coefficient for Case 2, collision efficiency between clusters, E=0.

_____ k_1 = 2.5E-41 (cm^{-6}-sec.)
_ _ _ _ k_1 = 2.5E-40 (cm^{-6}-sec.)
..... k_1 = 2.5E-39 (cm^{-6}-sec.)

magnetization (30 emu/g). Volume and surface compositions of primary particles were determined by Inductively Coupled Plasma Emission Spectroscopy and X-ray Photoelectron Spectroscopy. It was found that atomic ratios of metal to boron was around 2 and that the boron was concentrated on the surfaces of the particles. Alloy particles prepared from equimolar Fe-Co and Fe-Ni solutions always were enriched in Co or Ni, indicating a higher reduction rate for Co^{++} and Ni^{++} as compared to Fe^{++}.

Two mechanisms for formation for primary particles have been identified. One is found at low ferrous cation concentrations with basic borohydride solutions; in this regime, metallic particle formation appears to occur in sites in net-like hydroxide gel structures. The particles formed in this regime do not form chains in the absence of an external magnetic field and are of multidomain size with a crystalline diffraction pattern. At higher metallic cation concentrations in basic borohydride solutions, formation of ferromagnetic primary particles occurs directly from the metal atoms produced by the reduction reaction; these particles are of single domain size and do not exhibit a crystalline diffraction pattern. In the absence of sodium hydroxide in the reducing solution, the mean primary particle size is not affected by variation of cation concentration; in this case the borohydride hydrolysis reaction is important.

Mean primary particle size decreased and saturation magnetization decreased as the cation was changed from Fe to Co or Ni; alloy

particles of Fe+Co and Fe+Ni similarly decreased in mean size and saturation magnetization as the fraction of iron in the reactant solution was decreased. The addition of chromium chloride to the ferrous chloride reactant solution resulted in primary particles that exhibited no oxidation upon exposure to air for six weeks; in the absence of chromium chloride, collections of particles were pyrophoric and iron oxide was identified in micrographs of individual particles after exposure to air for one day. In all cases, increase of the reaction temperature resulted in smaller primary particles. When the reduction reaction was carried out in solvent mixtures of water and ethyl alcohol, mean primary particle size decreased as the fraction of ethyl alcohol increased.

A relationship has been demonstrated between fractal dimension of aggregates, their saturation magnetization, and the chaining tendency of the primary particles. Aggregates of primary iron particles with saturation magnetization of 130 emu/g had a fractal dimension of 1.54 whereas aggregates of primary cobalt particles with saturation magnetization of 30 had a fractal dimension of 1.72. Linear chain particles have a fractal dimension of 1.0.

A model for growth of primary particles above the critical cation concentration in basic solution has been developed which gives results in agreement with experimental observations. The model indicates that primary particle growth takes place in this regime primarily by condensation of atoms onto nuclei and that collisions between clusters is probably suppressed by electrical double layer forces. Subsequent to

their formation, primary particles in the presence of [illegible] magnetic fields greater than approximately 500 Gauss collide to form linear chains owing to the interparticle magnetic forces which [illegible] play for particles of critical domain or multidomain sizes.

4-1. Dispersion of aerosol plumes

The dispersion of a plume of volatile aerosol is a familiar process whose simulation is of practical importance. Aqueous fogs from cooling towers and other industrial sources can cause reduction in visibility, with concomitant hazards. In industrial, agricultural, and military technology an understanding of the dynamics of volatile aerosol plumes is necessary. Realistic simulation of the processes involved in these applications is possible only by numerical techniques. Consequently, this paper reports our investigation of reliable and accurate numerical schemes for such simulation.

The problems arising in numerical simulation of the dispersion of a plume of volatile aerosol are clearly shown by studying a crosswind line source. This choice obviates the need for a subgrid scale model to approximate a point source; any error is strictly due to the numerical methods used in the simulation. Also, a number of previous studies of aerosol plume dynamics are available for the [illegible] case.[104,105] For these reasons we use the crosswind line source as the basis for this study.

This paper presents [illegible]

First, the relevant equations for this process are discussed. Next, the numerical schemes for their solution are outlined. Finally, the numerical schemes are tested against analytical solutions and are used in the simulation of dispersion under realistic atmospheric conditions.

a. Theory.

For clarity, we choose to describe the dispersion of an aerosol consisting of a single chemical species in inert host gas. The aerosol concentration is sufficiently low that it may be regarded as a passive contaminant. Also, the evaporation process is sufficiently slow that that evolution of the plume may be treated as an isothermal process. In addition, it is assumed that the turbulent processes can be represented by first-order closure assumptions.

With these restrictions we study the evolution of the particle number density function n(m,x,z,t), where n(m,x,z,t)dm is the number of particles having masses in the range m,dm at downwind position x at height z at time t. The evolution equation is

$$\frac{\partial n(m,x,z,t)}{\partial t} + U(z)\left[\frac{\partial n(m,x,z,t)}{\partial x}\right] + \frac{\partial}{\partial m}\left[\dot{m}(m,s)\, n(m,x,z,t)\right]$$

$$= -\frac{\partial}{\partial z}\left[V(z)\left[\frac{\partial n(m,x,z,t)}{\partial z}\right]\right] + G_z(m)\left[\frac{\partial n(m,x,z,t)}{\partial z}\right]. \qquad (A-1-1)$$

This equation is coupled to the conservation equation for the vapor, which we give in terms of the saturation ratio s:

$$\frac{\partial s(x,z,t)}{\partial t} + U(z)\left[\frac{\partial s(x,z,t)}{\partial x}\right] = \frac{\partial}{\partial z} K(z)\left[\frac{\partial s(x,z,t)}{\partial z}\right]$$

$$- \frac{1}{c_v} \int \beta(m,s)\, n(m,x,z,t)\, dm. \qquad \text{(A-7-2)}$$

Equations (A-7-1) and (A-7-2) are subject to the following initial and boundary conditions:

$$n(m,x,z,0) = 0,$$

$$s(x,z,0) = 0, \qquad \text{(A-7-3)}$$

$$n(m,0,h,t) = [Q_0/U(h)]\,\delta(z-h)\,f(m), \qquad \text{(A-7-4)}$$

$$s(0,h,t) = 1.0, \qquad \text{(A-7-5)}$$

$$\frac{\partial n(m,x,H,t)}{\partial z} = \frac{\partial s(x,H,t)}{\partial z} = 0, \qquad \text{(A-7-6)}$$

$$n V_d(m) = K\, \partial n/\partial z, \quad z = 0, \qquad \text{(A-7-7)}$$

$$\partial s/\partial z = 0, \quad z = 0. \qquad \text{(A-7-8)}$$

$U(z)$ is the x component of the mean fluid velocity, and $K(z)$ is the vertical eddy diffusivity. $G_z(m)$ is the gravitational settling speed for a particle of mass m. Q_0 is the source strength, h its height, and $f(m)$ the source size distribution. H is the mixing height, $V_d(m)$ is the deposition velocity of a particle with mass m.

$\beta(m,s)$ is the condensation/evaporation growth law for a particle. We use the following approximate expression, due to Fuchs and Sutugin:[99]

$$\beta_{fm} = 4\pi D_{gj} m^{1/3} c_v (s - e^{Ke}) \left(\frac{1.33Kn + 0.71}{1 + Kn^{-1}} \right)^{-1}, \qquad (A\text{-}7\text{-}9)$$

where the diffusion coefficient D_{gj} of vapor j in host gas is related to the mean molecular speed v_j and the mean free path L_j by $D_{gj} = 1/3\ v_j L_j$. In Equation (A-7-9), ρ_p is the particle density; Kn the Knudsen number, $Kn = 2L_j/D_p$; and D_p is the particle diameter. The saturation ratio $s = c/c_v$, where c is the vapor mass concentration and c_v is the vapor mass concentration corresponding to the bulk liquid vapor pressure at plume temperature T. Ke is the Kelvin number, $Ke = 4\sigma v/D_p kT$. σ is the surface tension, v the particle's molecular volume, and kT the thermal energy.

Some of the important observables of n(m) are the total particle number concentration N,

$$N = \int_0^\infty n(m)\ dm;$$

the particle mass concentration M,

$$M = \int_0^\infty mn(m)\ dm;$$

and the total extinction coefficient β_{ext}, obtained from the normalized extinction efficiency Q_{ext}:[100]

$$\beta_{ext} = \left(\frac{3}{4\rho_p} \right)^{2/3} \int_0^\infty Q_{ext} m^{2/3} n(m)\ dm.$$

These are used in the following analysis of results.

b. Background and Procedure

[illegible] and condensation/evaporation terms, accurate numerical solution of Equation (A-7-1) cannot be achieved by a

routine application of classical numerical methods. Numerical approximation of these terms by such methods is well known to lead to substantial numerical dispersion and diffusion. Our aim in this study is to obtain numerical results of high accuracy by techniques that enable one to reduce to any desired level errors such as numerical dispersion and diffusion.

With respect to simulation of the advection and dispersion terms in Equation (A-7-1), Tsang and Brock[104] concluded that Fromm's method[97,98] for advection and orthogonal collocation on finite elements[96] for diffusion gives reliable numerical schemes. Tsang and Brock[104] successfully used the method of fractional steps[107] in the study of coagulation in a dispersing plume from a crosswind line source. One of the purposes of this study is to demonstrate the utility of these methods in plumes undergoing the condensation/evaporation process.

The condensation/evaporation term has long posed a major problem in aerosol dynamics simulations. Numerical simulation of this first-order hyperbolic evolution equation remains as a challenging problem in computational physics and engineering. For first-order hyperbolic equations, most numerical schemes exhibit either numerical dispersion (manifested as oscillations over some region) or numerical diffusion (dissipation of the amplitude of a distribution or the smearing of the front). Both numerical dispersion and diffusion are obviously undesirable in simulating the evaporation/condensation of aerosols. Recently, Tsang and Brock[106] devised a novel numerical scheme for such simulation.

Comparison of the numerical solution and known analytical solution shows that the scheme gives very accurate results. Case studies at various conditions were carried out. For the evaporation problem, it was found that the finite-element method (LFEM) using linear basis functions and natural boundary conditions[94] gives accurate results. Here we combine the numerical algorithm for advection and diffusion used by Tsang and Brock[104] with the finite-element method for evaporation to study a volatile aerosol plume. Only steady state solutions are presented in this paper.

The numerical solution of the coupled integro-partial differential Equations (A-7-1) and (A-7-2) presents a challenging problem. The simultaneous solution by an implicit numerical scheme using a matrix technique for 10^4-10^5 unknowns is no trivial task. In this work the method of fractional steps is used in the simulation. Advection, diffusion, and evaporation are included as follows:

1. Solve the advection and diffusion equation J_{max} times, where J_{max} is the number of size classes.
2. Solve the evaporation equation by LFEM at each grid point.
3. Solve the advection and diffusion equation for s.
4. Calculate the integral term in Equation (A-7-2), which is a source term for vapor due to evaporation, and update the saturation ratio at that grid point.

If the saturation ratio of the vapor does not change with position - that is, is constant - procedures 3 and 4 are not necessary. The method of fractional steps just outlined decouples Equations (A-7-1)

and (A-7-2). The explicit nature of procedure 4 does not pose a problem, because the source term is counterbalanced by the dilution effect of advection and diffusion.

c. Results and Discussion.

In order to validate the computational procedure outlined in the previous section, we perform some convergence studies on the numerical scheme. For certain forms of U(z), K(z), and $\psi(m)$, analytical solutions are available. Here, we assume

$$U(z) = 2m \text{ sec}^{-1}, \quad K(z)=1 \text{ m}^2\text{sec}^{-1},$$

and $\psi = -am^{1/3}$ (this represents continuum evaporation, where $a=2\times10^{-11}g^{2/3}\text{sec}^{-1}$). We also assume that gravitational sedimentation and deposition are absent for this test problem; that is, $G_z(m)=0$ and $V_d(m)=0$. For vertical diffusion all the numerical results in this work were obtained by using six interior collocation points (the quadrature points of a shifted Legendre polynomial) in each finite element of sizes 2.07, 12.93, and 85 m. The source height is 2 m from the ground. For these restrictions, the analytical solution of Equation (A-7-1) is readily obtained by Fourier transform methods and the method of characteristics. Figures A-7-1 and A-7-2 show the comparison between analytical and numerical solutions at the source height for the total particle mass and number concentrations, respectively. x is the grid size in the x direction, Δt_e is the time step used in procedure 2 for evaporation. Normally, Δt_e for evaporation is usually less than that

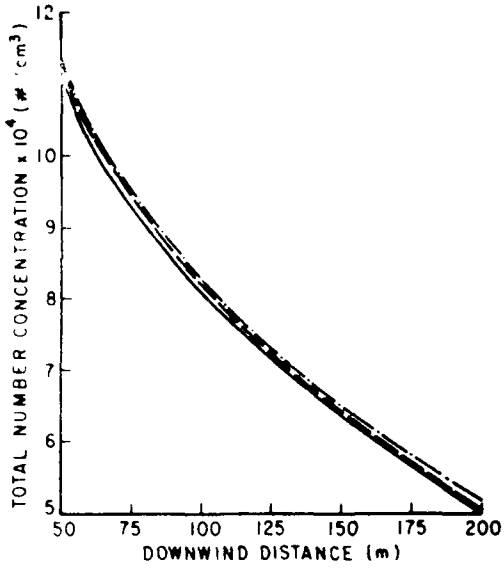

Figure A-7-1. Comparison between analytical solution (_____) and numerical solution (___·___, Δx=2.0 m, t_c=0.02 sec; ---, Δx=0.5 m, Δt_e=0.005 sec) at source height for total particle mass concentration.

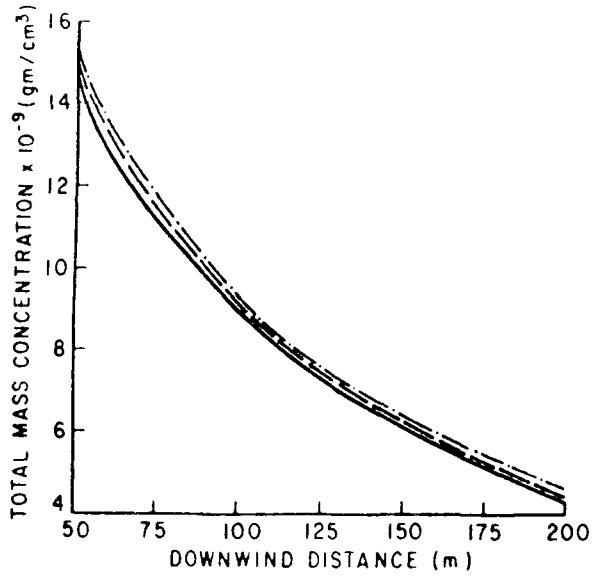

Figure A-7-2. Comparison between analytical and numerical solutions (___·___, Δx=2.0 m, t_e=0.02 sec; ---, Δx=0.5 m, t_e=0.005 sec) at source height for total particle number concentration.

for advection and diffusion. In this work, $\Delta t_e \sim 1/50 \Delta t_{ad}$, and so in practice we perform the advection/diffusion calculation every Δt_{ad} step rather than every Δt_e step. This saves computation time without sacrificing accuracy. Figures A-7-1 and A-7-2 show that as we decrease Δx and Δt_e, the numerical solution converges to the analytical solution converges to the analytical solution, thus demonstrating the validity of the method of fractional steps in volatile plume calculations. Figure A-7-3 shows a comparison between analytical and numerical solution at the source height for the number density function, $dN/d\log D_p$, for different downwind distances. The excellent agreement with the analytical result shows that the numerical method is accurate. One of the difficulties in solving the

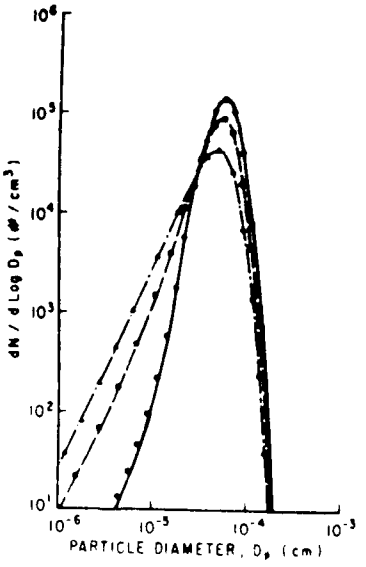

Figure A-7-3. Comparison between analytical solution (curves) and numerical solution (symbols) at source height for number density function, $dN/d\log D_p$, for different downwind distances (-o-, 50 m; -- --, 100 m; -· ·-, 200 m).

initial boundary value problem of first-order hyperbolic equations lies in the choice of appropriate boundary conditions and this is crucial in obtaining meaningful and accurate solutions. In Figure A-7-3, even at a downwind distance of 200 m, it is obvious that there is no boundary effect between particle diameters of 10^{-6} and 10^{-5} cm. The minimum D_p used in the simulation is 10^{-6} cm. Since computations must be performed on finite domains of particle diameters, and evaporation increases the number of smaller aerosol particles, this result shows that natural boundary conditions are appropriate in simulating evaporation of an aerosol.

With the tests of the numerical scheme completed for advection, diffusion, and evaporation, we use realistic atmospheric wind and diffusivity profiles for approximating evaporating plumes of simulated light and heavy oils (diesel and fog oil). The vertical eddy diffusivity profile is taken from the data presented by Smith.[103] The wind speed is from field measurements at Cape Canaveral under neutral stability (Panofksy[101]). Deposition velocity is taken from the data of Sehmel.[102] We assume the mixing height to be 100 m. The source height is 2 m from the ground. The line source size distribution is characterized by a log normal distribution with source strength of 0.3307 g m^{-1} sec^{-1}, geometric mean diameter of 0.6 m, and geometric standard deviation of 2.24. The particle density is assumed to be 1.0 g cm^{-3}. For the heavy oil (fog oil, or 100 pale oil) the average molecular weight is 300, the surface

tension is 35 dyn cm^{-1} and a constant bulk vapor pressure of 9.6×10^{-6} mm Hg is assumed. For calculation of σ_{ext}, the particle refractive indexes v_r with associated radiation wavelengths λ are $v_r = 1.5077 - 2.94 \times 10^{-5} i$, $\lambda = 3.39$ μm and $v_r = 1.44 - 0.1i$, $\lambda = 0.4416$ μm. For the light oil (diesel) the average molecular weight is 221, the surface tension is 20 dyn cm^{-1}, and a constant bulk vapor pressure of 1.5×10^{-3} mm Hg is assumed. The particle refractive indexes with the associated radiation wavelengths are $v_r = 1.522 - 0.064i$, $\lambda = 3.5$ μm and $v_r = 1.51 - 0.0i$, $\lambda = 0.5$ μm.

In order to demonstrate the roles of vapor conservation and the Kelvin effect, we carried out simulation studies of atmospheric plume dispersion at saturated conditions, s=1.0, and with s=s(x,z) according to Equations (A-7-1) and (A-7-2). Note that when s=1.0, only evaporation occurs owing to the Kelvin effect. Figures A-7-4 and A-7-5 show isopleths of total single-particle extinction (a sensitive index of changes in the density function) for the plume cross section ats=1.0 for the two wavelengths. Figures A-7-6 and A-7-7 are companion plots for the complete realistic simulation with vapor conserved under otherwise identical conditions. For the infrared wavelengths with the initial particle size distribution employed, σ_{ext} is very sensitive to the particle concentrations at the larger diameters; these particles disappear much more rapidly for the conserved case than for the case s=1.0, with attendant rapid decrease of σ_{ext} for the infrared in the conserved case.

Figure A-7-8 shows for the conserved case the number density function, $dN/d \log D_p$, for the oil aerosols at a downwind distance of 100 m at the source height of h=2 m. Under the conditions studied, the

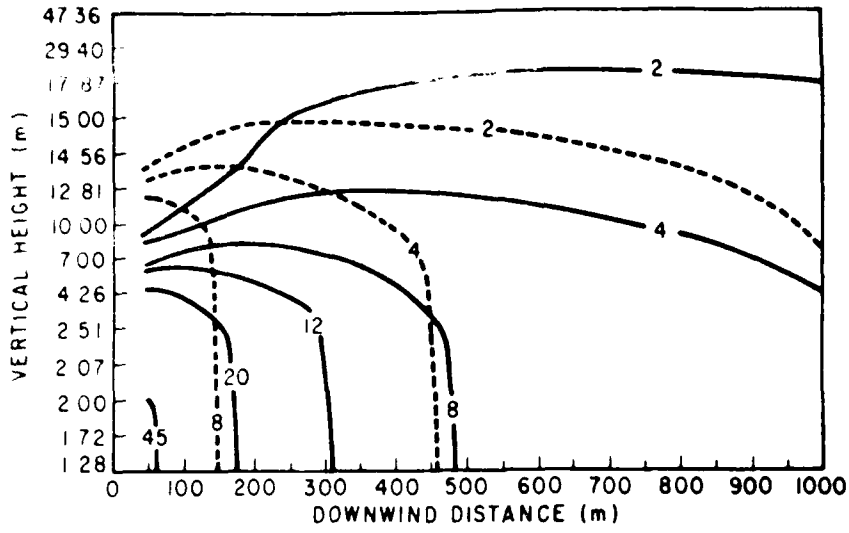

Figure A-7-4. Isopleths of total single-particle extinction σ_{ext} in the plume from a crosswind line source for s=1.0, σ_{ext} (in cm^{-1}) is equal to values given on isopleths times 5×10^{-5} (_____, fog oil, λ=0.441 μm; ---, diesel, λ=0.50 μm).

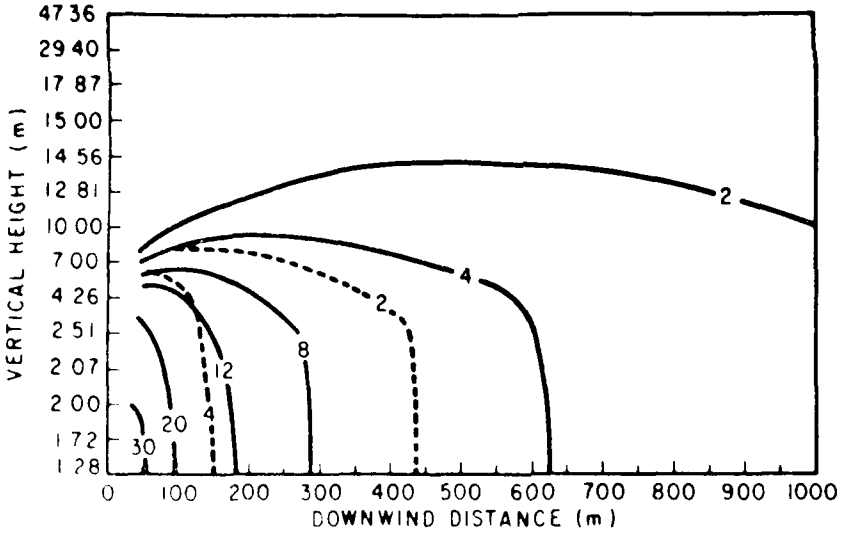

Figure A-7-5. Isopleths of total single particle extinction σ_{ext} in the plume from a crosswind line source for s=1.0, σ_{ext} (in cm^{-1}) is equal to values given on isopleths times 5×10^{-6} (_____, fog oil, λ=3.39 μm; ---, diesel, λ=3.50 μm).

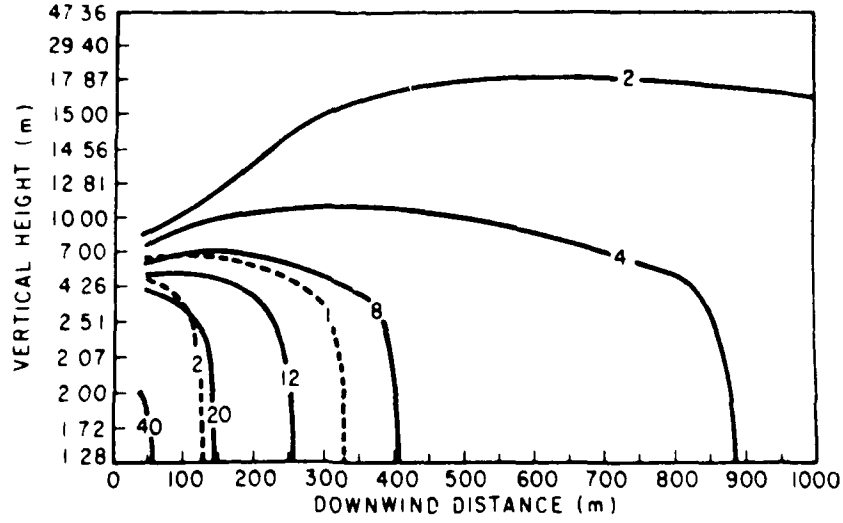

Figure A-7-6. Isopleths of total single particle extinction σ_{ext} in the plume from a crosswind line source with vapor conserved, σ_{ext} (in cm^{-1}) is equal to values given on isopleths times 5×10^{-5} (_____, fog oil, λ=0.441 μm; ---, diesel, λ=0.50 μm).

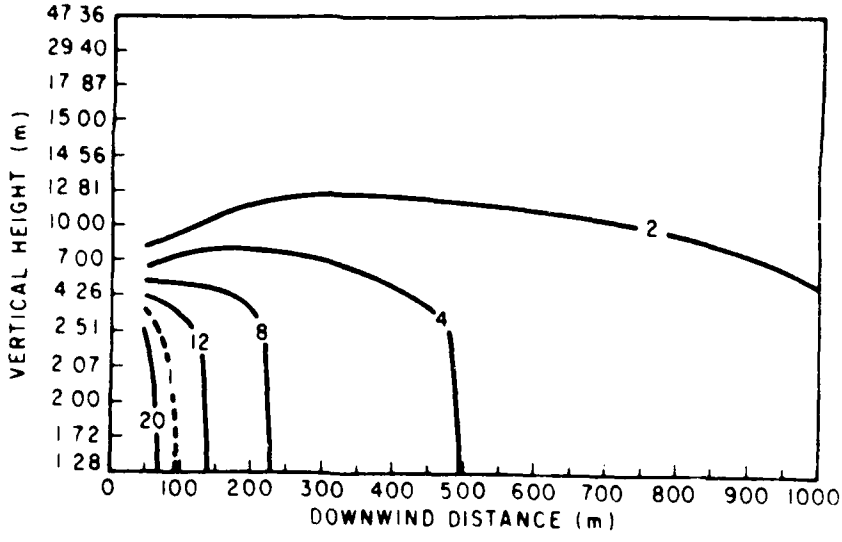

Figure A-7-7. Isopleths of total single particle extinction σ_{ext} in the plume from a crosswind line source with vapor conserved, σ_{ext} (in cm^{-1}) is equal to values given on isopleths times 5×10^{-5} (_____, fog oil, λ=3.39 μm; ---, diesel, λ=3.50 μm).

Kelvin effect causes a rapid increase of evaporation rate with decreasing particle diameter. As indicated in Figure A-7-8 for the heavy oil (fog oil), this causes an overall decrease in N and an increase of dN/d log D_p at smaller diameters, whereas dN/d log D_p is hardly altered by evaporation at the larger diameters. The vapor pressure of the light oil is sufficiently large that, as shown in Figure A-7-8, at x=100 m the entire density function is shifted to smaller diameters.

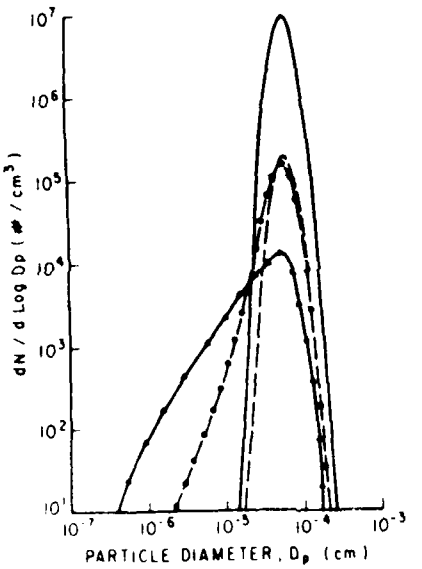

Figure A-7-8. Number density function dN/d log D_p for light and heavy oil aerosols in plume from a crosswind line source at x=100 m, h=2 m (_____, source distribution; ---, no evaporation at 100 m; --°--, evaporation of fog oil at 100 m, - · -, evaporation of diesel at 100 m).

3. Conclusions.

It has been demonstrated that dispersion of [illegible] aerosol can be simulated numerically by the method of [illegible]. For the special case where an analytical solution is [illegible] it has been shown that the numerical solution converges to the [illegible] solution with a reduction in step size; consequently the [illegible] numerical simulation can be reduced to any desired level. In the [illegible] comparisons, the validity of the method of fractional steps has been [illegible] with the attendant advantage over fully implicit schemes. From this and other studies it has been demonstrated that the finite-element method using linear basis functions and natural boundary conditions yields accurate numerical solutions for the evaporation process.

With the methods described in part here, [illegible] interesting problems in aerosol dynamics can now be studied. These include simulations of dispersion of plumes in which both coagulation and various condensation/evaporation processes occur. It would also be of interest to extend these procedures to other problems such as the multi condensation/evaporation processes in nonisothermal plumes, a problem of some importance.[35]

B. [illegible] INTERACTIONS

There is currently interest in the nonlinear interaction between laser beams and suspended particles. For very intense beams, particles may break up and propagation of a plasma column. At somewhat lower beam intensities, a particle may explode or fracture forming strong [illegible] in the viscosity of the particle. At low intensities, particles will evaporate rapidly with only small disturbances in the host gas. Work reported here is concerned with the last two of the interaction regimes noted above. First, work on particle explosion will be described. Then, work on fast evaporation of droplets.

B-1. Explosion of a water droplet by pulsed laser heating.

a. Introduction

The simulation discussed here addresses the following problem: A small aerosol droplet uniformly absorbs energy from a laser pulse. The duration of the pulse is so short that no fluid motion occurs during the pulse. The droplet absorbs enough energy that its final state after the pulse, but before any motion, is well above its critical point. The droplet subsequently explodes. We solve the conservation equations for the resulting spherically symmetric explosion. Uniform, instantaneous heating is assumed to simplify the heating process. Thus, we investigate the physics associated with the fluid motion after the heating.

Our results show that in the explosive regime, large nucleation rates can develop behind the shock of the exploding droplet. This phase transition can strongly influence both the hydrodynamics and the electrodynamics, and thus needs to be accounted.

In addition, a number of interesting experimental phenomena EMR-droplet interactions have been reported in the literature. convective motion is important to all of these phenomena. A realistic simulation of explosive vaporization can help to explain these occurrences.

We begin with a brief review of previous work on EMR-droplet interactions. Next, we discuss the theory of these interactions and apply the theory to the explosive vaporization of single water droplets. Finally, we present the results of our numerical simulation.

Many researchers are currently investigating how a very small droplet responds to applied electromagnetic radiation, and how the droplet subsequently alters the electromagnetic fields. This problem falls within the context of the larger problem of how to model and predict the effect of a system of discrete attenuators on the propagation of EMR. Thoroughly understanding this phenomenon will lead to advances in the microtechnologies (for example, the manipulation and control of submicrometer sized droplets, as in optical levitation) as well as advance our knowledge in the areas of laser propagation through a rainy or cloudy atmosphere, in situ analysis of combustion products, and astrophysics.

Broadly speaking, EMR interacting with a small droplet and its environment (in this case the atmosphere) manifests two types of response: electrodynamic and hydrodynamic. The Maxwell equations determine the electrodynamic response; the conservation equations for mass, momentum, and energy determine the hydrodynamic response. These partial differential equations, along with the constitutive relations that govern the physical properties of the system, and an equation of state determine the behavior of the system. The two sets of equations are strongly coupled through source terms in the primitive equations and through the constitutive relations.

We are currently working on the hydrodynamic aspects of this problem. To a first approximation, the effect of EMR on a small droplet is to generate heat within the droplet due to resistive heating. The rate at which the heat is generated determines the response of the droplet. The heating rate can vary over a wide range as determined by the complex index of refraction, the intensity of the radiation source, and the optical size of the droplet (Pendleton[123] and Greene et al.[119]). The optical size, also known as the Mie size parameter, is defined as $x = d/\lambda$ where d is the droplet diameter and λ is the wavelength of the incident light. The droplet shows an equally wide range of response, from slow evaporation to explosion. Thus, solving the problem for artibrary radiation intensity is very complicated.

A large body of literature has developed considering many aspects of this problem. For example, the articles by Yudanin and Lax,[129] Prishivalko,[124] and Chitanvis[117] illustrate the wide range of

effects that are being considered. Most of the current work addressing a realistic simulation of the hydrodynamics has dealt with the slow vaporization regime (see for instance Armstrong[109,110] and Sageev and Seinfeld[120]).

We are exploring the explosive vaporization regime of this problem. This regime is interesting because experimental studies have uncovered many unusual effects that seem be be based at least partly on strong convection. Among these are the lowering of the breakdown threshold for air containing small particles, and the appearance of jets of material emanating from a droplet (Chang[116]). Under some conditions, this behavior can be explained completely from hydrodynamic considerations, regarding the EMR simply as a source of heat. For instance, the lowering of the breakdown potential has been attributed to shock heating of the atmosphere (Steverding[127]). Also, the appearance of "cloudy" jets can probably be explained in terms of rapid, very localized vaporization at a hot spot near the surface of the droplet.

We have chosen a simple but very dynamic test problem as a first step towards developing a general solution for the convection dominated regime. By choosing a relatively simple hydrodynamical system, we can concentrate on simulating the physical properties of the droplet realistically. This in turn will help us determine what other physics (such as nucleation and particle growth) might arise due to strong convective effects. The physical system examined consists of a pure water droplet in air as a host gas. Initially, the droplet is subjected

to a very short, very intense pulse of laser radiation. The optical size of the droplet is assumed to be in the Rayleight limit, thus it absorbs energy uniformly. Because of the very short duration of the pulse, the droplet remains locked in place during the entire heating period. This implies that the droplet heats at constant volume. Additionally, the intensity of the pulse is great enough that the energy absorbed drives the water droplet into a supercritical fluid state. Because of uniform absorption, the motion that evolves will be spherically symmetric, and a one dimensional simulation is sufficient to describe the flow.

Under these conditions the hydrodynamic simulation can be started after the pulse but before the onset of fluid motion, using the very hot, dense fluid as the initial conditions. In practice this situation can be realized with an aerosol droplet whose Mie size parameter is less than about 0.3, and with a pulse length which is much shorter than the time required for an acoustic wave to propagate across the droplet. The conditions required for this type of "vaporization" have been discussed in the literature (Armstrong[110] or Zuev and Zemlyanov[130]).

Heating the droplet at constant volume causes its pressure to increase enormously (as high as 30000 atmospheres for some cases that we have run). The high pressure causes the droplet to expand violently against its host gas. The strong dynamics give rise to shock waves and associated shock heating in some regions, and adiabatic expansion, cooling, and the possibility of nucleation in other regions. We will

consider these possibilities after we discuss the equations which govern the solution.

b. Theory.

The conservation equations for mass, momentum, and energy determine hydrodynamic flows. Written in conservation form, these are (Bird, Stewart, and Lightfoot[111]):

$$\frac{\partial}{\partial t}\rho_i + (\nabla\cdot\rho_i V) = -\nabla\cdot j_i \qquad i = 1,n \tag{B-1-1}$$

$$\frac{\partial}{\partial t}\rho V + (\nabla\cdot\rho VV) = -\nabla P - \nabla\cdot\tau \tag{B-1-2}$$

$$\frac{\partial}{\partial t}\rho E + (\nabla\cdot\rho EV) = -\nabla\cdot PV - \nabla\cdot q_r \tag{B-1-3}$$

$$- \nabla\cdot q_c - \nabla\cdot(\tau\cdot V)$$

where:

ρ_i is the mass density of the i'th component

n is the number of components

ρ is the total mass density

V is the mass average velocity

j_i is the diffusive mass flux of component i with respect to the mass average velocity

τ is the shear stress tensor

P is the fluid pressure

E is the total energy per unit of mass, kinetic plus internal

q_r is the radiative heat flux

q_c is the conductive heat flux

These equations represent a pointwise mass balance for each component, a force balance, and a total energy balance respectively. We have neglected terms containing gravity and are not allowing the possibility of chemical reaction. Both of these can be included when necessary.

Notice that the momentum equation (B-1-2) is nonlinear in velocity. This gives rise to much interesting behavior. In fact, under many flow conditions this nonlinear term dominates the behavior of the solution. We will examine this further shortly.

In the explosive vaporization regime, molecular transport effects such as mass diffusion and heat conduction are small compared to convective transport. Convective transport is driven by gradients in the pressure field. In the droplet/atmosphere system, convection becomes important when the vapor pressure of the evaporating droplet becomes comparable to the pressure of the surrounding gas. Under these conditions, the rate of evaporation becomes greater than the rate at which diffusion can "conduct" mass away from the droplet. As the temperature and therefore the vapor pressure and evaporation rate of the droplet rises, convection becomes an effective mechanism for mass transport away from the droplet. At higher temperatures it becomes the dominant mechanism.

When a system is convection dominated, the conservation equations can be simplified by eliminating the terms associated with

molecular transport. Specifically, the last term on the right hand side of equations (B-1-1) and (B-1-2), and the last two terms on the RHS of equation (B-1-3) are eliminated. Since there is no molecular diffusion, the system of equations for mass conservation (1) can be added to give a single equation giving the total mass density at a point. The resulting equations are called the "inviscid Euler equations." The driving force for these equations is the pressure gradient term in equation (B-1-2).

Current work in the slow vaporization regime incorporates molecular transport effects, but assumes a constant pressure field, thus eliminating convection. The stipulation of slow vaporization validates this assumption. The basis for the two extremes of vaporization in a single aerosol droplet thus becomes evident. One extreme occurs under conditions of constant pressure and is dominated by molecular transport. This arises under low radiation intensities. The other extreme occurs when high intensities cause large pressure gradients, and is dominated by convective transport. There is a large grey area between these two extremes in which both transport mechanisms must be incorporated.

As mentioned earlier, the gradient of the pressure drives the fluid motion through the momentum equation. The extent to which the pressure is reliably predicted for a compound determines how well the hydrodynamic simulation corresponds to observed behavior. With this in mind, we have incorporated an equation of state which reliably predicts the equilibrium properties of liquid, vapor, and supercritical fluid water over a very wide range of temperatures and densities (Kestin et

al.[121] and Hsar et al[120]). This equation of state allows us to account for deviations from ideal gas behavior.

The equation of state is given as Helmholtz free energy (A) as a function of temperature and density. The pressure can be derived from this expression as a partial derivative:

$$A = A(T,\rho) \tag{B-1-4}$$

$$P = \rho^2 \left(\frac{\partial A}{\partial \rho}\right)_T \tag{B-1-5}$$

The equation of state predicts the proper fluid pressure even under conditions of superheating or supercooling. Thus, we can determine if the vapor becomes supersaturated, and its degree of supersaturation. This helps us determine whether condensation is an important mechanism. To do this we have computed nucleation rates at every point in the system as a function of time. Classical nucleation theory yields the following expression for nucleation rate (McGraw and Saunders[122]):

$$J(f_1) = K(f_1) \exp\left[-W(g^*)/kT\right] \tag{B-1-6}$$

The prefactor K incorporates information about the kinetics of the collision process giving rise to nucleation:

$$K(f_1) = (\alpha f_1^2/\rho_1)\left[2\sigma/\pi m_1\right]^{1/2} \tag{B-1-7}$$

The activation energy for the formation of a critical sized cluster is given from thermodynamic considerations by:

$$W(g^*) = \frac{16\pi\sigma^3}{3\left(\rho_1 kT \ln S\right)^2} \tag{B-1-8}$$

where:

f_1 is the concentration of the vapor

g^* is the critical cluster size, the minimum stable size for a liquid particle at (T,P,)

k is the Boltzmann constant

α is an accommodation coefficient or sticking factor

ρ_1 is the molecular number density in the cluster

σ is the surface tension

m_1 is the molecular mass

S is the supersaturation ratio, the ratio of the vapor concentration to that which exists at equilibrium over a flat interface at T

The inviscid Euler equations have been the bane of numerical analysts for decades. The equations are coupled, hyperbolic and nonlinear. The hyperbolic nature of the equations manifests wavelike behavior (or fronts) in the solution. As an equation becomes more hyperbolic in nature, its numerical solution becomes more susceptible to spurious oscillations (Carey[115]) especially in regions of the solution that contain high curvature (Roache[125]). The nonlinear term in Equation (B-1-2) exacerbates the difficulties by generating shock waves which are discontinuities in the solution. A discontinuity has essentially an infinite curvature, giving rise to severe oscillations and ultimately causing most standard numerical methods to fail.

Much research has gone into developing methods that can provide stable and well resolved solutions in the presence of shock waves.

Woodward and Collela[128] provide a very good review and comparison of several state of the art numerical schemes for solving the Euler equations. We have chosen the Flux Corrected Transport (FCT) method devised originally by Boris and Book.[113] Very simply, FCT works as follows: Two solutions to the problem are computed. One is a low order solution which is guaranteed not to blow up under any conditions, but which gives low accuracy. The second sclution is of higher order and gives accurate results, but tends to develop wiggles in highly structured (shocked) regions of flow. The algorithm searches for regions in which the high order solution develops extrema which do not occur in the low order solution, an indication of spurious oscillations. When one of these regions is encountered, the low order solution is used; in other regions the high order solution is used.

For many problems the original FCT algorithm gives very good results. However, because of the extremely dynamic nature of our test problem, the original algorithm does not give acceptably smooth answers. We have incorporated a more stable version of FCT (Book et al.[112]) which gives very nice results. Computing a smooth profile in smooth regions is very important because of the extremely strong dependence of nucleation rate on temperature.

As mentioned earlier, the equation of state requires density and temperature as input. Unfortunately, transport simulations give density and internal energy, but not temperature directly. Thus, one must iterate within the equation of state to find the temperature to

which the internal energy corresponds. This takes a lot of computer time. Instead of iterating, we have formed a large table of pressure as a function of density and internal energy. Due to the complexity of the equation of state, interpolating from the table is much faster than direct evaluation, even if the temperature were known. We have used a shape preserving interpolation method developed by Delbourgo and Gregory[118] to interpolate accurately, and to reduce the number of data points required.

c. Results.

We have computed the solution to our test problem for a number of initial energies and droplet sizes. The hydrodynamic results are given for a droplet initially heated by a laser pulse to 2400 K exploding into an ideal diatomic gas at 300 K and one atmosphere. The nucleation rates that result for droplet initial conditions of 2400 K and 1600 K are also presented.

Figures B-1-1 through B-1-4 show a time series of density, pressure, temperature, and velocity respectively for a one micron droplet initially heated to 2400 K. The spherically symmetric explosion of a hot, dense gas has been well studied because of the interest in explosives. Brode[114] has given a very good description of the structure and behavior of the flow, to which we refer anyone desiring a detailed explanation of the hydrodynamics. Briefly, the system manifests two shock waves. One shock wave exists in the water region and faces toward

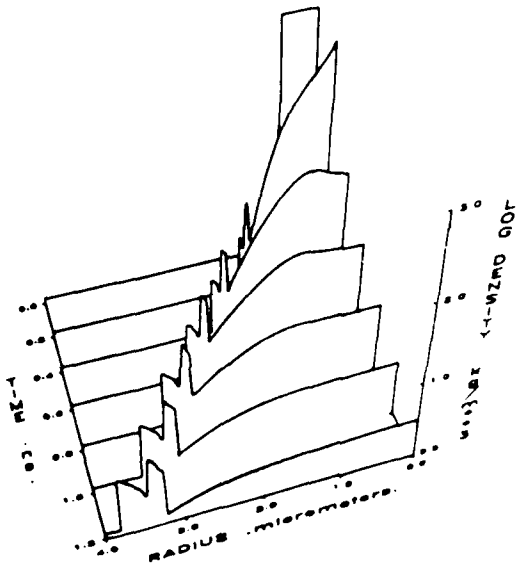

Figure B-1-1. Time series of density versus radius for an initial droplet temperature of 2400 K.

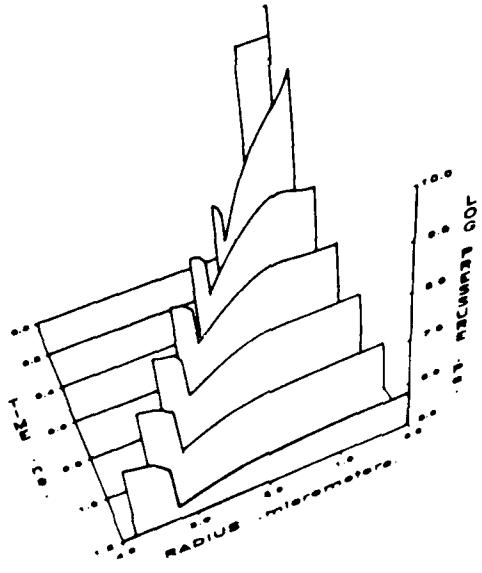

Figure B-1-2. Time series of pressure versus radius for an initial droplet temperature of 2400 K.

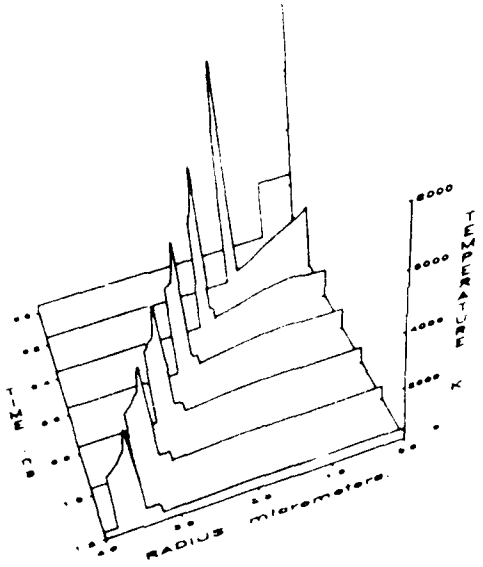

Figure B-1-3. Time series of temperature versus radius for an initial droplet temperature of 2400 K.

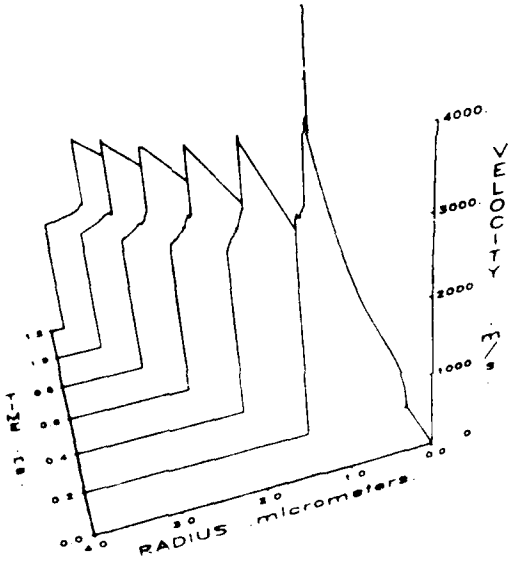

Figure B-1-4. Time series of velocity versus radius for an initial droplet temperature of 2400 K. Note the change in the direction of advancing time.

the origin. The second shock exists in the air and faces away from the origin. The contact discontinuity, which is the remnant of the initial discontinuity, separates the water from the air. The contact discontinuity is characterized by a discontinuous change in density and temperature, and continuous pressure and velocity profiles. Shock waves are discontinuous in all of the flow variables. The region between the water shock and the origin is a region of strong expansion.

Notice the very high temperatures to which the surrounding ideal gas is heated by the passage of the shock. The lowering of the breakdown threshold in air in the presence of fine particles is well known. Steverding[127] has suggested that one of the possible mechanisms for this phenomenon is shock heating of the air. We do not consider breakdown here. However, our results support the possibility of ionization in the shock heated air. Substantial ionization can occur at the high temperatures found in the simulation. Avalanche breakdown could subsequently occur in the presence of intense EMR. It must be remarked, however, that at high fluences, breakdown by ionization processes in the droplet phase may also occur.

The region between the origin and the rear facing (water) shock undergoes extremely strong isentropic expansion before colliding with the rear facing shock. The expansion causes very rapid cooling of the water vapor in the region. As the expansion proceeds, the equation of state begins to predict nonphysical (negative) pressures in this region of the flow. This indicates that the Euler equations are no longer sufficient to describe the physics.

The nonphysical results appear because the water cools to well below the point at which it should condense. The Euler equations make no provision for a phase change in the fluid. Thus, as the expansion proceeds the water vapor becomes more and more supersaturated until the model breaks down.

By acting strangely, the equation of state is saying that all is not well with the simulation. This is the most compelling reason to use a realistic equation of state. Under most conditions, the differences between water vapor and an ideal gas are small, at least not large enough to drastically change the hydrodynamics. However, the difference between condensing water vapor and an ideal gas is very great. Condensation can therefore affect the hydrodynamics (and the electrodynamics) condsiderably. Simulating the physical properties realistically often indicates when and where additional physics becomes important. This behavior might otherwise not be identified and cause incorrect results.

As a first step towards incorporating the effects of condensation on the flow we have computed the nucleation rate in the water vapor as a function of time and space. Figures B-1-5 and B-1-6 show nucleation rates for initial temperatures of 2400 K and 1600 K respectively. The logarithm of the nucleation rate as a function of position is shown for various times.

Comparison of Figure B-1-5 with Figures B-1-1 through B-1-4 shows that nucleation first develops in the region of lowest density and temperature. This is the region that has undergone the greatest amount

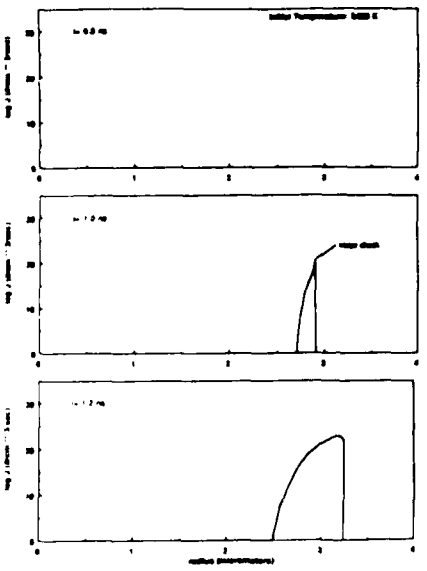

Figure B-1-5. Time series of the logarithm of nucleation rate versus radius for an initial droplet temperature of 2400 K.

of expansion and cooling. As time proceeds, the nucleating regions grow toward the origin. The nucleation rates start out small but grow to very large values as the expansion proceeds and the vapor becomes more supersaturated. The nucleation rates continue to increase because there is no mechanism to relax the high supersaturation. Figure B-1-6 shows that ultimately the supersaturation grows so large that it drives the exponential term in the nucleation rate to one and the rate reaches its maximum possible value (according to classical nucleation theory). This point is nonphysical and under these conditions the equation of state predicts extremely low and sometimes negative pressures. The nonphysical regions can be avoided only by incorporating the nucleation and growth equations. These would allow the vapor to condense and reduce the excessive supersaturation. Note that whereas classical nucleation theory is sufficient to describe when and where nucleation should occur, there

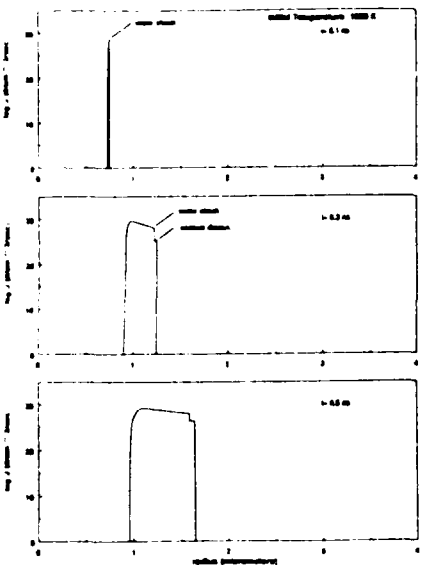

Figure B-1-6. Time series of the logarithm of nucleation rate versus radius for an initial droplet temperature of 1600 K.

is some doubt as to its ability to correctly predict nucleation rates in this problem. Since the flow timescale is so short, the onset of high supersaturation occurs very quickly. Establishing a "detailed balance" between evaporation and condensation rates, a requirement of the classical theory, may not be a realistic assumption in this case.

Strong nucleation occurs after only a brief expansion for all of the initial temperatures considered, from 1600 K through 2800 K. As one might expect, for lower initial temperatures, nucleation becomes important earlier and the system expands less before the simulation becomes nonphysical. It seems that nucleation and particle growth should be considered under almost all conditions of strong convection.

For an initial condition of 2400 K, the nucleation rate drops abruptly from its maximum value in the field to zero when the expanding vapor collides with the shock wave and is reheated. In this region the

particles formed previously will probably be vaporized. For the lower initial temperature (1600 K), the temperature rise at the shock only decreases the value of the nucleation rate, which still remains quite high. This results in the "arm" in the profiles of Figure B-1-6. The nucleation rate goes to zero only at the contact discontinuity.

Chang[116] has reported observing what appear to be jets emanating from single droplets upon intense laser irradiation. The jets originate at hot spots on either side of the droplet, along the axis of the beam, and have a cloudy appearance. The droplet seems to maintain its basic shape and does not appear to be shattering. This observation indicates that the jets may be composed of a hot stream of vaporized material which subsequently condenses to form fine particles. Scattering of light by the particles could explain the cloudy appearance of the jets. Thus, convection dominated hydrodynamics coupled with nucleation and particle growth provide a possible explanation for this phenomenon.

There are several areas that need to be considered to assure that the hydrodynamic simulation is realistic.

As can be seen from Figures B-1-1 through B-1-4, the relevant timescale for large changes in the flow variables is on the order of 0.1 nanosecond. In order that no appreciable motion occurs during absorption of energy, the length of the laser pulse must be on the order of 0.01 nanoseconds for a 1 micron droplet. From the equation of state, the energy required to raise the droplet from ambient conditions to 2400 K is about 6×10^6 J/kg. This implies that the droplet must absorb the energy at a rate of about 6×10^{17} W/kg over the heating period.

Assuming that the optical properties of the water droplet remain constant during the heating period, the intensity required to accomplish the heating (see Armstrong[109] or Pendleton[123]) is on the order of 10^{11} - 10^{12} W/cm^2. The breakdown potential for clean air is on the order of 10^9 W/cm^2. This indicates that in practice, heating a droplet to very high temperatures before substantial motion occurs and in the absence of nonlinear optical effects in either the air or the droplet might be difficult. Nonlinear optical effects may dominate at these power densities.

A strongly absorbing droplet might allow the proper heating rate without such a high power density, but this sidesteps the real problem. To avoid very high power densities, and to extend the range of validity of the simulation, the heating process must be modelled more realistically. Very high power densities can be avoided if the heating process is allowed to occur over a longer period. In general, motion will occur during the heating process, and this will affect subsequent absorption. Even for a droplet that stays in the Rayleigh size limit while expanding, the effect of varying temperature and density on the absorption must be accounted. In addition, since the vaporization process is not even approximately quasi-stationary, the kinetics of the phase change should be considered.

By requiring instantaneous heating of the droplet, the current simulation predicts the most dynamic response possible for a given input energy. Thus, it traces an envelope of limiting behavior. Simulations with a more realistic treatment of heating should fall within the envelope.

Finally, since the relevant timescale for flow is so short, the partitioning of energy amongst the translational, rotational, and vibrational modes of the molecule should be considered. On one hand, the absorption of energy from the laser will cause a departure from equilibrium amongst the various modes. The molecules will move toward an equilibrium state through collisional relaxation. If the time for this relaxation is of the same order as the convective timescale, then the initial nonequilibrium state will affect the hydrodynamics.

Nonequilibrium partitioning of energy can also arise as a result of the expansion. One of the implications of using an equilibrium equation of state is that energy contained in all modes is instantaneously available to drive fluid motion. However, depending on the temperature and density, vibrational relaxation times can be longer than the convective timescale of the expansion. When this occurs, vibrational energy will be available only at a rate determined by collisional relaxation. In order to account for these effects explicitly, the transport equations need to be reformulated in terms of the individual molecular energy modes (see Anderson[108]).

d. Conclusions.

We are modelling the hydrodynamic response of a small water droplet to a very large pulse of laser energy. Our current simulation assumes isotropic absorption and a droplet which is inertially locked in place during the absorption process. Upon heating to very high temperatures, the droplet explodes. We have solved the transport

equations that govern the explosion, incorporating a realistic equation of state for water. The requirement of instantaneous heating manifests the most dynamic response possible for a given input energy. Thus, the current simulation represents a limiting case in the hydrodynamics. In addition, we have computed nucleation rates for the water vapor as it expands.

In the course of the explosion the system manifests two shock waves, one in the water vapor and one in the air. There is also a region of strong expansion and cooling between the water shock and the center of the droplet. This is consistent with previous studies of explosions in curvilinear coordinates.

The air is shock heated to temperatures high enough to cause ionization. If the ionized air is subjected to more radiation, avalanche breakdown of the air can occur. Our simulation substantiates the theory that shock heating of air can be at least partly responsible for aerosol enhanced breakdown.

For all initial droplet temperatures considered (1600-2800 K), strong nucleation occurs in certain regions of the flow after a brief expansion. If condensation of the vapor is not allowed, the solution soon becomes nonphysical. Without using a realistic equation of state, this behavior would likely go unnoticed. Thus, in the explosive vaporization regime, condensation appears to be an important mechanism which should be considered. The presence of fine particles can appreciably affect both the hydrodynamics and the electrodynamics of the system.

Finally, a realistic heating process needs to be included. Heating a water droplet to high temperatures before appreciable motion occurs requires very high power densities. The power densities can be lowered by relaxing the constraint of very little motion during the heating process. However, this requires accounting for the variation of absorption with temperature and density as the motion occurs, still assuming that the "droplet" remains in the Rayleigh size limit during absorption.

We are currently incorporating a realistic heating rate for the droplet. In addition, we are accounting for the possibility of condensation in the flow by including the particle growth equations. These additions will add a new dimension of realism to the simulation, yielding information that can be verified experimentally and providing new insight into the problem.

B-2. Rapid evaporation of droplets in laser beams.

a. Introduction.

There is considerable current interest in the problem of high energy laser beam propagation through an atmosphere containing an absorbing aerosol. When intense electromagnetic radiation interacts with absorbing particles, a variety of diverse phenomena have been noted,[131] including thermal blooming (self steering/defocusing of the beam), and optical breakdown. Each of these effects is due in part to the absorption and consequent comprising the aerosol. Thus we first direct our attention to the single particle absorption problem.

Two extremes of heating may be identified for single particle absorption. For highly intense beams, and/or strongly absorbing droplets, there is the explosive vaporization regime, in which droplet deformation and shattering may occur. This regime is dominated by convective effects, in which pressure gradients are responsible for, and govern, mass transfer from the droplet. At the other extreme, droplet interaction with less intense beams falls into what may be termed the slow evaporation regime. By contrast, this regime is dominated by diffusive effects, in which concentration driving forces determine mass transfer rates from the particle. Carls and Brock[132] have recently studied the case of droplet explosion, shock wave formation, and expansion. Here we study the case of slow evaporation, that is, evaporation in which the droplet temperature never exceeds its boiling point, and in which a constant pressure field is assumed to prevail around the droplet.

Under this restriction of constant pressure, we treat rigorously the time dependent continuum transport equations which describe the hydrodynamics of single droplet evaporation, and develop a computer code, IRIS (Isobaric Radial Droplet Evaporation), for their numerical solution. A slip flow analysis is introduced to account for noncontinuum effects. We compare our solution with a quasi-static approximation to the evaporation process which has been widely used in the past,[134,135,136] and so examine the validity of that approximation. Further, from a unified treatment of the droplet mass and energy

balances, we examine the consequences of various simplifying assumptions that have often been implicit in the past.

b. Theory.

The physical system to be described consists of an isolated spherical droplet (or particle) in an effectively infinite host gas illuminated by laser radiation. The amount of heat an individual droplet absorbs depends on the particle's complex refractive index and its Mie size parameter (the ratio of the particle's circumference to the wavelength of the incident radiation). We have utilized Pendleton's[137] code, PENDSOR, to determine the Mie size parameter below which the droplet heats uniformly. PENDSOR computes a dimensionless heating source function along specified chords of a sphere.[a] For droplet size parameters below 1.0, PENDSOR shows little variation in source function along a diameter. Thus, for incident radiation at 10.6 μm, restriction of the analysis to particles which heat uniformly places an upper limit on particle radius of ~2.0 μm. This restriction makes the problem spherically symmetric. Extension of the model to larger droplets which do not absorb uniformly would require a solution of both the Maxwell equations[138] and the transport equations[139] over the droplet interior.

---

[a] Pendleton defines a dimensionless source function, or normalized power density as:

$$S = |E/E_{inc}|^2$$

where E is a complex representation of the electrical field induced by the laser within the droplet, and E_{inc} is the magnitude of the incident electrical field.[136]

For an incompressible droplet of density ρ_D, and constant heat capacity $C_p \approx C_v$, the general energy conservation equation at any interior point has the form:[139]

$$\rho_D \partial/\partial t(C_{pD}T_L+1/2v^2) + \rho_D \nabla\cdot[(C_pT_L + P/\rho_D + 1/2v^2)\underline{v}] = -\nabla\cdot(\underline{q}+\underline{q}_r \quad (B-2-1)$$

where T_L is the droplet temperature at any point (r,θ,ϕ) within the droplet, and $\underline{v}$ the velocity at that point. The conductive heat flux to the droplet surface, $\underline{q}$, is given by $a -K_D\nabla T_L$, where K_D is the thermal conductivity for the drop. $\underline{q}_r$ accounts for the laser heating source. We consider only a lumped parameter, macroscopic description of droplet behavior in terms of an average droplet temperature T_D. This is achieved by integrating Equation (B-2-1) term by term over the droplet volume, with the definition $T_D = \int_V T_L dV / \int_V dV$, where V is the droplet volume. Utilizing the spherical symmetry of the problem, application of GAuss' divergence theorem yields.

$$Cp_D d/dt\ (4/3\ R^3\rho_D T_D) - 4\pi R^2 K_D(\partial T_L/\partial r)|_R + \pi R^2 Q_{abs} I_0 \quad (B-2-2)$$

where terms representing the internal kinetic energy and the work due to droplet expansion have been neglected. The droplet is irradiated with a uniform beam of intensity I_0, and we account for the laser heating source with a Mie absorption efficiency[138] Q_{abs}. For water droplets below 2 m in radius, Q_{abs} is a linear function of radius.[138] Hence the laser heating term can be written as $4/3\ \pi R^3 \alpha I_0$, where α is a constant, the bulk absorption coefficient.

Consistent with the macroscopic description of droplet behavior, we donot calculate the internal droplet temperature profile to evaluate the surface flux term, $K_D(\partial T_L/\partial r)|_R$. Instead, the term is replaced through the use of an interfacial energy balance. Equating the heat flux from the droplet interior at the surface (conductive only) with that leaving the surface (conductive, kinetic, and convective energy fluxes, and latent heat loss) to the surrounding host gas yields:

$$-4\pi R^2 K_D(\partial T_L/\partial r)|_R = 4\pi R^2\{-K_g(\partial T_g/\partial r)|_R + (\rho v C_{pg} T_g)|_R + 1/2\,\rho_a v_a^3\} - H_{vap}\,dM/dt \qquad (B\text{-}2\text{-}3)$$

where $T_g(t,r)$ is the host gas temperature at any point outside the droplet, K_g is its thermal conductivity, and C_{pg} its heat capacity. ρ is the total mass concentration of the gas, and ρ_a the mass concentration of the vapor. v_a is the radial outward directed velocity of the vapor species, and v the radial mass average velocity of the gas. Substitution of Equation (B-2-3) in Equation (B-2-2) and rearrangement yields:

$$\rho_D C_{pD} 4/3\,\pi R^3 dT_D/dt + 4\pi R^2 \rho_D C_{pD} T_D dR/dt = 4\pi R^2\{K_g(\partial T_g/\partial r)|_R - (\rho v C_{pg} T_g)|_R - 1/2\,\rho_a v_a^3\} + H_{vap}\,dM/dt + 4/3\,\pi R^3 I_0 \qquad (B\text{-}2\text{-}4)$$

Comparison of Equation (B-2-4) with previous analyses[135,136] shows two hitherto neglected terms: one representing bulk convection of energy away from the interface by the moving host gas, $(\rho v C_{pg} T_g|_R)$, and a term which accounts for the droplet radius shrinking with time, $4\pi R^2 \rho_D C_{pD} T_D dR/dt$. We will examine the significance of these terms.

We derive a droplet mass balance taking into account the fact that the surface is shrinking with a velocity dR/dt. Mass flux of the vapor species relative to the moving boundary is given by:

$$1/(4\pi R^2)\ dM/dt = -\rho_a(v_a - dR/dt) \qquad (B\text{-}2\text{-}5)$$

where M(t) is the droplet mass. Noting that $\rho_a v_a$, the total flux relative to a stationary co-ordinate system, is made up of diffusive and convective components,[139] we write:

$$\rho_a \underline{v}_a = -\rho D_{ab} \nabla \omega_a + \omega_a \underline{v} \qquad (B\text{-}2\text{-}6)$$

where ω_a is the mass fraction of the vapor species ($\omega_a = \rho_a/\rho$). Equation (B-2-6) requires a specification of $\underline{v}$ ($\underline{v} = \omega_a \underline{v}_a + \omega_b \underline{v}_b$, where $\underline{v}_b$ is the absolute veolcity of the inert component of the host gas). The inert component is assumed to be insoluble in the droplet, and hence at the interface, $v_b = dR/dt$. The velocity of the water vapor species is specified as $v_a = \dot{m}/4\pi R^2 + dR/dt$, where $\dot{m}$ is the volumetric flowrate of water vapor from the surface. These definitions, with the assumption that the host gas behaves ideally and with $M(t) = (4/3)\pi R^3(t)\rho_D$, lead to:

$$v = dR/dt\ (\rho_D/\rho) \qquad (B\text{-}2\text{-}7)$$

substituting (B-2-6) and (B-2-7) in (B-2-5), and solving for dR/dt:

$$dR/dt = \rho D_{AB} \nabla \omega_a / [\rho_D(1-\omega_a)] \qquad (B\text{-}2\text{-}8)$$

The numerator represents normal Fickian diffusion from a stationary surface. The denominator accounts for mass transfer from the surface by convection, i.e. bulk movement, of the host gas at the surface.

Equations (B-2-4) and (B-2-8) are two ordinary differential equations which, with the initial conditions $T_p(t=0) = T_{p_0}$ and $R(t=0) = R_0$, describe the droplet behavior over its lifetime. However, the energy

conservation Equation (B-2-4) requires a specification of the host gas energy flux, $K_g(\partial T_g/\partial r)|_R$, at the surface, and the mass conservation Equation (B-2-8) requires a mass flux, $\rho D_{AB}\nabla\omega_a$. These fluxes can only be obtained by a simultaneous solution in time of the equations of continuity, energy, and motion, which govern respectively, the concentration, temperature, and velocity profiles in the atmosphere surrounding the drop.

We limit our simulation to the case of an isobaric gas around the droplet, with the argument[140] that any pressure wave in the host gas induced by evaporation at the surface is a transient which propagates at the local speed of sound. Thus, for the time scale in which we are interested, pressure equilibration is complete. In contrast to earlier studies,[135,136,140] the medium surrounding the droplet was not assumed to have a constant density. While the assumption of an incompressible fluid is appealing in that only the isobaric case is considered, temperature variations of up to 30% will cause similar vairations in density. With these restrictions, the transport equations in the host gas surrounding the spherical droplet are well known.[139]

$$(\partial/\partial t)(\rho_a) + \nabla\cdot(\rho_a \underline{v}) = \nabla\cdot(\rho D_{AB}\nabla\omega_a) \qquad \text{(B-2-9)}$$

$$(\partial/\partial t)(T_g) + \underline{v}\cdot\nabla T_g = 1/(\rho C_{pg})\nabla\cdot(K_g\nabla T_g) \qquad \text{(B-2-10)}$$

$$(\partial/\partial t)(\underline{v}) + \nabla\cdot\underline{v}\,\underline{v} = -\nabla(\quad) \qquad \text{(B-2-11)}$$

$$\tau_{rr} = -\mu(2\partial\underline{v}/\partial\underline{r} - 2/3\ \nabla\cdot\underline{v}) \qquad \text{(B-2-12)}$$

With the assumption of a uniformly heated droplet, the fields about the droplet are spherically symmetric. We assume the following temperature dependence for D_{AB} and K_g:[144]

$$D_{AB}(T) = D_{AB0}\ (T/T_0) \qquad \text{(B-2-13)}$$

$$K_g(T) = K_{g0}\ (T/T_0) \qquad \text{(B-2-14)}$$

where the subscript '0' denotes the reference state. Shear stress shown is for the Newtonian fluid, with viscosity, μ. Although the host gas is assumed ideal, the inclusion of a more rigorous equation of state is straightforward. The system (B-2-9) - (B-2-12) is highly coupled and nonlinear, and can only be solved numerically.

For purposes of numerical calculation we consider a spherical water droplet in an initially (t=0) uniformly saturated atmosphere of water vapor in air, stationary relative to the sphere. At t=0 the droplet is exposed to a beam of intensity I_0. The initial conditions for the system are thus:

$$T(r,t=0) = T_{D0};\ v(r,t=0)=0; \quad \rho_a(r,t=0)=\rho_{a0} \qquad \text{(B-2-15)}$$

The interior interfacial boundary conditions in temperature and concentration are given by solution to the ordinary differential equations (B-2-4) and (B-2-8). Departure from continuum behavior is accounted for through the introduction of concentration and temperature jump conditions,[133] appropriate for the slip regime.[133] For exterior interfacial conditions the medium is assumed to be undisturted.

$$T_g(r=R,t) = T_D(t) + C_t\,\lambda_g\,\partial T_g/\partial r|_R \qquad T_g(r\to\infty,t) = T_{D0}$$

$$\rho_a(r=R,t) = \rho_{as}(t) + C_d\,\lambda_g\,\partial\rho_a/\partial r|_R \qquad \rho_a(r\to\infty,t) = \rho_{a0} \qquad \text{(B-2-16)}$$

$$v(r=R,t) = dR/dt\ (\rho_l - \rho_D)/\rho_l \qquad v(r\to\infty,t) = 0$$

C_t and C_d are respectively the temperature and concentration slip coefficients,[133] and λ_g is the mean free path in the host gas.[133] Note that equation (B-2-7) specifies a boundary condition for the [illegible]

motion. Mass concentration at the sphere surface, ρ_{as}, is calculated using Antoine's expression for vapor pressure, with the Kelvin surface curvature correction included.[142]

The system of Equations (B-2-9) through (B-2-16) is highly coupled and nonlinear, but, with the restriction of isobaric evaporation is parabolic in nature. The boundary conditions to Equations (B-2-9) through (B-2-11) are specified by the time integration of Equations (B-2-4) and (B-2-8). The system (B-2-9) through (B-2-11) presents a moving boundary (Stefan-type) problem, since the sphere interface recedes with time. Although the actual radial domain of interest is semi-infinite, the computational doman has been arbitrarily limited to 100 droplet radii. Results from the simulation show the host gas undisturbed at 50 droplet radii and validate this assumption. When solving the transport equations for the host gas we have chosen to ignore the moving boundary problem entirely, since complete disappearance of the droplet constitutes only a 1% change in the computational domain. For each of the partial differential equations (B-2-9) through (B-2-11), a simple implicit finite differencing scheme was used. All coupling terms and nonlinearities have been evaluated explicitly at the previous time step.

. Numerical Results and Discussion.

The calculations have been limited to the case of a pure water droplet irradiated with monochromatic laser light at 10.592 m. Extension of the model to include droplets comprising a nonideal aqueous

solution requires a straightforward modification of the vapor pressure calculation.[136] Table B-2-1 lists the physical property data used.

In this section we first discuss the importance of terms previously neglected in the droplet energy balance. We then examine the effect on the solution of the transport equations of both a temperature dependent diffusion coefficient, and of the temperature and concentration jump boundary conditions. Next we examine how laser energy incident on a particle is distributed in various forms over the particle's lifetime. Finally, the transient solution described is compared with a quasi-steady approximation to the evaporation process. The limitations of this pseudo-steady approach are noted, and we show how its accuracy and applicability may be improved in several ways: through the use of a rigorous energy balance, a temperature dependent diffusion coefficient, and a proper incorporation of the slip flow boundary conditions.

We start by assessing the relative importance of four different effects on droplet heating. These include: (a) accounting for the shrinking droplet radius with the term $4\pi R^2 \rho_D C_{pD} T_D dR/dt$ in (Equation B-2-4); (b) including convective energy losses from the droplet with the term $(\dot{v} C_{pg} T_g)|_R$ in (Equation B-2-4); (c) accounting for the temperature dependence of the diffiusion coefficient with Equation (B-2-17); (d) extending the continuum analysis in an approximate matter to the slip flow regime with the jump boundary conditions, Equation (B-2-16). None of these effects have been accounted in previous analyses.[135,136,143,144] The individual contribution of each of these effects to droplet behavior

Table B-2-1. Physical Constants Used in the Simulation (at 298 K)

Symbol	Value	Units
C_{pd}	4183.	J $kg^{-1}K^{-1}$
C_{pg}	1008.	J $kg^{-1}K^{-1}$
C_d	1.5	dimensionless
C_T	2.3	dimensionless
D_{ABO}	$2.6x10^{-5}$	m^2sec^{-1}
H_{vap}	$2.259x10^6$	J kg^{-1} l
K_{gO}	0.025	$Jm^{-1}sec^{-1}K^{-1}$
ρ_{aO}	0.02265	kg m^{-3}
ρ_D	1000	kg m^{-3}
T_O	298	K
T_{DO}	298	K
A_1	0.019	dimensionless
	$7.87x10^4$	m^{-1}
	1.786	dimensionless
	1.5	dimensionless
g	$6.6x10^{-8}$	m
	$1.8x10^{-5}$	$kgm^{-1}sec^{-1}$

was determined by 'switching off' other terms in the simulation. Figures B-2-1 and B-2-2 compare these effects in the long-term heating behavior of a droplet initially 1 μm in radius. In these figures each of the above effects is compared with a base line (curve A), in which only conductive and latent heat losses from the droplet were considered, and in which diffusion coefficient D_{AB} was held constant, while the slip flow corrections to the boundary conditions were ignored. In Figure B-2-1, which depicts droplet temperature variation with time, and in Figure B-2-2, which shows how droplet radius varies with time, each of the curves shown represents the simultaneous solution of Equations (B-2-4, and (B-2-8) through (B-2-16). Although the droplet temperature-time curves in Figure B-2-1 all vary in their prediction of peak droplet temperature, they are similar in that none show a steady-state droplet temperature. Similar behavior has been reported by Sageev and Seinfeld,[136] and Caledonia and Teare.[140] We have modified the simulation so as to hold the drolet size constant, and observed that droplet temperature increases monotonically with time, asymptotically approaching a steady state at which point heat losses by evaporation, conduction, etc., balance the laser heating source. Thus the nonstationary temperature is due solely to the fact that the droplet is shrinking. This suggests an error in previous analyses which have assumed that droplets rise quickly to a steady temperature, at which they remain while evaporating.[143,144]

Figure B-2-1 makes it clear that failure to account for the rate of change of droplet shrinkage (the term $\rho C_L \frac{dr}{dt} \frac{dT_d}{dr}$ in Eq. (B-2-4)) will result in a significant underprediction of the peak droplet

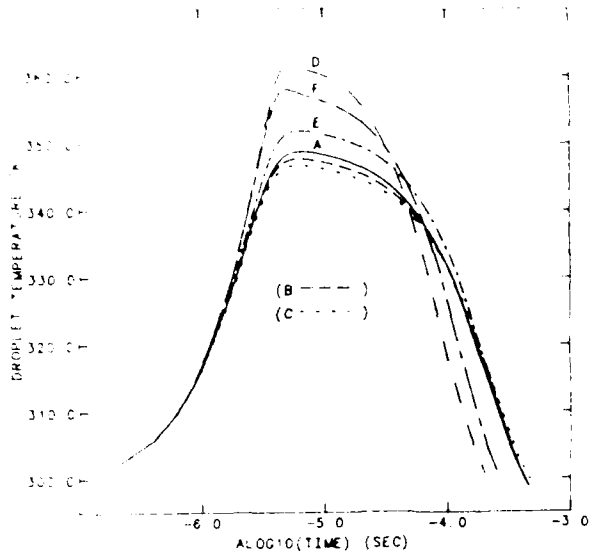

Figure B-2-1. Droplet temperature behavior in response to long time heating for a 1 μm drop. $I_0=10^9$ W/m^2.

(A) Conductive and latent heat losses accounted for
(B) Curve (A) with the temperature dependence of D_{AB} included.
(C) Curve (A) with convective heat loss from drop included.
(D) Curve (A) with droplet mass loss included.
(E) Curve (A) with the incorporation of slip flow boundary conditions.
(F) True solution, i.e. Curve (A) with all above effects included.

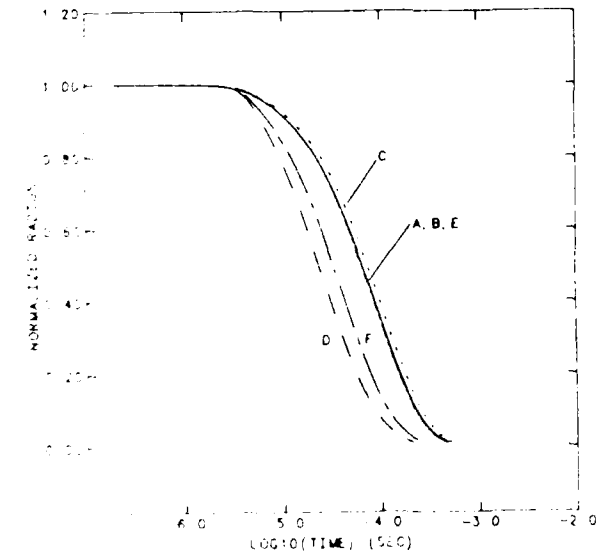

Figure B-2-2. Droplet size behavior in response to long time heating - conditions as in Figure B-2-1. Note that curves (B) and [illegible] indistinguishable from curve (A).

temperature, and a consequent overprediction of its lifetime (Figure B-2-2). In the context of fog 'hole-boring' it may be desirable to stay in the slow evaporation regime while burning through a cloud in order to avoid the shock formation and refractive index changes which might accompany more rapid evaporation and perhaps droplet explosion. These effects may serve to further scatter and attentua'e any ensuing laser beam. Thus, an accurate prediction of droplet peak temperature is essential when one wants to determine the onset of droplet boiling and perhaps explosion, or to study the thermal blooming effects caused by highly nonuniform temperature fields in the atmospheric medium. Although not shown on these plots, kinetic energy losses and accounting for the temperature dependence of K_g have contributed negligibly to the droplet's behavior. Inclusion of convective heat losses (curve C) from the droplet surface has, as might be expected, lowered its peak temperature. Accounting for the temperature dependence of D_{AB} (curve B) similarly lowers the peak droplet temperature. Curve E in Figures B-2-1 and B-2-2 shows the effect of extending the continuum boundary conditions (obtained with $C_t=C_d=0$) to the slip flow regime. The temperature discontinuity at the droplet surface has served to lower the effective driving force for evaporation, hence causing the droplet to rise to a higher peak temperature in order to continue evaporating at the same rate (Figure B-2-2). Figures B-2-1 and B-2-2 make it clear that while the effects of convective energy loss from the droplet, temperature dependent D_{AB}, and slip flow boundary conditions, are of lesser importance than accounting

for the rate of droplet shrinkage, they should all be included when an accurate prediction of droplet behavior is critical.

Next, to further examine how energy is distributed in various forms within the droplet, Equation (B-2-4) is rewritten:

$$E_H + E_{KE} + E_{CV} + E_{CD} + E_{VAP} = E_L + E_R \qquad (B-2-17)$$

in which:

$$E_H = C_{pD}\rho_D 4/3\pi R^3 dT_D/dt \qquad E_{KE} = 1/2A\rho_a v_a^3$$

$$E_{CD} = -AK_g(\partial T_g/\partial r)|_R \qquad E_{CV} = A(\rho v C_{pg} T)|_R$$

$$E_{vap} = -H_{vap} dM/dt \qquad E_L = 4/3\pi R^3 I_0$$

$$E_R = -A\rho_D C_{pD} T_D dR/dt \qquad A = 4\pi R^2$$

Terms on the left hand side of Equation (B-2-17) represent modes in which energy is dissipated in the drop, i.e.: droplet heating, kinetic energy, convective, conductive, and latent heat losses. Terms on the right hand side represent the laser source of heat, and the 'artificial source' due to the shrinking radius. Each term in Equation (B-2-17) is normalized by the right hand side, yielding:

$$Q_H + Q_{KE} + Q_{CD} + Q_{CV} + Q_{VAP} = 1 \qquad (B-2-18)$$

in which $Q_x = E_x/(E_R+E_L)$. This formulation, in terms of the fractional energies, Q_x, provides a convenient means of studying energy distribution in an absorbing droplet. We have deliberately paralleled Armstrong's analysis here in order to allow an immediate comparison with his results.[135] Figures B-2-3 and B-2-4 show these fractional energies for both small drop/low intensity, and large drop/high intensity extremes. Initially the droplet is at equilibrium at the ambient temperature, and hence cannot lose energy by conduction, evaporation, etc.; thus 100% of

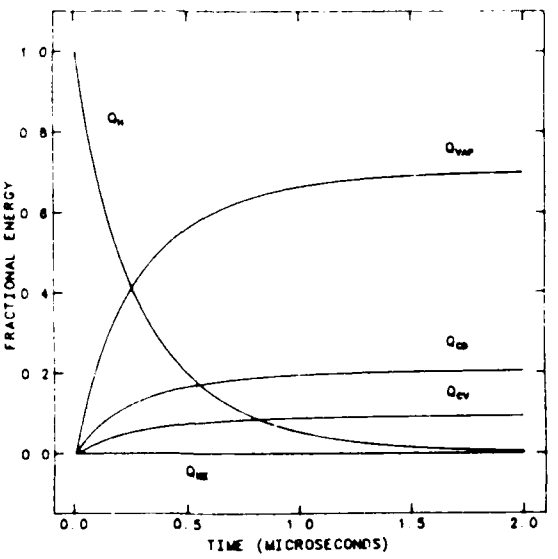

Figure B-2-3. Energy distribution in an absorbing droplet. Initial radius = 0.1 μm, $I_0 = 1.27 \times 10^5$ W/m^2.

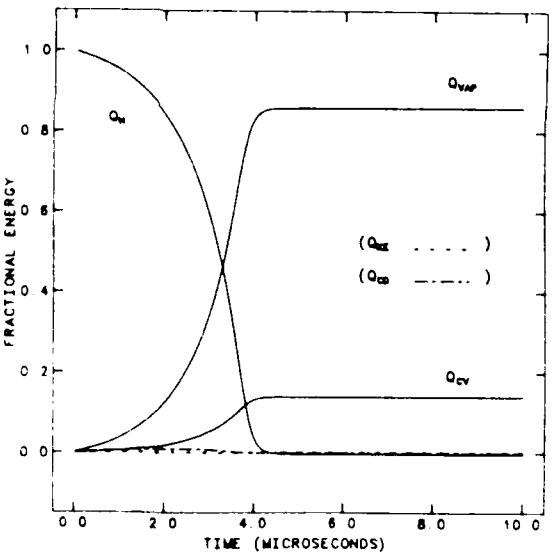

Figure B-2-4. Energy distribution in an absorbing droplet. Initial radius = 2.0 μm, $I_0 = 10^9$ W/m^2.

the source energy goes into droplet heating. As the drop heats it is able to lose energy through the conductive, evaporative, and convective mechanisms discussed, whose rates increase with increasing temperature. Figure B-2-3 shows latent heat losses asymptotically approaching ~70% of the source, conductive losses ~20%, and convective losses ~10%. For this extreme of small droplet/low intensity, similar results have been reported by Armstrong,[135] who shows asymptotic limits of 72% for latent heat losses, and 28% for conduction (convective losses were not accounted for in his analysis). For the opposite extreme of a large drop subjected to an intense beam, Armstrong[135] has predicted that latent heat losses will asymptotically absorb 100% of the source energy, and conduction 0%. However, due to the nature of the approximation used in his solution, Armstrong was unable to verify this result. When we ignore convective losses from the droplet (the term E_{CV} in Equation B-2-17) in our simulation, although not shown we find exactly this behavior. At this extreme, the droplet is evaporating at a sufficiently high rate that conductive heat losses, while still present, are negligibly small compared to latent heat losses. Figure B-2-4 shows this case when the term E_{CV} is included. Latent heat losses asymptotically approach 86%, conductivelosses are insignificant, and convective losses, following the same trend as latent heat losses, approach 14%. As expected, for this case of faster evaporation, convective losses are larger than those shown in Figure B-2-3. These high evaporation losses in comparison to conductive losses occur because vapor pressure, and hence evaporation rate, is an exponential function of temperature, while conductive losses

depend only linearly on temperature. Note that convective losses, unlike conductive losses, do not disappear, since they are due purely to the net efflux of material from the particle. Figures B-2-3 and B-2-4 should not be construed as implying that droplet temperature asymptotically approaches a steady state (since Q_H, the fractional energy used in droplet heating, approaches zero). They give this appearance only because the time scales shown represent such a small portion of the life of the drop. However these figures do lend credence to the assumption of a quasi-steady state droplet temperature for heating times very short compared with the droplet lifetime. Such a situation develops when the drop is exposed to a pulsed laser source.[135,136]

Finally, we compare our transient model of droplet evaporation with a quasi-steady approximation to the process which has been used by several previous investigators.[134,135,136] This approximate analysis makes a great simplification in the model development by assuming a pseudo-steady state approximation to the transport equations (B-2-9) through (B-2-11) in which the explicit time derivatives are ignored. This approach[136] argues that the characteristic relaxation times for changes in gas phase temperature and concentration profiles are far smaller than for changes in the droplet temperature.[b] Equations (B-2-9) and (B-2-10) thus reduce to two second order ordinary differential

---

[b] This is easily verified for the air water system, and laser heating times of the order of 1 sec. It is, however, easy to imagine a situation (e.g., for a short laser pulse (<< 1 sec) or for the case in which thermal diffusivities of particle and hose gas are ~ equal) in which it may not be a valid assumption.

equations. Williams[134] discusses this approach in some detail and shows that, with the further assumption of an incompressible atmosphere, with constant binary diffusion coefficient D_{AB} and a thermal conductivity K_g, a straightforward analytical integration gives radial profiles for mass fraction ω_a and host gas temperature T_g, and obviates numerical solution of the system (B-2-9) through (B-2-16). We have generalized Williams approach[134] somewhat by integrating the steady-state form of equations (B-2-9) and (B-2-10), with the temperature and concentration jump boundary conditions of Equation (B-2-16). Differentiating these quasi-steady profiles yields fluxes of mass and energy:

$$\rho D_{AB} \partial \omega_a / \partial r|_R = dM/dt \, (\omega_{a\infty} - \omega_a)/(4\pi R^2)/\{EXP[dM/dt/(4\pi R \rho D_{AB})]-F\} \quad (B-2-21)$$

$$K_g \partial T_g / \partial r|_R = dM/dt (T_{g0}-T_{g\infty}) C_{pg}/(4\pi R^2)/\{EXP[C_{pg} dM/dt/(4\pi R K_g)]-G\} \quad (B-2-22)$$

The subscripts '0' and '∞' represent quantities at the sphere surface and at infinity respectively. The quantities F and G can be viewed as correction factors for the slip flow regime:

$$F = 1 - C_d \rho_g dM/dt \, / \, (4\pi R^2 \rho_{AB})$$

$$G = 1 - C_t \rho_g C_{pg} dM/dt \, / \, (4\pi R^2 K_g)$$

Clearly, for the continuum case, F=G=1, and equations (B-2-21) and (F-2-22) reduce to those originally presented by Williams.[134] Previous investigators[135,136] have substituted the continuum forms of the flux expressions (B-2-21 and B-2-22) into the droplet energy and mass balances Equations (B-2-4) and (B-2-8). Substitution of expression (B-2-22) in (B-2-8) and rearrangement yields the following quasi-steady expression for the mass balance.

$$dM/dt = -4\pi R \rho D_{AB} \ln [(F + (1-F)\omega_{a0} - \omega_{a\infty})/(1-\omega_{a0})] \quad (B-2-23)$$

Note that if the continuum restriction is made then F=1, and Equation (B-2-23) is identical to that used by both Sageev and Seinfeld[136] and Armstrong.[135] In this pseudo-steady approach the ordinary differential euqations (B-2-4) with (B-2-21), and (B-2-23) provide a complete description of droplet behavior. With the restriction to continuum behavior and some further simplifying assumptions, Armstrong[135] has achieved an analytical solution of the system (B-2-4), (B-2-21), and (B-2-23), which is valid for short heating times during which the droplet may be assumed to move quickly to a steady pool temperature. Sageev and Seinfeld[136] have extended this to droplets comprised of aqueous solutions. Computationally, solution of the pair (B-2-21) and (B-2-22) is straightforward. It should be noted that the correction factor F is defined in terms of the evaporation rate dM/dt. However, this poses no problem in the numerical solution of the pair (B-2-4) and (B-2-23). Equation (B-2-23) is solved iteratively at each time step for the evaporation rate dM/dt.

In Figures B-2-5 and B-2-6 the solutions to equations (B-2-4), (B-2-21), and (B-2-23) are compared with our transient solution (Equations (B-2-4) and (B-2-8) through (B-2-16)), for a 1 μm droplet irradiated with light of intensity 10^9 W/m^2.

Previous investigators[134,135,140] have used an energy balance similar to Equation (B-2-4), but neglected the terms E_{CV}, and E_P. Thus, in order to allow a direct comparison with their work, in curve (B) we have held F=G=1, and ignored the terms representing convective energy loss, E_{CV}, and droplet shrinkage, E_P, and furthermore, held diff[illegible]

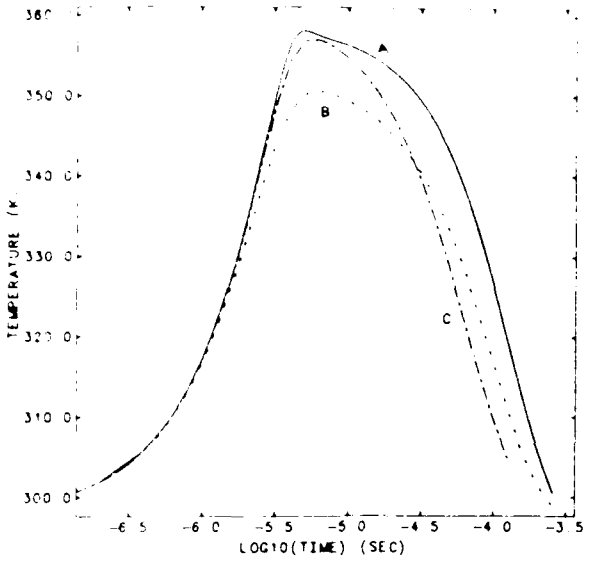

Figure B-2-5. Droplet temperature comparison of pseudo-steady state solution and full transient solution for long-time droplet heating. Conditions as in Figure B-2-1
A - Rigorous transient solution
B - pseudo steady solution of previous investigators
C - pseudo steady solution using rigorous energy balance, temperature dependent D_{AB} and slip flow boundary conditions.

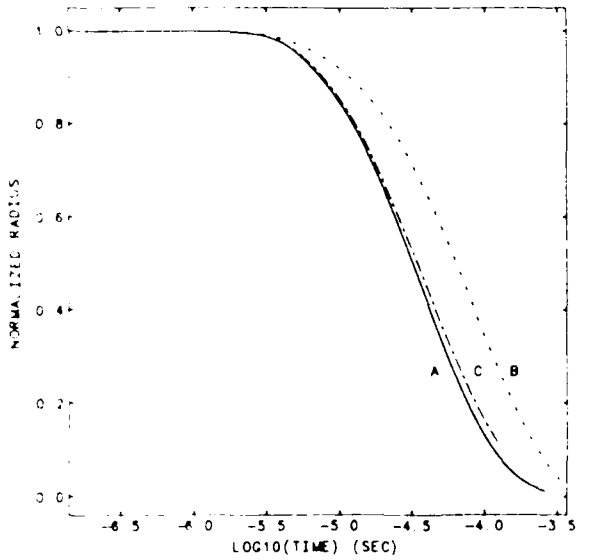

Figure B-2-6. Droplet size comparison of pseudo-steady state solution and full transient solution for long-time droplet heating. Same as Figure B-2-5.

coefficient constant. This form of the pseudo-steady solution provides a poor prediction of droplet peak temperature, and we immediately suspect this to be caused by the difference in energy balances used, more than by the nature of the quasi-steady assumption. Inclusion of slip boundary conditions (F,G≠1), the rigorous energy balance, and a temperature dependent diffusion coefficent, provides an improved prediction of droplet behavior. Although each effect has not been singled out explicitly as in Figure B-2-1, their relative magnitudes are similar to those already shown. While the temperature profiles (Figure B-2-5) are still in slight disagreement, the radial profiles agree closely (Figure B-2-6). When studying atmospheric extinction of electromagnetic radiation, the size of the absorbing particle is of greater importance than its temperature (in the absence of thermal blooming effects). Figure B-2-6 shows that the quasi-steady assumption may be made to provide an adequate description of droplet shrinkage only if the rigorous energy balance Equation (B-2-4) is used. Greater accuracy can be achieved by further use of a temperature dependent diffusion coefficient, and the slip flow correction factors F and G.

Figure B-2-7 shows droplet response to a pulsed laser source. Here various sized droplets have been irradiated with a 5 microsecond pulse of 10^9 W/m^2. It can be seen that the smaller drops attain a quasi-steady temperature during passage of the pulse. Also shown for comparison are results obtained using the quasi-steady analysis and neglecting the effects discussed above. As shown by Figure B-2-7, neglect of these effects results in an erroneous prediction of droplet

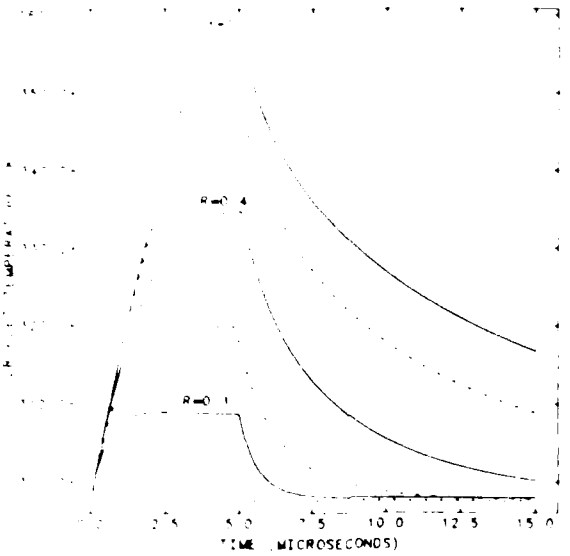

Figure B-2-7. Droplet temperature response to a pulsed laser source. Pulse length = 5 seconds, $I_0 = 10^9$ W/m^2, initial radius indicated is in m.
A - full transient solution
B - pseudo-steady state solution of previous investigators.

peak temperature, even for the case of heating times very short in comparison to the droplet's lifetime.

d. Conclusions.

We have made a rigorous theoretical development of the equations which describe the continuum evaporation of a single droplet suspended in an inert host gas, and extended this approximately to the noncontinuum regime through a slip flow analysis.[133] A computer code (RIDE) for numerical solution of the system has been developed and utilized to compare this rigorous development with a simplified analysis which uses a pseudo-steady approximation to the hydrodynamic equations governing droplet evaporation. This pseudo-steady approximation allows a

straightforward analytical spatial integration of the transport equations, and has been commonly used in the past. Its solution is also attractive in that it affords a reduction of several orders of magnitude in the computational time required to characterize a droplet's behavior over its lifetime. However, the pseudo-steady solution can be made to agree approximately with the full transient solution only if a rigorous form of the droplet energy balance is used, as done here. The most important feature of this rigorous balance is that it accounts for the rate of change of droplet radius. Significant differences in prediction of peak droplet temperature result from neglect of the droplet shrinkage term. A further, although less important improvement in the prediction using the pseudo steady approximation can be achieved if a temperature dependent diffusion coefficient is used, and if the appropriate jump boundary conditions in temperature and concentration are included.

For the case of a water droplet irradiated with a 10.6 m laser light of pulse length greater than the order of a microsecond, we have satisfied ourselves that the pseudo-steady solution developed here can be made to give an adequate qualitative description of droplet behavior. We are using the pseudo-steady solution to model the laser-forced evaporation of a polydispersed aerosol distribution. This involves both an approximate, moment method,[146] and a high accuracy finite element code developed by Tsang and Brock.[142] In this context, the computational speed of the pseudo-steady solution is especially important. We will elaborate on our results in a later publication. With this polydispersed

model complete, a straightforward extension allows one to tackle the laser hole-boring problem, modeling the propagation of an electromagnetic beam through a polydispersed aerosol cloud, a problem which up to now appears to have been solved for the limiting case of a mono-dispersed aerosol.

AD-A184 467 PLUME MECHANICS AND AEROSOL GROWTH PROCESSES(U) TEXAS UNIV AT AUSTIN AEROSOL RESEARCH LAB J R BROCK JUL 87 CRDEC-CR-87084 DAAK11-83-K-0006 3/3

UNCLASSIFIED F/G 19/1 NL

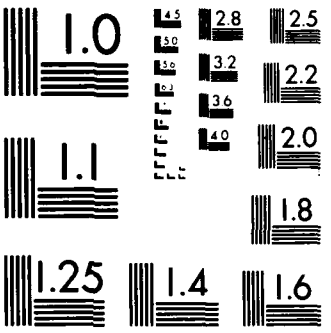

MICROCOPY RESOLUTION TEST CHART
NATIONAL BUREAU OF STANDARDS-1963-A

C. AEROSOL FILTRATION

We have only recently started work on aerosol filtration. Two types of filters have been studied theoretically. The fibrous filter and the membrane filter. Here only the work on membrane filtration is discussed.

1. Membrane Filters.

a. Introduction.

For aerosol filtration, fibrous filters have played a dominant role and so have received most attention. By contrast, membrane filters, although widely used, have not been studied extensively. The structure of membrane filters exerts a somewhat limiting influence on their applicability, but they are still used widely and they are useful especially in the analysis of aerosols[147] due to their own characteristic advantages such as a nearly absolute efficiency, light and non-hygropscopic character, capture of particles mostly on the surface or in the thin surface layer, slow clogging of its pores, wide thermal range, resistance against acids, bases and certain solvents,[147] to name a few. In comparison with fibrous filters, membrane filters have been studied theoretically very little since they have complex structure and filtration mechanisms which don't permit simplifying assumptions. Therefore, exact theoretical analysis requires numerical analysis.

In recent times, the finite element method has been widely used to solve fluid dynamics problems. It can handle problems with non-

regular geometries more easily than finite difference methods. In this study, a finite element method based on Galerkin discretization was used to investigate the membrane filtration problem.

b. Mathematical Formulation and a Finite Element Scheme.

The mathematical description of steady fluid motion for the membrane filter problem is assumed to be given by the following equations:

(continuity equation)

$$\nabla \cdot \underline{V} = 0 \qquad \text{(C-1-1)}$$

(momentum equation)

$$\rho \underline{V} \cdot \nabla \underline{V} = \rho \underline{f} + \text{div } \overline{\overline{\sigma}} = -\nabla p + \rho \underline{f} + \nabla \cdot \overline{\overline{\tau}} \qquad \text{(C-1-2)}$$

Here the fluid is assumed to be incompressible and Newtonian. In these equations, $\underline{V}$ represents the fluid velocity, ρ the density, $\underline{f}$ the body force vector per unit mass, $\overline{\overline{\tau}}$ deviatoric stress tensor, $\overline{\overline{\sigma}}$ total stress tensor, p pressure. For the constitutive equation a Newtonian fluid was assumed. Then

$$\overline{\overline{\tau}} = 2\overline{\eta}\ \overline{\overline{D}} \qquad \text{(C-1-3)}$$

where D is rate of strain tensor. In the analysis, we also need the diffusion equation for aerosol concentration,

$$\underline{v} \cdot \nabla C_A = D_A \nabla^2 C_A + R_A \qquad \text{(C-1-4)}$$

where C_A is a concentration of aerosol, D_A is the diffusivity of aerosol in the fluid, R_A is the rate of formation of aerosols per unit volume of the fluid. With suitable boundary conditions, these four equations form the basis for analysis by the finite element method used in this study.

Using the variational statement for these equations implicitly included with finite element interpolation for the independent variables, $\underline{v}$, p and C yields the standard finite element equations. Since the finite element scheme used in this study has been fully described elsewhere,[148] the derivation is not given here; we only mention briefly the main features of this scheme. Basically the finite element method code used is designed for steady state, incompressible, two dimensional (plane or axisymmetric without torsion) problems. It is based on the Galerkin discretization procedure, solving simultaneously equations (C-1-1) to (C-1-4) in their full nonlinear forms. To handle the nonlinear terms, iteration is done until convergence occurs.[148] The computer program has been amply tested for correct simulations.

c. Diffusion of Aerosols in Laminar Flow in a Cylindrical Tube.

Before solving the membrane filtration problem, the problem of mass transfer of aerosols with axial diffusion in laminar flow through a cylindrical tube was solved first since its analytical solution as a series of Bessel functions is already known.[149] This provides a test of our numerical procedures.

When small particles are suspended in a fluid flowing through a channel, the random Brownian diffusion of the particles may bring them into contact with the channel walls where they are absorbed and normally lose any electric charge they carry. The steady state mass diffusion equation governing the concentration of particles C_A within a fluid moving in a circular pipe is given by the diffusion equation (C-1-4).

Cylindrical coordinates (r,z) with the axis of the tube at r=0 are used for this problem.

Many authors have studied this problem under varying assumptions, e.g., Tan and Hsu, [149,150] Ingham,[151,152] Gormley and Kennedy,[153], Davies.[154,155] Some of them solved this problem under the assumption of a fully developed or a flat axial velocity profile at tube entry and some neglected axial diffusion (This can be a valid assumption provided the Peclet number is larger than 100. However for Pe $\leq$ 100, the effect of axial diffusion is still significant near the channel entrance[150]). The entrance effect in a short tube was considered by Ingham[152] with no axial diffusion.

In this study we will solve full diffusion equation, making none of these previous assumptions. With $R_A = 0$, equation (C-1-4) can be written as

$$v_z \frac{\partial C_A}{\partial z} + v_r \frac{\partial C_A}{\partial r} + D_A \frac{\partial (r\, C_A)}{r \partial r\, \partial r} + \frac{\partial^2 C_A}{\partial z^2} \qquad \text{(C-1-5)}$$

with the following boundary conditions imposed on this equation

$$C_A(0,r) = C_0$$

$$C_A(\ ,r) = 0$$

$$\frac{\partial C_A}{\partial r}(z,0) = 0 \qquad \text{(C-1-6)}$$

$$C_A(z,R) = 0$$

The first boundary condition is the assumption of uniform concentration of particles at the tube inlet and the second represents decay of concentration to zero for very long tubes, the third one is the

axisymmetric condition at the center of the tube and the fourth is the condition of perfect absorption at the tube wall. The initial velocity profile was assumed that for Poiseuille flow $v_z/v_0 = 2\ (1-r^2/R^2)$, where R is tube radius. The schematic diagram of this problem is shown in Figure C-1-1.

The solution of this problem can be found following Tan and Hsu[149] and defining a parameter F_μ as the function of aerosols arriving at a distance z,

$$F_\mu = \frac{\int_0^R v_z C_A 2\pi r\, dr}{\pi R^2 C_0 v_0} \qquad (C-1-7)$$

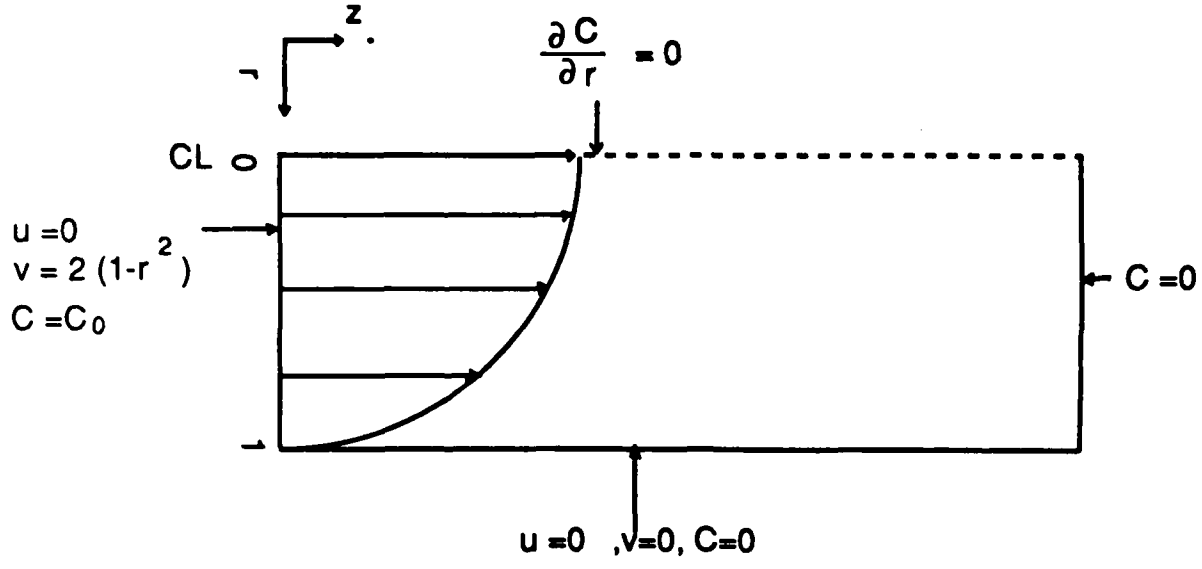

Figure C-1-1. Geometry of diffusion inside tube.

(where $\mu = D_A z/v_0 R^2 = 2z/RPe$)

The following solution was derived by Tan and Hsu[149]

$$F_\mu = -4 \sum_{n=1}^{\infty} D_n \{R_n'(1) + \beta_n^2 \int_0^1 \eta R_n d\eta\} \exp(-\beta_n^2) \qquad (C-1-8)$$

where R_n is the eigen function of

$$R_n'' + R_n'/\eta + \beta_n^2 [(1-\eta^2) + (\beta_n^2/Pe^2)]R_n = 0 \qquad (C-1-9)$$

with $R_n'(0)=0$ and $R_n(1)=0$, β_n is the eigenvalue of equation (C-1-5), $\xi = \mu/2$, $\eta = r/R$ and $Pe=2Rv_0/D_A$. The values of F_μ were tabulated by Tan and Hsu[150] for Pe=1,10,100.

To solve this problem by a finite element method, a total of 120 elements (6x20) was used. Calculated values of F_μ are tabulated for Pe=1,10,100 in Tables C-1-1, C-1-2, and C-1-3 and Tan and Hsu's result is also presented for comparison. Generally the agreement is very good. The differences between the FEM solution and those of Tan and Hsu's are less than 0.5%. The integration of equation (C-1-7) was done using

Table C-1-1. Values of F_μ for Diffusion of Aerosols in a Tube When Pe = 1

	F_μ by FEM	F_μ by Tan and Hsu
0	0.995649	1.
0.005	0.984864	0.9885
0.01	0.974130	0.9773
0.02	0.952884	0.9553
0.05	0.891686	0.8928
0.1	0.798612	0.7991
0.2	0.642655	0.6431
0.3	0.519083	0.5196
0.4	0.420359	0.4210
0.5	0.341043	0.3416

Table C-1-2. Values of F_μ for Diffusion of Aerosols in a Tube When Pe = 10

	F_μ by FEM	F_μ by Tan and Hsu
0	0.995649	1.
0.005	0.990372	0.994
0.01	0.995085	0.994
0.02	0.974554	0.977
0.05	0.944011	0.9542
0.1	0.897130	0.8975
0.2	0.81616	0.8166
0.3	0.748123	0.7488
0.4	0.689215	0.6901
0.5	0.63723	0.6382
1.	0.442648	0.444
2.	0.222972	0.224
3.	0.113101	0.114
4.	0.057516	0.058
5.	0.029256	0.0295

Table C-1-3. Values of F_μ for Diffusion of Aerosols in a Tube When Pe = 100

	F_μ by FEM	F_μ by Tan and Hsu
0	0.995649	1.
0.01	0.99258	0.9955
0.02	0.989477	0.992
0.05	0.980677	0.9824
0.1	0.967846	0.9689
0.2	0.946274	0.947
0.3	0.928518	0.929
0.4	0.912596	0.9132
0.5	0.898638	0.8989
1.	0.840628	0.8406
2.	0.754646	0.7545
3.	0.688676	0.6872
4.	0.632621	0.6305
5.	0.584127	0.581
10.	0.396452	0.3968

Simpson's rule in the FEM calculation, due to the coarse grid in a row a small error can arise. When $\mu=0$, F_μ should be 1, but the FEM solution shows small deviations from this. If we use more elements in a row, better results are obtained but at increased computation cost. The small difference can be reduced, so we have shown that the FEM solution is accurate enough to be accepted. From these tables we can see also that decreasing Pe increases F_μ since a decrease of Peclet number means physically an enhancement of axial diffusion over radial diffusion, reducing the loss of particles to the tube walls and increasing F_μ values.

d. The Computational Results of Membrane Filtration and Discussion.

With assurance to the accuracy of the present code, membrane filtration was investigated next. Since there are so many pores on the surface of membrane filters, it is impossible to include all the pores in the simulation. Instead, we do the calculations using a single pore model, a procedure analogous to that used in the fibrous filter problem.

Consider the membrane filtration process as occurring in a single pore membrane as shown in Figure C-1-2. Dimensionless variables are used:

$r^* = r/R$, $\quad z^*=z/R$

$C^*=C_A/C_0$ $\quad v^*=v/v_0$

$u^*=u/v_0$ $\quad D_A^*=D_A/2Rv_0$

where R is the reference length, v_0 is reference velocity.

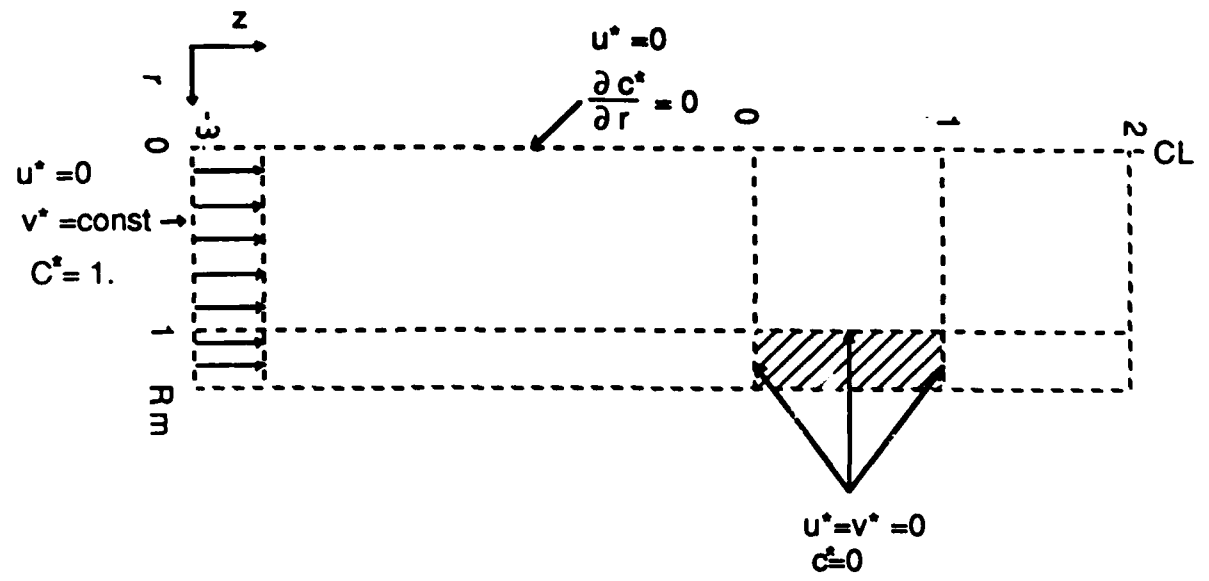

Figure C-1-2. Geometry for membrane filter.
r_1Z: radial coordinates; u*, v* radial and axial velocities;
C: concentration; R_m: outer radius of pore.

The following boundary conditions are used:

$v^* = 1$, $u^* = 0$, $C^* = 1$ at far upstream ($z^* = z_{min}$)

$u^* = v^* = 0$, $C^* = 0$ at pore wall and membrane surface

$u^* = 0$ and $\partial C^*/\partial r^* = 0$ at pore center line. (C-1-10)

The far upstream position was taken as 3 times the pore radius. The pore radius was set as follows. If A is the area of the whole filter, L the thickness, A_p the area of one pore and N_p the number of pores per unit surface area, then the volume of the pores V_p is

$$V_p = A_p N_p LA \qquad (C-1-11)$$

Since the volume of the filter V_f is $V_f = AL$, the porosity $\varepsilon = V_p/V_f$, then equation (C-1-11) yields

$$\varepsilon = A_p N_p \qquad (C-1-12)$$

The porosity can be expressed as a function of pore diameter D_p and the axial distance between pores d from simple geometrical considerations[147]

$$\varepsilon = \pi D_p^2/(2\sqrt{3}d^2) \qquad (C-1-13)$$

The porosity reaches the maximum value for $d=D_p$, i.e., $\varepsilon=90.64\%$. The porosity of membrane filters is accordingly much lower than the porosity of fibrous filters. In the limit of a single pore membrane, the porosity is $\varepsilon=1/R_m^2$, so from equations (C-1-12) and (C-1-13)

$$R_m = \{\pi D_p^2/(2/3d^2)\}^{0.5} \qquad \text{(C-1-14)}$$

Hence minimum R_m reaches almost 1.05 when the membrane has the maximum porosity.

In this study, four different values of R_m were taken: 1.05, 1.1, 1.2, 1.3 respectively, and accordingly the porosity was 90.7%, 82.64%, 69.44%, 59.17%. In this study two different mechanisms of membrane filtration were investigated: diffusional deposition inside the pore and inertial deposition on the filter surface. For diffusion inside the pore, the efficiency was defined as

$$E_d = 1 - C_f^*/C_i^* \qquad \text{(C-1-15)}$$

where C_i^* is the concentration at pore inlet, C_f^* is the concentration at the pore outlet. For inertial deposition, particle trajectories were calculated based on the equation of particle motion following Stoke's law

$$\text{Stk}\,\frac{du_p^*}{dt} + U_f^* - u_p^*$$

$$\text{Stk}\,\frac{dv_p^*}{dt} + V_f^* - v_p^* \qquad \text{(C-1-16)}$$

where Stk is Stokes number defined as

$$\text{Stk} = mv_0/3\pi\eta_0 d_p R \qquad \text{(C-1-17)}$$

In the above equations, U_f^* and V_f^* are the radial and axial fluid velocities, u_p and v_p are radial and axial particle velocities, d_p is the

particle diameter, η_0 is the fluid viscosity, and m is the mass per unit particle. Since particle movement does affect fluid momentum, equation (C-1-16) is solved using the Runge-Kutta-Fehlberg method with velocity fields generated from the FEM solution. Far upstream, particles were assumed to have the same velocities as that of the fluid.

Inertial deposition efficiency was defined as follows

$$E_1 = (R_2^2 - R_1^2)/R_m^2 \qquad (C-1-18)$$

where R_2 is the starting radial position of a particle far up stream which hits the membrane skirt ($r^*=R_m$) and R_1 is the starting radial position of a particle far upstream which hits the pore skirt ($r^*=1$).

Figure C-1-3 shows a fluid stream line and Figure C-1-4 shows typical particle trajectories. Figure C-1-5 shows the axial velocity profiles at some positions. We can see that at the pore inlet the axial velocity is neither fully developed nor in plug flow. However the flow develops very fast, so that except for very short pores (very thin membranes) the general assumption of a fully developed velocity profile seems to be reasonable. Table C-1-4 shows the variation of diffusion efficiency and inertial efficiency with different porosity membranes. As the porosity decreases, the inertial deposition increases due to increased membrane surface area and the initial concentration at pore inlet decreases due to reduced porosity. The diffusion efficiency increases slightly owing to decreased inlet axial velocity (slow convection), but due to decreased initial concentration the total deposition by diffusion decreases. In this computation when exact collision at pore inlet and outer membrane skirt did not occur,

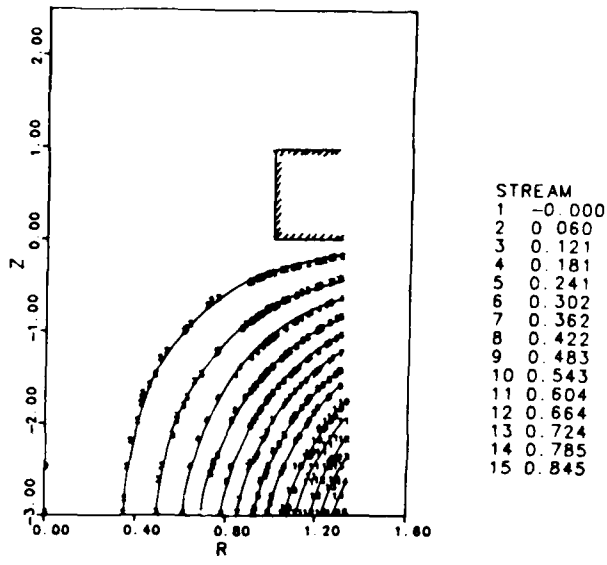

Figure C-1-3. Streamlines near membrane filter surface when $v^*=1$, $R_m=1.3$.

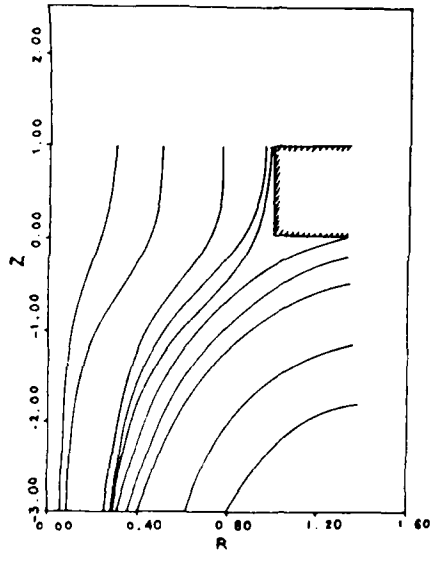

Figure C-1-4. Particle trajectories when $P_e=1$, $R_m=1.3$, Stk=0.2.

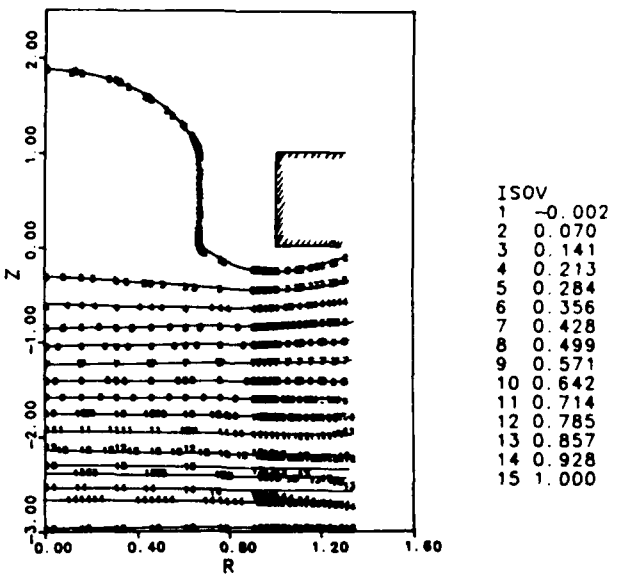

Figure C-1-5. Iso-axial velocity profiles, R_m=1.3.

interpolation was done to get the inertial deposition efficiency. This can introduce a very slight error in the calculation of inertial deposition, but it is at least qualitatively correct. Another fact to be mentioned is that the particle which moves into the pore does not deposit on the pore wall, due to the laminar flow of the fluid inside the pore. This is confirmed by particle trajectory calculations; the particle which enters the pore just passes out the pore.

The computational result in Table C-1-4 is for Pe=1. Peclet number was varied to determine the concentration change. The result is summarized in Table C-1-5. Increasing Pe increases convection. However due to increased axial diffusion, the diffusion efficiency was reduced. The total diffused concentration at the wall is also presented in Table C-1-5. Increasing Pe raises the diffused concentration but when Pe goes over 100 it drops. This means that axial diffusion is very important for diffusion in the pore when the fluid moves slowly or diffusivity of the

Table C-1-4. Summarized Result of Membrane Filtration When

$v^*=1$, Pe=1, Stk=0.2

R_m	Diffusion Deposition	Inertial Deposition	Initial Concentration at pore inlet C_i
1.05	0.88683	5.425E-5	0.007113
1.1	0.89061	8.144E-5	0.006582
1.2	0.89486	7.258E-4	0.006096
1.3	0.89709	2.0732E-4	0.005908

Table C-1-5. Concentration Change with Pe When

$v^*=1$, $R_m=1.2$, Stk=0.2

Pe	F_μ at pore inlet	F_μ at pore inlet	$E_{diffusion}$	Diffused Amount
0.1	0.00276	0.000284	0.8973	0.00248
1.	0.00610	0.000640	0.8949	0.00546
10.	0.00976	0.001232	0.8738	0.00853
100.	0.03922	0.014437	0.6319	0.02478
1000.	0.05949	0.048000	0.1931	0.01150
10000.	0.06209	0.059038	0.0492	0.00305

particles is very large. Figures C-1-6 through C-1-8 show iso-concentration profiles when Pe=1,10,100 respectively. These figures show that, as already mentioned, high Pe causes high concentrations at the pore inlet ($z^*=0$); the higher Pe is, the steeper the concentration gradient is near the pore wall.

Up to this point, we have just looked at the problem with the initial velocity $v^*=1$. Next the initial velocity far upstream was varied as 3,5,10, so that the Peclet number was also changed 3,5,10. The result is shown in Table C-1-6. As previously seen, increasing Pe decreases the diffusion efficiency. When the initial axial velocity is 10, inertial deposition rises very sharply, while the concentration at pore inlet changes remarkably due to the large convection.

In the calculation of particle trajectories, the particle size was assumed to be uniform. For different sizes of particles, the diffusivity and Stokes number change. The Stokes number is proportional to the square of particle diameter while diffusivity decreases inversely with particle diameter.[156] To examine the selective characteristics, which can be defined as an efficiency dependence of the filter on the particle size, particle size was changed and accordingly the Stokes number and diffusivity were changed. The computational results are presented in Table C-1-7. As expected, the diffusion efficiency decreases due to increased Pe and inertial efficiency increases. Total efficiency increases slightly with increasing particle size. From this limited calculation, it is not quite clear if the effect of decreasing of

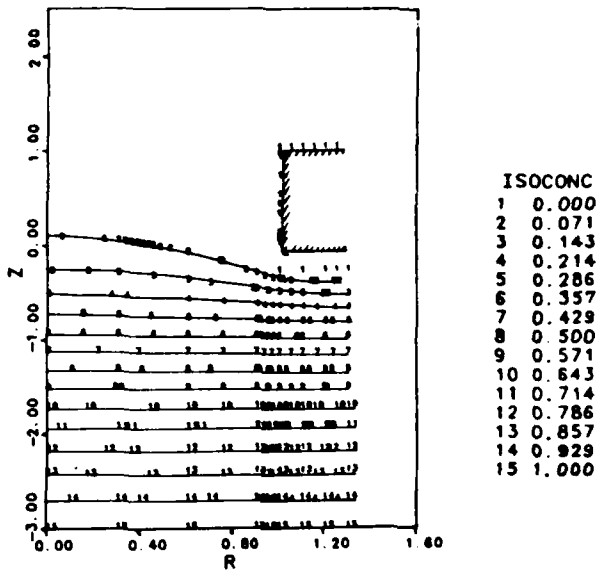

Figure C-1-6. Iso-concentration profiles when P_e=1, R_m=1.3.

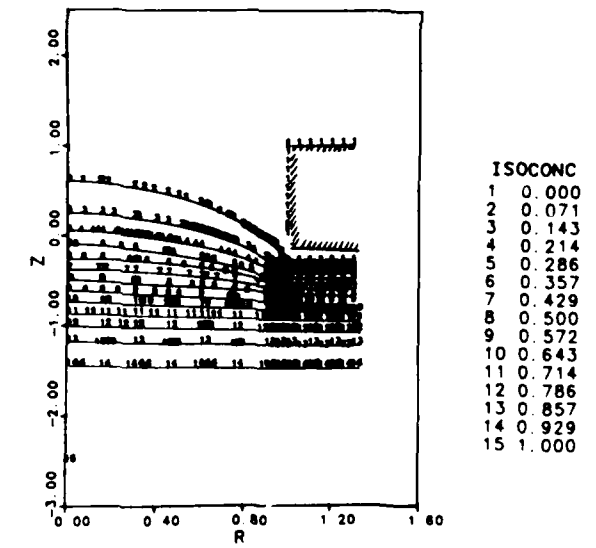

Figure C-1-7. Iso-concentration profiles when P_e=10, R_m=1.3.

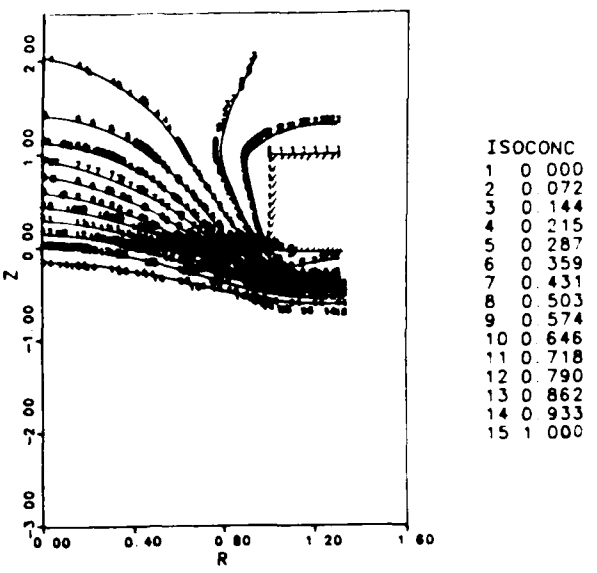

Figure C-1-8. Iso-concentration profiles when P_e=100, R_m=1.3.

Table C-1-6. The Effect of Initial Velocity on Diffusion and Inertial Efficiency when R_m=1.2, Stk=0.2

v^*	Diffusion Efficiency	Inertial Efficiency	F_μ at Pore Inlet
1	0.8949	7.257E-4	0.006096
3	0.8903	0.001174	0.025487
5	0.8857	0.002090	0.053018
10	0.8737	0.103988	0.147779

Table C-1-7. The Effect of Particle Size on Diffusion and Inertial Efficiency, R_m=1.2

v^*	Diffusion Efficiency	Inertial Efficiency	F_u at Pore Inlet
1.	0.8949	7.257E-4	0.006096
2.	0.8925	0.084998	0.007324
4.	0.8880	0.124378	0.009582
7.	0.8809	0.170056	0.012407
10.	0.8737	0.179799	0.014742
20.	0.8483	0.184490	0.020805

diffusion efficiency is greater than that of increasing inertial efficiency. And it is not clear that there should exist a minimum point of total efficiency at some particle radius, as Pich insisted.[147] This point needs more careful investigation.

e. Conclusions.

Using a finite element method, membrane filtration efficiency has been studied. First diffusional deposition in a cylinder was investigated and the results were compared to analytical results. The agreement was very good. Using the tested FEM code, computations were carried out next for membrane filters. The following conclusions wer made for membrane filtration.

(1) Using the same size particle, increasing membrane area (or decreasing porosity) increases inertial deposition efficiency and slightly increases the diffusion efficiency.

(2) Increasing flow velocity increases inertial deposition efficiency but decreases diffusion efficiency.

(3) Increasing particle size increases inertial deposition efficiency but decreases diffusion efficiency. The total efficiency did not show a minimum over computed range.

(4) Increasing Pe results in high concentration at the pore inlet but increasing convective flow decreases diffusion efficiency in the pore.

This work is being continued and compared with available experimental data. In addition, the transmission problem is being investigated for fibrous filters for both spherical and nonspherical particles.

Blank

LITERATURE CITED

1. Abraham, F. B. (1974) Homogeneous Nucleation Theory. Academic Press, New York.

2. Amelin, A. G. (1948) Kolloid Zh. 10, 68.

3. Anisimov, M. P., Kostrovskii, V. G. and Shtein, M. S. (1980) Kolloid Zh. 42, 724.

4. Birkhoff, G. and Zarantonello, E. H. (1957) Jets, Wakes and Cavities. Academic Press, New York.

5. Brock, J. R. (1983) In Theory of Dispersed Multiphase Flow (Edited by Meyer, R. E.). Academic Press, New York.

6. Clark, T. L. (1976) J. atmos. Sci. 33, 810.

7. Davis, E. J., Ravindran, P. and Ray, A. K. (1980) Chem. Engng Commun. 5, 251.

8. Delattre, P. and Friedlander, S. K. (1978) Ind. Engng Chem. Fundam. 17, 189.

9. Hidy, G. M. and Friedlander, S. K. (1964) AIChE J. 10, 115.

10. Higuchi, W. I. and O'Konski, C. T. (1960) J. Colloid Sci. 15, 14.

11. Ismagilov, F. R., Beksheneva, N. M., Masagutov, R. M. and Kiba, V. N. (1979a) Kolloid Zh. 41, 48.

12. Ismagilov, F. R., Kiva, V. N., Masagutov, R. M. and Beksheneva, N. M. (1979b) Kolloid Zh. 42, 127.

13. Pai, S. I. (1954) Fluid Dynamics of Jets. Van Nostrand, Princeton.

14. Sutugin, A. G., Grimberg, A. N. and Puchkov, A. S. (1984) J. Colloid Interface Sci. 98, 229.

15. Takahashi (1975) J. Aerosol Sci. 6, 45.

16. Binder, K. (1977) Phys. Rev. B15:4425.

17. Bixon, M. and Zwanzig, R. (1981) J. Chem. Phys. 75:2354.

18. Felderhof, B. V., and Deutch, J. M. (1976) J. Chem. Phys. 64:4551.

19. Granquist, C. G., and Buhrman, R. A. (1976) J. Appl. Phys. 47:2200.

20. Kahlweit, M. (1975) Adv. Colloid Int. Sci. 5:1.

21. Kahlweit, M. (1976). Faraday Discuss. Chem. Soc. 61:48.

22. Kirkpatrick, T. R. (1982). J. Chem. Phys. 76:4255.

23. Liesegang, R. E. (1911) Z. Phys. Chem. 75:374.

24. Lifshitz, I. M., and Slyozov, V. V. (1958) Sov. Phys. JETP. 35:331.

25. Lifshitz, I. M., and Slyozov, V. V. (1961) J. Phys. Chem. Solids. 19:35.

26. Marquesee, J. A., and Ross, J. (1983) J. Chem. Phys. 79:373.

27. Marquesee, J.A., and Ross, J. (1984) J. Chem. Phys. 80:536.

28. Muthukumar, M., and Cukier, R. I. (1981) J. Stat. Phys. 26:453.

29. Ostwald, W. (1901). Analytische Chemie. 3d ed., Engelmann, Leipzig.

30. Tsang, T. H. and Brock, J. R. (1983) Aerosol Sci. Tech. 2:311.

31. Venzl, G. (1983) Ber. Bunsenges. Phys. Chem. 87:318.

32. Wagner, C. (1961) Z. Electrochem. 65:581.

33. Ostwald, W. (1901) Analytische Chemie, 3rd ed. Engelmann, Leipzig.

34. Liesegang, R. E. (1911) Z. Phys. Chem. 75, 374.

35. Lifshitz, I. M., and Slyozov, V. V. (1958) Sov. Phys. JETP. 35, 331.

36. Lifshitz, I. M., and Slyozov, V. V. (1961) J. Phys. Chem. Solids. 19, 35.

37. Wagner, C. (1961) Electrochem. 65, 581.

38. Kahlweit, M. (1975) Adv. Colloid Int. Sci. 5, 1.

39. Kahlweit, M. (1974) Faraday Discuss. Chem. Soc. 61, 48.

40. Binder, K. (1977) Phys. Rev. B15, 4425.

41. Venzl, G. (1983) Ber. Bunsenges, Phys. Chem. 87, 318.

42. Marqusee, J. A., and Ross, J. (1983) J. Chem. Phys. 79, 373.

43. Tsang, T. H., and Brock, J. R. (1983) Aerosol Sci. Tech. 2, 311.

44. Tsang, T. H., and Brock, J. R. (In Press) Aerosol Sci Tech.

45. Desai, R.C., Koch, S. W., and Abraham, F. F. (1983) Physica 118A, 136.

46. Takajao, S., Kaysser, W. A., and Petzow, G. (1984) Acta. Metall. 32, 107.

47. Tokuyama, M., and Kawasaki, K. (1984) Physica 123A, 386.

48. Marqusee, J.A., and Ross, J. (1984) J. Chem. Phys. 80, 536.

49. Hidy, G. M., and Brock, J. R. (1970) The Dynamics of Aerocolloidal Systems, Pergamon Press, Oxford.

50. Abraham, F. (1974) Homogeneous Nucleation Theory. Academic Press, New York.

51. Defay, R. Prigogine, I., Bellemans, A. and Everett, D. (1966) Surface Tension and Adsorption. Wiley, New York.

52. Friedlander, S. (1977) Smoke, Dust and Haze. Wiley, New York.

53. Gelbard, F. and Seinfeld, J. L. (1980) J. Colloid Int. Sci. 78, 485-501.

54. Rambahadran, T. E., Peterson, T. W. and Seinfeld, J. (1976) AIChE J. 22, 840-851.

55. Rogers, R. (1979) A Short Course in Cloud Physics (2nd edn). Pergamon Press, Oxford.

56. von Neumann, J. and Richtmeyer, R. (1950) J. Apl. Phys. 21, 232.

57. Pfund, O. H. (1933) J. Opt. Soc. Am. 23, 375.

58. Beeck, O. (1945) Rev. Mod. Phys. 17, 61.

59. Kubo, R. (1975) J. Phys. Soc. Jpn. 17, 975.

60. Kimoto, K., Kamiya, Yl., Nonoyama, M. and Uyeda, R. (1963) Jpn. J. Appl. Phys. 2, 702.

61. Wada, N. (1968) Jpn. J. Apl. Phys. 7, 1287.

62. Yatsuya, S., Kasubake, S. and Uyeda, R. (1973) Jpn. J. Appl. Phys. 12, 1675.

63. Beischer, D. and Winkel, A. (1937) Die Naturwiss. 26/27, 420.

64. Tholen, A. R. (1979) Acta Metall. 27, 1765.

65. Gen, M. and Storozhov, V. (1984) Russ. J. Phys. Chem. 58, 1198.

66. Hazlett, R. D., Schechter, R. and Aggarwal, J. (1985) I.E.C. Fund. 24, 101.

67. Kawamura, K. (1973) Jpn. J. Appl. Phys. 12, 1685.

68. Ozawa, S., (1982) Ibaraki Daigaku Kogakubu Kenkuy Shuho (in Japanese). 30, 127.

69. Granqvist, C.G. and Buhrman, R. A. (1976) J. Appl. Phys. 47, 2200.

70. Hidy, G. M. and Brock, J. R. (1970) The Dynamics of Aerocolloidal Systems. Pergamon, Oxford, p. 119-132.

71. Chapman, S. and Cowling, T. G. (1951) Mathematical Theory of Non-Uniform Gases. Cambridge University Press, Cambridge, pp. 151-167.

72. Schlesinger, H. I., Brown, H. C., Finholt, A. E., Galbreath, J. R., Hochstra, H. R. and Hyde, E. K. (1953) J. Am. Chem. Soc. 75, 215.

73. Paul, R., Buisson, P. and Joseph, N. (1952) INd. Eng. Chem. 44, 1006.

74. Brown, C. A. (1970) J. Org. Chem. 35, 1900.

75. Brown, C. A. and Ahuja, Y. K. (1973) J. Org. Chem. 38, 2226.

76. Nakao, Y. and Fujishige, S. (1980) Chem. Soc. Japan 53, 1267.

77. Freitag, W. O., Sharp, T. A., Baltz, A. and Suchodolski, V. (1979) J. Appl. Phys. 50, 7801.

78. Oppegard, A. L., Darnell, F. J. and Miller, H. C. (1961) J. Appl. Phys. 32, 184.

79. Freitag, W. O. and Suchodolski, V. (1983) U.S. Patent No. 4,394,160.

80. Dragieva, I., Gavrilov, G., Buckov, D. and Slavcheva, M. (1979) J. Less-Common Metals 67, 375.

81. Sohnel, O. and Mullin, J. W. (1978) J. Cryst. Growth 44, 377.

82. Olsen, K. H. (1974) IEEE Trans. on Magnetics, MAG-110, 660.

83. Baltz, A., Freitag, W. O., Greifer, A. P. and Suchodolski, V. (1981) J. Appl. Phys. 52, 2456.

84. Detourney, J., Miranda, L., Derie, R. and Ghodsi,M. (1975) Corrosion Sci. 15, 295.

85. Bernal, J. D., Dasgupta, D. R. and Mackay, A. L. (1974) Ind. Chim. Belg. 39, 695.

86. Mandelbrodt, B. (1983) The Fractal Geom etry of Nature, W. H. Freeman, N.Y.

87. Witten, T. A. and Sander, L. M. (1981) Phys. Rev. Letters 47, 1400.

88. Meaken, P. and Waaerman, Z. R., Phys. Letters 103A, 337.

89. Shaw, D. J. (1983) Introduction to Colloid and Surface Chemistry, Butterworths, London.

90. Overbeek, J. Th. G. (1985) Powder Tech. 37, 195.

91. Valioulis, I. A. (1983) Particle Collision and Coalescence in Fluids, Ph.D. Dissertation, California Institute of Technology.

92. Ivanov, M. V., Gorbunova, K. M., Nikiforova, A. A. and Shcheredin, V. P. (1971) Dokl. Akad. Nauk. SSSR Phys. Chem. 199, 703.

93. Hidy, G. M. and Brock, J. R. (1970) The Dynamics of Aerocolloidal Systems, Pergamon, Oxford.

94. Baker, A. H., and Solimon, D. O. (1979). J Comp. Phys. 32:289-324.

95. Britter, R. E., and Griffiths, R. F. (1982). Dense Gas Dispersion. Elsevier, Amsterdam.

96. Carey, G. F., and Finlayson, B. A. (1975). Chem. Eng. Sci. 30:587-596.

97. Fromm, J. E. (1968). J. Comp. Phys. 3:176-189.

98. Fromm, J. E. (1969). Phys. Fluids Suppl. 2:3-12.

99. Fuchs, N. A., and Sutugin, A. G. (1971). In Topics in Current Aerosol Research (G. M. Hidy and J. R. Brock, Eds.). Pergamon, Oxford, Vol. 2, pp. 1-60.

100. Kerker, M. (1969). The Scattering of Light and Other Electromagnetic Radiation. Academic, New York.

101. Panofsky, H. A. (1974). Ann. Rev. Fluid Mech. 6:147-177.

102. Sehmel, G. A. (1980). Atmos. Environ. 14:983-1011.

103. Smith, F. B. (1975). Sci. Progr. Oxford 62:127-151.

104. Tsang, T. H., and Brock, J. R. (1982a). Atmos. Environ. 16:2229-2235.

105. Tsang, T. H., and Brock, J. R. (1982b). Appl. Opt. 21:1588-1592.

106. Tsang, T. H., and Brock, J. R. (1983). Unpublished.

107. Yanenko, N. N. (1971). The Method of Fractional Steps. Springer-Verlag, Berlin.

108. Anderson, J. D. (1979). In Gas Flow and Chemical Lasers, (J. F. Wendt, ed.). Hemisphere, New York, p. 3.

109. Armstrong, R. L. (1984a). Aerosol heating and vaporization by pulsed light beams, Appl. Opt. 23:148.

110. Armstrong, R. L. (1984b). Interactions of absorbing aerosols with intense light beams, J. Appl. Phys. 56:2142.

111. Bird, R. B., Steward, W. E., and Lightfoot, E. M. (1960). Transport Phenomena. John Wiley, New YOrk.

112. Book, D. L., Boris, J. P., Fry, M. A., Guirguis, R. H., and Kuhl, A. L. (1982). In Lecture Notes in Physics, Eighth International Conference on Numerical Methods in Fluid Dynamics, (E. Krause, ed.). Springer-Verlag, Berlin, v. 170, p. 143.

113. Boris, J. P., and Book, D. L. (1976). In Meth. Comput. Phys., (J. Killeen, ed.). Academic Press, New York, v. 16, p. 85.

114. Brode, H. L. (1959). Blast wave from a spherical charge, Phys. Fluids 2:217.

115. Carey, G. F. (1979). In Finite Element Methods for Convection Dominated Flows, (T. J. R. Hughes, ed.). American Society of Mechanical Engineers, New York, p. 63.

116. Chang, R. K. (1986). Nonlinear optical effects in liquid droplets: Results from high intensity lasers, presented at Workshop on the Interactions of Electromagnetic and Particle Beams with the Atmosphere, (Las Cruces, NM, Jan. 28-29).

117. Chitanvis, S. M. (1985). High energy laser interactions with water droplets, Appl. Opt. 24:3552.

118. Delbourgo, R., and Gregory, J. A. (1985). Shape preserving rational interpolation, SIAM J. Sci. Stat. Comput. 6:967.

119. Greene, W. M., Spjut, R. E., Bar-Ziv, E., Sarofim, A. F., and Longwell, J. P. (1985). Photophoresis of irradiated spheres: Absorption centers, J. Opt. Soc. Am. b 2:998.

120. Haar, L., Gallagher, J. S., and Kell, G. S. (1982). In Proceedings 8th Symposium on Thermophysical Properties, (J. V. Sengers, ed.). American Society of Mechanical Engineers, New York, v. 11, p. 298.

121. Kestin, J., Sengers, J. V., Kamgar-Parsi, B., and Levelt-Sengers, J. M. H. (1984). Thermophysical properties of fluid H_2O, J. Phys. Chem. Ref. Data 13:175.

122. McGraw, R., and Saunders, J. H. (1984). A condensation feedback mechanism of oscillatory nucleation and growth, Aerosol Sci. Technol. 3:367.

123. Pendleton, J. D. (1985). Water droplets irradiated by a pulsed CO_2 laser: Comparison of computed temperature contours with explosive vaporization patterns, Appl. Opt. 24:1631.

124. Prishivalko, A. P. (1983). Heating and destruction of water drops on exposure to radiation with inhomogeneous internal heat evolution, Sov. Phys. J. 26:142.

125. Roache, P. L. (1982). Computational Fluid Dynamics. Hermosa, Albuquerque.

126. Sageev, G., and Seinfeld, J. H. (1984). Laser heating of an aqueous aerosol particle, Appl. Opt. 23:4368.

127. Steverding, B. (1974). Ignition of laser detonation waves, J. Appl. Phys. 45:3507.

128. Woodward, P., and Colella, P. (1985). The numerical simulation of two-dimensional fluid flow with strong shocks, J. Comput. Phys. 54:115.

129. Yudanin, B. and Lax, M. (1985). In Proceedings of the 1985 CRDC Scientific Conference on Obscuration and Aerosol Research, (R. H. Kohl, ed.). Ronald H. Kohl & Associates, Tullahoma, TN, p. 339.

130. Zuev, V. E. and Zemlyanov, A. A. (1983). Explosion of a drop under the action of intense laser radiation, Sov. Phys. J. 26:149.

131. Bisyarin, V. P., Kolosov, H. A., Pozhidaev, V. N. and Sokolov, A. V., (1977). Interactions of laser radiation in the UV, visible, and IR ranges with a water aerosol, Institute of Radio Engineering and Electronics, Academy of Sciences of the USSR, 1501.

132. Carls, J. C. and Brock, J. R. (In Press). Explostion of a water droplet by pulsed laser heating, Aerosol Sci. Technol.

133. Hidy, G. M. and Brock, J. R. (1970). The Dynamics of Aerocolloidal Systems, Vol. 1, Pergamon Press, New York.

134. Williams, F. A. (1965). On vaporization of mist by radiation, Int. J. Heat Mass Transfer 8:575.

135. Armstrong, R. L. (1984). Aerosol heating and vaporization by pulsed light beams, Appl. Opt. 23:148.

136. Sageev, G. and Seinfeld, J. H. (1984). Laser heating of an aqueous aerosol particle, Appl. Opt. 23:4368.

137. Pendleton, J. D. (1985). Water droplets irradiated by a pulsed CO_2 laser: Comparison of computed temperature contours with explosive vaporization patterns, Appl. Opt. 24:1631.

138. Bohren, C. F. and Huffman, D. R. (1983). Absorption and Scattering of Light by Small Particles. Wiley, New York.

139. Bird, R. B., Stewart, W. E. and Lightfoot, E. N. (1961). Transport Phenomena. Wiley, New York.

140. Caledonia, G. E. and Teare, J. D. (1977). Laser beam-hygroscopic aerosol interactions, J. Heat Transfer 99:281.

141. Reid, R. C., Prausnitz, J. M. and Sherwood, T. K. (1977). The Properties of Gases and Liquids, 3rd Ed. McGraw-Hill, New York.

142. Tsang, T. H. and Brock, J. R. (1983). Simulation of condensation aerosol growth by condensation and evaporation, Aerosol Sci. and Technol. 2:311-320.

143. Harney, R. C. (1977). Hole-boring in clouds by high-intensity laser beams: Theory, Appl. Opt. 16:2974.

144. Sutton, G. W. (1978). Fog hole boring with pulsed high-energy lasers: An exact solution including scattering and absorption, Appl. Opt. 17:3424.

145. Glickler, S. L. (1971). Propagation of a 10.6- laser through a cloud including droplet vaporization, Appl. Opot. 10:144.

146. Brock, J. R. and Oates, J. (In Press). Moment simulation of aerosol dynamics, J. Aerosol Sci.

147. Pich, J. (1968). "Aerosol Science" Chapter Nine, ed. Davies. Academic Press.

148. Murty, V.D. (1982). Ph.D. Dissertation, University of Texas at Austin.

149. Tan, C. W. and Hsu, C. (1971). J. Aerosol Sci. 2, P117.

150. Tan, C. W. and Hsu, C. (1970). Int. J. Heat and Mass Transfer. 13, P1887.

151. Ingham, D. B. (1975). J. Aerosol Sci. 6, P125.

152. Ingham, D. B. (1984). J. Aerosol Sci. 15, P637.

153. Gormley, P. G. and Kennedy, M. (1949). Proc. R. Ir. Acad. 52, P163.

154. Davies, C. N. (1946). Proc. R. Soc. Lond., B133, P282.

155. Davies, C. N. (1973). J. Aerosol Sci., 4, P367.

156. Friedlander, S. K. (1977). Smoke, Dust and Haze, Chapter 2, John Wiley Sons.

END

10-87

DTIC